FACULTY
OF MATHEMATICS
AND PHYSICS
Charles University

DOCTORAL THESIS

Gabriel Korcsmáros

Properties of point defects in CdTe at temperatures of 300 - 600 K

Department of Optoelectronics and Magneto-optics,
Institute of Physics

Supervisor of the doctoral thesis: doc. RNDr. Pavel Moravec, CSc.

Study program: Physics

Specialization: Quantum Optics and Optoelectronics

Prague 2019

I declare that I carried out this doctoral thesis independently, and only with the cited sources, literature and other professional sources.

I understand that my work relates to the rights and obligations under the Act No. 121/2000 Coll., the Copyright Act, as amended, in particular the fact that the Charles University has the right to conclude a license agreement on the use of this work as a school work pursuant to Section 60 paragraph 1 of the Copyright Act.

In…..... date..... signature

Acknowledgement

Hereby, I would like to thank mainly to my supervisor doc. RNDr. Pavel Moravec, CSc. for his continuous guidance during my study and his help with the experiments. Besides, I am also very thankful to prof. RNDr. Roman Grill, CSc. for his help and support with his theoretical insights. Nonetheless, I would like to express also my gratitude to Miloš Černý, for his help with the crystal cutting for my experiments, RNDr. Martin Veis, Ph.D. and Kristupas Kazimieras Tikuišis, Ph.D. for their help with the ellipsometrical measurements, doc. RNDr. Karel Mašek, Dr. for his help with SIMS and XPS measurements, RNDr. Václav Dědič, Ph.D. for his help with the photoluminescence measurements and RNDr. Klára Uhlířová, Ph.D. for her help with the atomic force microscope measurements.

In addition, I am also much obliged to my parents and to my sister for their support upon my studies and during writing my thesis. Last but not least, I would like also to thank to my wife, for her support, cheer and positiveness during my study.

Title: Properties of point defects in CdTe at temperatures of 300 - 600 K

Author: Gabriel Korcsmáros

Department / Institute: Institute of Physics of Charles University

Supervisor of the doctoral thesis: doc. RNDr. Pavel Moravec, CSc., Institute of Physics of Charles University

Abstract: The thermal stability of p-type CdTe crystals by using conductivity and Hall-effect measurements have been studied at room and slightly increased temperatures. It was observed that thermal changes often implicate an anomalous behavior of the hole density characterized by reversible decrease/increase in a heating/cooling regime. This anomaly was explained by a transfer of fast diffusing donors between Te inclusions and the bulk of the sample. Sodium and potassium were determined by the Secondary Ion Mass Spectroscopy (SIMS) as the most probable diffusing species. To verify this behavior samples were also treated in saturated NaCl solution for different time intervals in order to examine the influence of the oxide layer and sodium on the surface of the sample. To determine the structure of the surface the sample was characterized by ellipsometric and X-ray photoelectron spectroscopy (XPS) and SIMS. Very low determined diffusion coefficient of Na was explained by trapping of Na in Cd sublattice.

Keywords: CdTe, diffusion, ellipsometry, SIMS, XPS

Contents

Introduction

The invention of semiconducting materials started an industrial revolution. Although, this revolution was slow in the beginning, it continuously grew up to nowadays. The first semiconductors helped in computation and after the introduction of microchips the computer industry started to grow rapidly. The same analogy applies for the semiconducting detectors, which are in fact "solid ionization chambers". The fact that semiconductors are solid materials means that they are able to detect much higher energies than gas filled detectors due to much higher density. Besides a semiconductor detector produces a signal which is proportional to the amount of radiation energy absorbed, allowing energy-proportional radiation counting. These capabilities allowed to revolutionize several fields, including space technology, medical imaging, energy industry and military. Nowadays, none of the mentioned fields could be imagined without semiconducting detectors.

However, semiconducting materials also have some limitations which, depending on the field of application, can narrow their usage. The first is the operating temperature, where the amount of thermally induced electrical current at room temperature influences the radiation-induced current. Due to this limitation, this kind of detectors must be constantly cooled in order to work optimally. For example, Si detectors (usually) and Ge detectors (always) must be used at temperatures well below room temperature. The second biggest limitation is the purity of the semiconductor material. During the growth of the crystal several impurities can influence the crystal structure of the material, creating signal traps for the detection. Besides, native crystal defects such as dislocations and point defects also negatively influence the quality of the crystal. Depending on the energy of the radiation the semiconducting detector needs to absorb the radiation in order to detect it sufficiently. This is connected with the size of detector and again with the quality of the crystal structure.

One promising semiconductor material for gamma or X-ray detection is Cadmium telluride. The main advantage of this semiconductor is that it can be operated at room temperature without excessive electronic noise, and due to its high atomic number absorbs better gamma radiation, which results in smaller crystal sizes.

1. CdTe

Cadmium telluride is known to the mankind more than a century. First it was prepared by a French chemist called Margottet, who reacted Te with metals in 1879 [1] . CdTe belongs into group II-VI of semiconductors and crystallizes in a cubic zinc-blende structure with a lattice constant of a = 6.48 Å, depicted on Fig. 1.1:

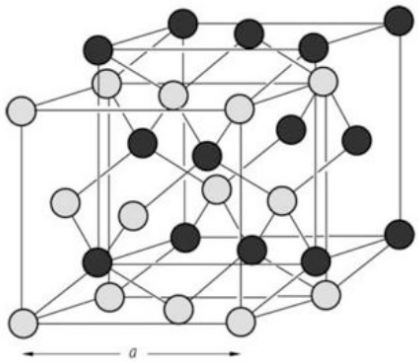

Fig. 1.1: Zinc-blende crystal **[2]**.

It has a relatively high band gap ~ 1.5 eV at 300 K. Thus near room temperature it is not necessary to cool down a CdTe detector due to the low thermal noise. Besides, as mentioned before, it has also high atomic number, Z_{Cd}= 48, Z_{Te}=52 (compared to Z_{Ge}=32 or Z_{Si}=14) resulting higher energy absorption, as the absorption ratio is proportional to the 4-5 power of the atomic number ($a \sim Z^{4-5}$). CdTe has a direct energy band structure with a minimum of the conduction band and maximum of the valence band in the center of Brillouin zone, Γ point [3], showed on Fig. 1.2 below.

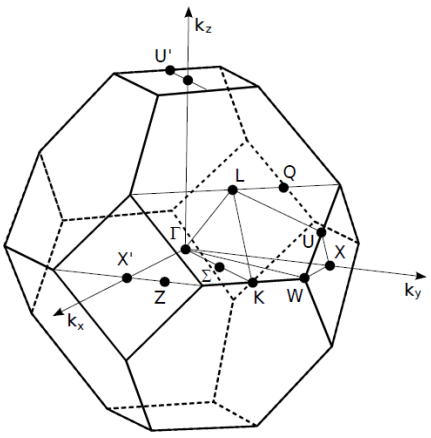

Fig. 1.2: Brillouin zone of zinc blende structure **[4]**.

Undoped CdTe is used as gamma or X-ray detector in the field of medical imaging [5] and also in the field of photovoltaics [6]. Besides, CdTe is also applied as electro-optic modulator, since it has the greatest electro-optic coefficient among the II-VI semiconductors [7]. Moreover, $Cd_{1-x}Zn_xTe$ is used as a substrate material for $Hg_{1-x}Cd_xTe$ infrared detectors. Both materials are tunable in its composition, whereas $Cd_{1-x}Zn_xTe$ can be varied in the lattice constant to fit to the lattice constant of the tuned to a $Hg_{1-x}Cd_xTe$ defined wavelength between 1 – 30 µm.

1.1 Band structure and electrical properties of CdTe

The valence band structure of CdTe consists from three bands, whereas two of them are degenerated at $\vec{k} = 0$ and the third band is split-off by spin-orbital coupling. The first with lower curvature is the heavy-hole band and the second with larger curvature is the light-hole band. The third is the spin-orbit split-off band, shifted by the spin-orbit splitting energy Δ_0. With the Kane model [8] the interaction of the valance band with the conduction band via $\vec{k} \cdot \vec{p}$ interaction and $\vec{k}$ – independent spin-orbit interaction is considered. This model takes in consideration the atomic wave function and the spin of the electron. The band structure can be described by three parameters: bandgap width E_G, momentum matrix element P and the spin-orbit splitting energy Δ_0. The parameter P can be expressed also as an energy $E_P = 2m_0P^2/\hbar^2$, which is $8.94 \times 10^{-8} eVcm$. The value of Δ_0 can be estimated from electroreflectance [9] measurements as $0.91eV$. In the vicinity of $\vec{k} = 0$ we have the following parabolic bands:

$$E_n(k) = E_0 + \frac{E_0 E_p}{3}\left(\frac{2}{E_G} + \frac{1}{\Delta_0 + E_G}\right) = \frac{\hbar k^2}{2m_n} \tag{1.1}$$

$$E_{lh}(k) = E_0 - E_G + \frac{2E_0 E_p}{3} = -E_G - \frac{\hbar k^2}{2m_{lh}} \tag{1.2}$$

$$E_{hh}(k) = -E_G - \frac{\hbar k^2}{2m_{hh}} \tag{1.3}$$

$$E_{so}(k) = E_0 - E_G - \Delta_0 - \frac{2E_0E_p}{3(E_G + \Delta_0)} = -E_G - \Delta_0 - \frac{\hbar k^2}{2m_{so}} \quad (1.4)$$

The electrical properties are highly influenced by the impurities, native defects and the interactions between them. The intrinsic carrier concentration of the semiconductor is determined by the band gap E_G and the density of states effective masses m_n^*/m_0 and m_p^*/m_0 for electrons and holes, respectively. The band gap we can define, based on Chadi [10] as:

$$E_G(eV) = 1.622 - 3.5 \times 10^{-4}\, T \quad (1.5)$$

$m_n^*/m_0 = 0.1$, and $m_p^*/m_0 = 0.8$. The electron effective mass approximates the value obtained by Mears and Stradling [11] and the hole effective mass is the heavy-hole mass value that Kranzer [12] found to give the best agreement between experimental data and theoretical mobility. The mobility of holes in CdTe was investigated by Yamada [13], who fitted his experimental data for as-grown, nominally undoped p-type samples with room temperature concentration of about 5×10^{14} cm^{-3}, the mobility is about 80 $cm^2V^{-1}s^{-1}$ at 300K. Besides, for n-type samples the electron mobility, reported by Triboulet and Marfaing [14], is approximately 950 $cm^2V^{-1}s^{-1}$ for the purest samples.

1.2 Crystal growth

This chapter will introduce the basic thermodynamic theory of solidification process and some known techniques of the crystal growth based on [15].

As a first step in a crystal growth process, the starting material is inserted into an ampoule and heated up slightly above the melting temperature, where it is held for homogenization of the melt. Thereafter, the melt is slowly cooled down to room temperature. This transformation process of the melt to solid can be described as a process in a thermodynamic system where the thermodynamic potentials change. The

process where the volume change is minor and the pressure remains constant, can be described in terms of Helmholtz free energy F as follows:

$$dF = dU - TdS - SdT\,. \tag{1.6}$$

Where U is the internal energy, S is the entropy and T is the temperature. The stability of a thermodynamic system is also described by a minimum of the Gibbs free energy G:

$$dG = dH - TdS - SdT = dU - TdS - SdT + Vdp + pdV \tag{1.7}$$

where H is the enthalpy, V is the volume and p is the pressure of the system. For isobaric and isothermal processes, the Gibbs energy is calculated (1.7) and for systems under constant temperature and volume the Helmholtz free energy is calculated. Thus, to describe the stability of a thermo-dynamic system the minimum of the Gibbs free energy can be used.

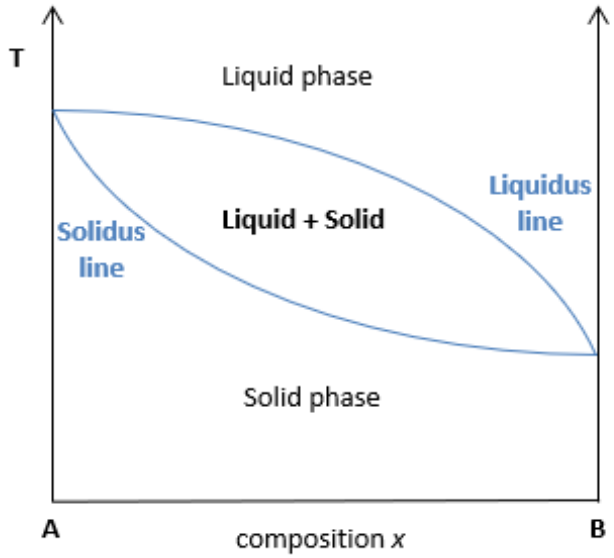

Fig. 1.3: Isobaric phase T-x diagram of the binary compound.

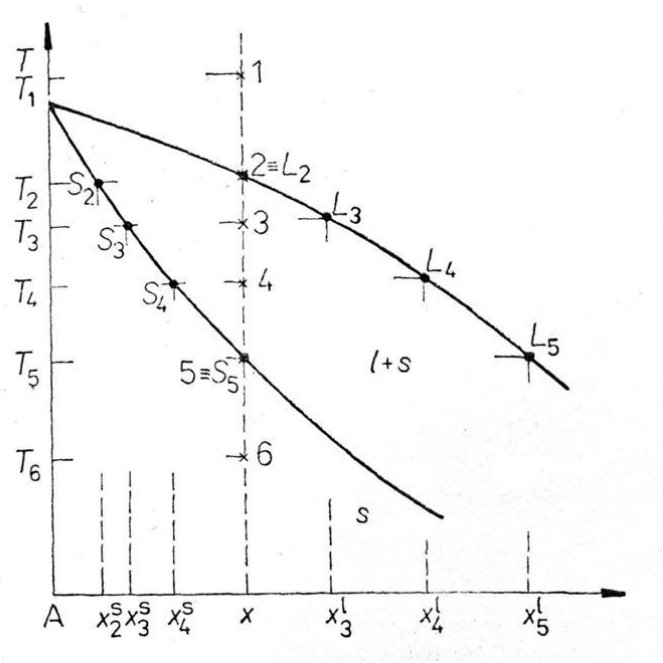

Fig. 1.4: The composition and temperature dependences of the solid and liquid phase composition during equilibration solidification **[16]**.

Minimum of free energy in dependence of temperature and composition is depicted on Fig. 1.3 as an *isobaric phase T-x* diagram. Fig. 1.4 shows a simplified T-x phase diagram if a binary compound formed from components A and B (detailed Fig. 1.3). Ideally, during this transformation the temperature change is infinitely slow. For temperatures below the solidus line the binary system consists of solid, for temperature above the liquidus line the binary system consists of liquid solution and between the solidus line and the liquidus line the binary system consists of mixture of liquid solution and solid.

Fig 1.4 depicts an ideal transformation of a binary system from liquid state to solid state by a slow temperature decrease. T_i and states 1 - 6 represent different temperatures and its corresponding states in the phase diagram. The equilibrium state at temperature T_1 is at point 1 in the phase diagram. The whole system consists of liquid solution at this point. Upon the temperature reaches temperature T_2 the state of the system will lay on the liquidus curve and the first solid phase particles appear. The composition of solid phase particles x_2^S is given by the point S_2 on the solidus line, the composition of the liquid solution is defined by L_2. The following two states, at temperatures T3 and T4, at points 3 and 4, after gradually decreasing the temperature represent phase states inside the liquidus and solidus lines. The composition of both solid (S_i) and liquid (L_i) phases are gradually changing. The

ratio of the solid phase and the liquid phase in the saturated solution is given by the lever rule:

$$n_l(x - x_l) = n_s(x_s - x) \tag{1.8}$$

where the system composition is x, x_l and x_s are molar atomic fractions of liquid and solid, n_l and n_s are material amounts in the liquid and solid phase. For the solidification process it is also necessary to suppose that after state S_2 the temperature decrease is slow enough to equilibration of the composition differences in solidified particles by diffusion. Besides, at temperature T_5 the liquid droplets solidify in the whole system. In the final state, at temperature T_6, there is only one solid phase present in the whole material with composition x and the same composition is present in the whole crystal ingot.

1.3 CdTe crystal growth methods

The mostly used growing methods for CdTe crystals are derived from Bridgman method (BM) [17] and from travelling heater method (THM) technique.

1) Bridgman method

This growth method is one of the oldest technique (1924) for crystal growth and applies a crystal growth from melt, see also Fig. 1.5. In Bridgman method the crucible contains the molten material and it is moved along the axis of the temperature gradient in the furnace. The principle of this method is that the solidification occurs by a translational movement of the melt from a hot zone to a cold zone. As a first step the polycrystalline material in the crucible has to be melted completely in the hot zone and be brought into contact with a seed at the bottom of the crucible. The seed is a single crystal with a defined crystallographic orientation defining the single-crystal growth. The crucible is moved slowly into the cooler section of the furnace. The temperature at the bottom of the crucible is below the solidification temperature and the crystal growth is initiated by the seed at the melt-seed interface. After the whole crucible is moved through the cold zone the whole

melt converts to a solid single-crystalline ingot. Besides, the Bridgman method can be implemented in vertical or in horizontal configuration.

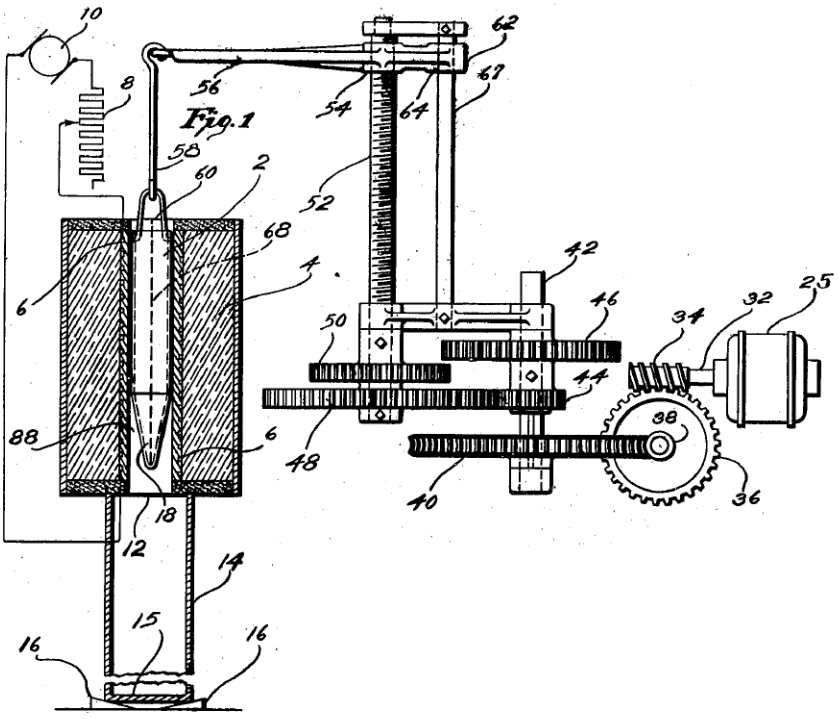

Fig. 1.5: The original diagrammatic view of Bridgman's crystal growth apparatus from his granted patent US1793672A.

2) Vertical gradient freeze method

This growth method is analogous to the Bridgman method. However, this method does not implement any movement of the crucible in the axis of the temperature gradient. In this case the temperature is regulated by the furnace coil along the ampoule, see Fig. 1.6. Thus, the hot zone and cold zone in the crucible is controlled by the applied current in the coils.

Vertical Bridgman method **Vertical Gradient Freeze method**

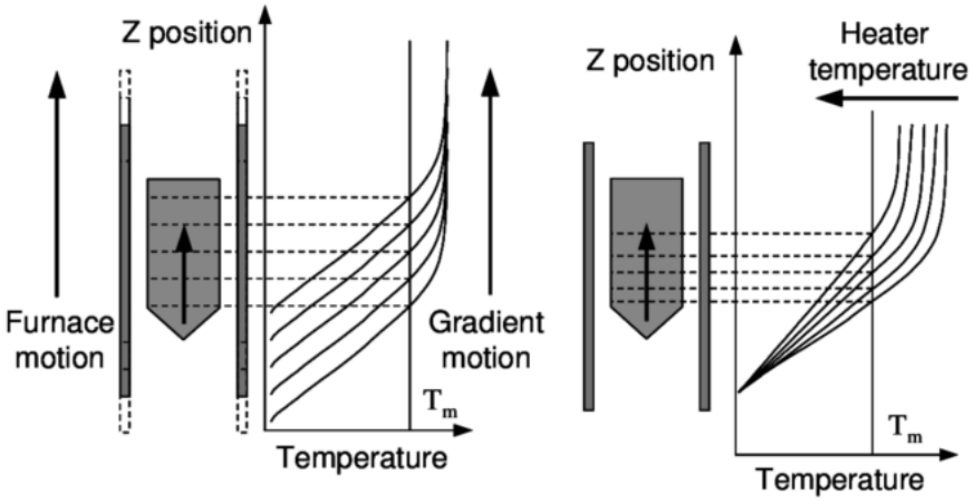

Fig. 1.6: A schematic view of vertical Bridgman method and vertical gradient freeze method from **[18]**. For the Bridgman method either the furnace or the crucible is moved in the temperature gradient. In the case of vertical gradient freeze method, the temperature gradient is controlled and shifted along the ampoule.

3) Travelling heater method

This method is analogous to the zone refining technique, which was developed to purification of metal elements from impurities. The travelling heater method (THM) is used for crystal purification and also for crystal growth. It is applied on a polycrystalline material placed into an evacuated chamber. A movable heating coil is used to produce a melting zone locally and moved from the top to the end of the polycrystal. The floating zone pushes the impurities from the melting zone and generally a monocrystalline material is solidified behind the floating zone. The speed of the floating zone is very slow ~ 5mm/day.

The number of degrees of freedom Φ is given by the Gibbs phase rule, $\Phi = c - \varphi + 2$, where c is the number of components and φ is the number of phases. Since CdTe is a binary compound and during crystallization two phases are present, the number of degrees of freedom is 2. The number of degrees of freedom is the number of independent intensive variables that is the largest number of thermodynamic parameters such as temperature or pressure that can be varied simultaneously and arbitrarily without determining one another. Thus, in order to define an equilibrium

state for CdTe the composition *x*, the temperature *T* and the partial pressure *P* must be considered.

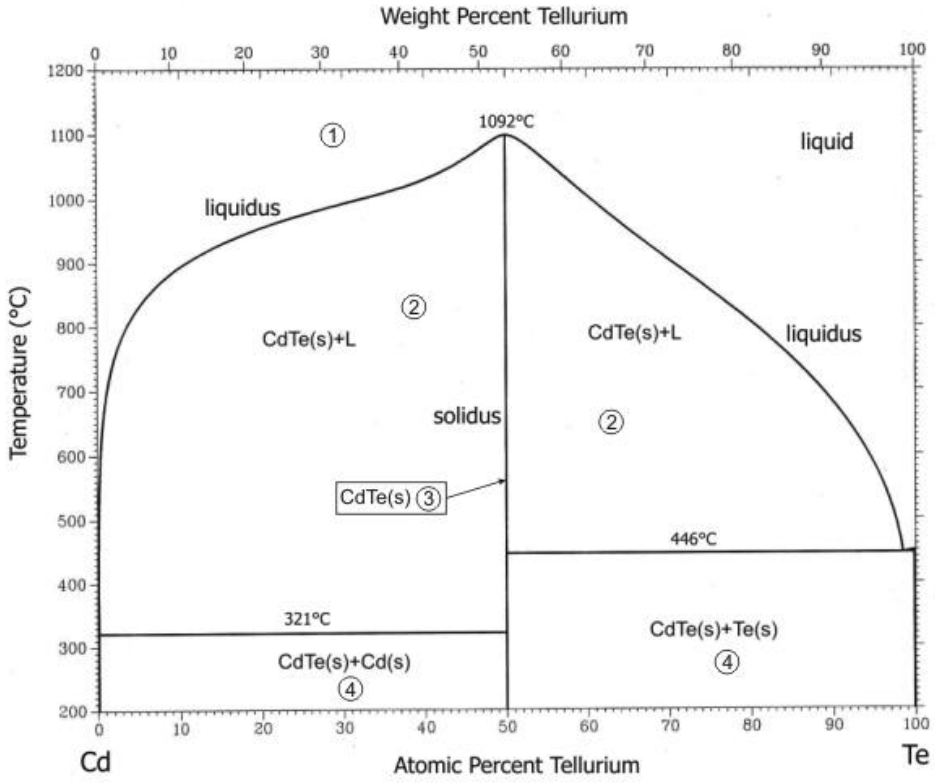

Fig. 1.7: Equilibrium *T-x* diagram of CdTe **[19]**.

In Fig. 1.7 the equilibrium T-x diagram is showed. In region 1 the binary system is liquid in any composition, region 2 relates to a mixture region of melt and solid, the middle region 3 is a solid state in equilibrium and region 4 refers to two solid phases with different compositions. The center solidus line, corresponding to region 3, stands for the stability region of the CdTe compound. The P-T diagram is shown in Fig. 1.8:

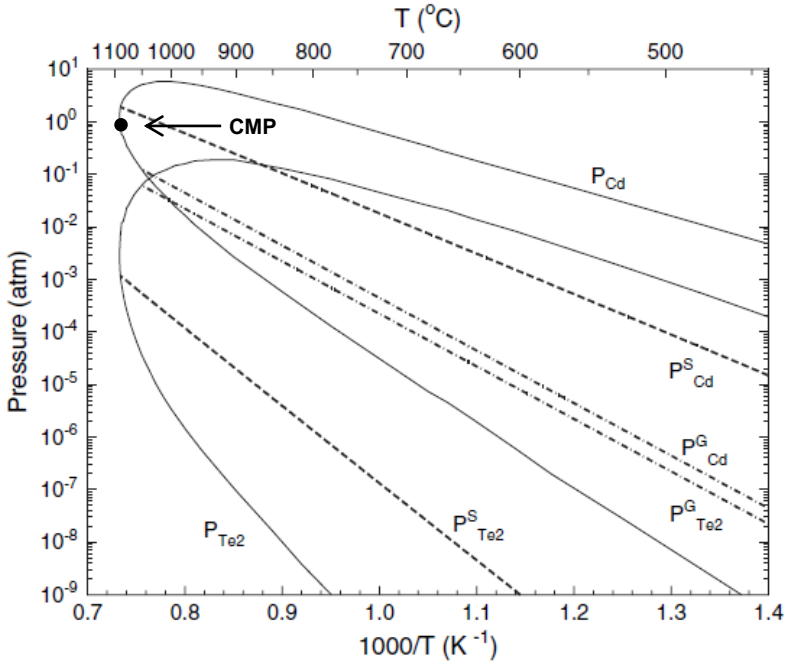

Fig. 1.8: *P-T* diagram of CdTe. The solid $\boldsymbol{P_{Te_2}}$ and $\boldsymbol{P_{Cd}}$ lines denote the partial pressure along the three-phase loop of solid CdTe. The dashed lines $\boldsymbol{P^S_{Te_2}}$ and $\boldsymbol{P^S_{Cd}}$ show the pressure over stoichiometric solid CdTe. The dash-dotted lines $\boldsymbol{P^G_{Cd}}$ and $\boldsymbol{P^G_{Te_2}}$ plot respective pressure over subliming CdTe **[20]**. CMP denotes the congruent melting point.

From Fig. 1.9 it can be deduced that the tellurium atom fraction is not symmetrical along the three-phase curve. The native point defects in the material cause derivations. At the Cd rich side, the experiment shows maximum deviation from stoichiometry near 850°C. The donor-type Te antisite Te_{Cd} can significantly influence the stability region in Te-rich conditions.

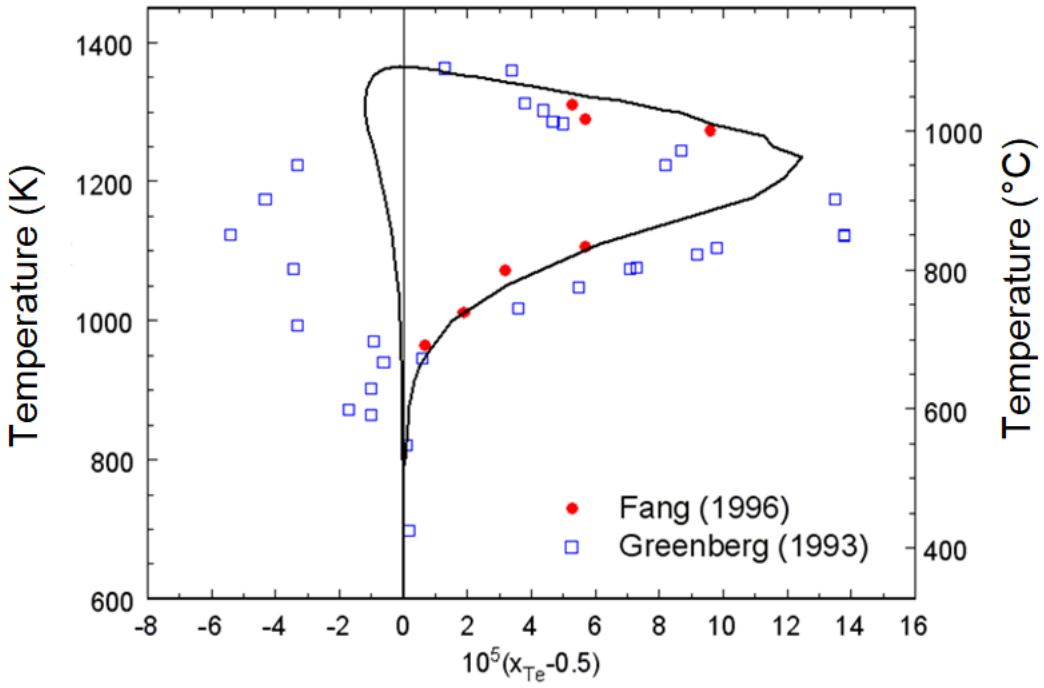

Fig. 1.9: The fit of the tellurium atom fraction in CdTe along the three-phase curve **[21]** together with the experimental data **[22]** (red circle) and **[23]** (open square).

During the crystallization process the temperature of the melt, crystallization interface and pressure of the system needs to be controlled. The pressure of the whole system is determined by the coldest place of the system, which can be determined from the equilibrium thermodynamic process and Pascal's law. By controlling the partial pressure formed above cadmium/tellurium source in the coldest place of the evacuated system we are able to control the pressure. This pressure can be determined by the Dalton's law in the system, which reads as follows:

$$P_{tot} = P_{Cd} + P_{Te_2} . \tag{1.9}$$

The partial pressure P_{Te_2} pressure (atm)-temperature diagram can be written as in [22]:

$$P_{Te_2} = exp(45.23 - 69080/T)P_{Cd}^2 . \tag{1.10}$$

This form also defines the congruent sublimation line via $P_{Cd} = 2P_{Te_2}$. The CdTe Gibbs formation energy reads [24]:

$$G_f(CdTe) = -2.975 + 1.36 \times 10^{-3} T \ (eV). \tag{1.11}$$

The crystallization process requires high-purity materials and for Bridgman method the solidification requires a stoichiometric composition. Upon solidification the state of the system goes to the congruent melting point 1092°C (in the T-x diagram at maximum of the liquidus line in Fig. 1.7 and in the P-T diagram point CMP in Fig. 1.8), where both the solid and liquid state have the same composition. In ideal case the system should follow the solidus line in the T-x diagram and the stoichiometric line P_{Cd} in the P-T diagram, by controlling the temperature and the pressure. The CMP point is closer to a tellurium enriched state and it is not on the stoichiometric line P_{Cd}, as it can be seen in Fig. 1.8. Therefore, upon the crystallization process it is necessary to shift the state towards the stoichiometric line. By keeping that condition up to room temperature, a crystal with stoichiometric composition can be solidified. Nevertheless, under realistic conditions the crystal growth process can be influenced by several factors and the final product can comprise several types of defects.

1.4 Native point defects in CdTe

Native point defects can greatly influence the electrical properties of the semiconductors. Besides, it is complicated to determine the properties, density and mutual interactions of the defects. In a binary compound *AB,* cation and anion vacancies V_A, V_B, interstitials A_i, B_i and antisite defects B_A, A_B can occur, see also Fig. 1.10. Moreover, complex defects like vacancy-antisite complex B_AV_A or double vacancies can also occur. At room temperature the electrical properties of the semiconductor are influenced by the native defects reactions, which proceed upon cooling or at any temperature change.

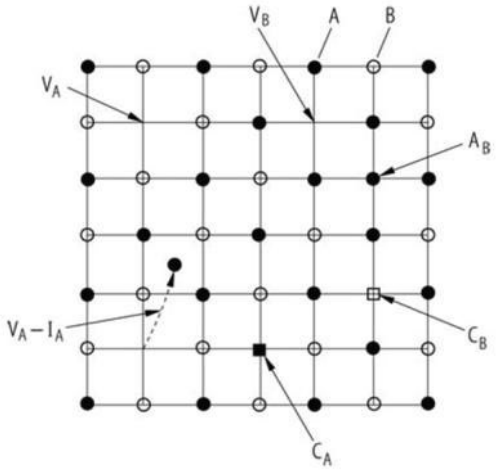

Fig. 1.10: Various crystal defects in a crystal lattice. A, B are crystal atoms, V – vacancy, I –interstitial, C –impurity **[25]**.

For the calculation of defect densities, it is convenient to start with neutral point defects whose density is independent on the Fermi energy E_F [26].. Thus, the evaluation of the defects is based on the Gibbs energy $G = H - TS$. The neutral defect densities are set by P_{Cd} by the following reactions and respective formulas

$$Cd_I^0 \leftrightarrow Cd_g\,, \tag{1.12}$$

$$[Cd_I^0] = n_0 \frac{P_{Cd}}{\kappa} exp\left[\frac{S(Cd_I)^{vib}}{k_b}\right] \times exp\left[-\frac{E(Cd_I)+U(Cd_I)^{vib}}{k_b T}\right], \tag{1.13}$$

$$V_{Cd}^0 \leftrightarrow Cd_{Cd} - Cd_g\,, \tag{1.14}$$

$$[V_{Cd}^0] = n_0 \frac{\kappa}{P_{Cd}} exp\left[\frac{S(V_{Cd})^{vib}}{k_b}\right] \times exp\left[-\frac{E(V_{Cd}) + U(V_{Cd})^{vib}}{k_b T}\right], \tag{1.15}$$

$$Te_{Cd}^0 \leftrightarrow 2Cd_{Cd} + Te_{Te} - 2Cd_g\,, \tag{1.16}$$

$$[Te_{Cd}^0] = n_0 \frac{\kappa^2}{P_{Cd}^2} exp\left[\frac{S(Te_{Cd})^{vib}}{k_b}\right] \times exp\left[-\frac{E(Te_{Cd}) + U(Te_{Cd})^{vib}}{k_b T}\right], \tag{1.17}$$

The formation energy E is related to the corresponding defect reaction, energy U^{vib} and entropy S^{vib} determine contributions to the vibrational free energy. κ is defined as

$$\kappa = (k_b T)^{5/2} \left(\frac{m_{Cd}}{2\pi\hbar^2}\right)^{3/2} \tag{1.18}$$

and connects Cd chemical potential μ_{Cd} to P_{Cd} as

$$\mu_{Cd} = k_b T ln \frac{P_{Cd}}{\kappa}, \tag{1.19}$$

n_0 = 1.48×10^{22} cm^{-3} is the Cd or Te atom density, k_b is the Boltzmann constant and m_{Cd} is the mass of the Cd atom. For the multiply ionized defects the densities for acceptors and donors are calculated as follows:

$$[X^{z-}] = [X^0] \frac{g_{X^{z-}}}{g_{X^z}} exp\left(\frac{zE_F - E_a^1 - \ldots - E_a^Z}{k_b T}\right), \tag{1.20}$$

$$[X^{z+}] = [X^0] \frac{g_{X^{z+}}}{g_{X^0}} exp\left(\frac{E_d^1 + \ldots + E_d^Z - zE_F}{k_b T}\right), \tag{1.21}$$

where E_a and E_d refer to the acceptor and donor one-electron ionization energies, $g_{X^{z-}}$ and $g_{X^{z+}}$ are the defect degeneracies, z refers to the ionization degree.

If we will consider a vacancy of atom A in a II-VI compound AB, we can study two acceptor ionization energy levels in the bandgap. We can label these energies as the first and second ionization levels, E_{A_1} and E_{A_2}, respectively ($E_{A_1} < E_{A_2}$). An equilibrium state with an external phase containing A in the vapor (A_g) is written as:

$$AB \Leftrightarrow V_A B + A_g \,. \tag{1.22}$$

From the Mass action law, we can get:

$$[V_A^0] = K_{V_A^0}/P_A \,, \tag{1.23}$$

where the concentration of the neutral vacancies is proportional to the ratio of the reaction constant $K_{V_A^0}$ and the pressure P_A of A in the vapor phase. The reaction constant can be defined based on the formation energy parameters, enthalpy $H_{V_A^0}$ and entropy $S_{V_A^0}$:

$$K_{V_A^0} = (k_b T)^{5/2}(2\pi m_A)^{3/2}\hbar^{-3} exp\left(\frac{H_{V_A^0}}{k_b T}\right) exp\left(\frac{S_{V_A^0}}{T}\right), \tag{1.24}$$

where m_A is the mass of A, $\hbar$ is the Planck's constant and k_b in the Boltzmann's constant. The last expression holds when concentrations are expressed in site fractions and pressure in atmospheres. The formation enthalpy H is often interpreted also as the formation energy itself. From the above relations we can formulate the ionization relations of singly $[V_A^-]$ and doubly ionized vacancies $[V_A^{2-}]$:

$$[V_A^-] = \left(g_{V_A^-}/g_{V_A^0}\right) exp\left(\frac{E_F - E_{A_1}}{kT}\right)[V_A^0], \tag{1.25}$$

$$[V_A^{2-}] = \left(g_{V_A^{2-}}/g_{V_A^-}\right) exp\left(\frac{E_F - E_{A_2}}{kT}\right)[V_A^-], \tag{1.26}$$

where the g are the degeneracy factors corresponding to the ionization states. The Fermi level energy is E_F and its position depends on the electrical equilibrium in the solid, formulated by the electrical neutrality condition

$$n + [V_A^-] + 2[V_A^{2-}] + N_A^- = p + N_D^+, \tag{1.27}$$

where n and p refer to the free electron and hole concentrations, N_A^- and N_D^+ are concentrations of any foreign ionized donor and acceptor impurities, respectively.

One of the first who extensively studied the characteristics of point defects was de Nobel [27]. In his model he was considering Cd interstitials as Cd_I as dominant native donor and Cd vacancies V_{Cd} as dominant native acceptors. The model parameters K_1, K_2, K_3, K_4, K_r and K_F, in the set of equations describing the defect equilibrium, are in Arrhenius-like form.

$$
\begin{aligned}
np &= K_i, \\
[Cd_I^0] &= K_r P_{Cd}/K_1, \\
[Cd_I^+] &= K_r P_{Cd}/n\,, \\
[Cd_I^{2+}] &= K_2 K_r P_{Cd}/n^2\,, \\
[V_{Cd}^0] &= K_3 K_F/K_r P_{Cd}\,, \\
[V_{Cd}^-] &= nK_F/K_r P_{Cd}\,, \\
[V_{Cd}^{2-}] &= n^2 K_F/K_4 K_r P_{Cd}\,, \\
n + [V_{Cd}^-] + 2[V_{Cd}^{2-}] &= p + [Cd_I^+] + 2[Cd_I^{2+}]\,,
\end{aligned}
\tag{1.28}
$$

K_1, K_2, K_3, and K_4 can be connected to the defect ionization energies through Eqs. (1.20) and (1.21). K_r and K_F are linked to the energy of the formation of the ionized defects E' through equations (1.25) and (1.26).

While the ionization energies of the defects E_a and E_d can be obtained from different electrical and optical measurements, the energies of the defect formation connected to parameters K_r and K_F are much harder to be measured. Nonetheless, de Nobel found out from Hall-effect measurements on quenched samples, treated at different temperatures at high P_{Cd}, that the free electron concentration n is proportional to $P_{Cd}^{1/2}$. He concluded that for high P_{Cd} the free electron concentration should be prevailed by ionized Cd interstitials. For this case, the neutrality equation in system (1.28) can be simplified as follows

$$
n = [Cd_I^+]. \tag{1.29}
$$

This equation can be substituted in the third equation of (1.28) and we can get

$$
n = (K_r P_{Cd})^{1/2}. \tag{1.30}
$$

Improved defect model [28] considering divalent character of Cd interstitials led to the lower power of n proportional to $P_{Cd}^{1/3}$, which was consecutively confirmed experimentally. That is, by measurement of the free carrier concentration of samples treated in high P_{Cd} at different temperatures the parameter $K_r(T)$ can be determined

and thus the formation energy $E(Cd_I)$ through equation (1.21). The defect parameter K_F can be also determined analogously from samples annealed in low P_{Cd} by considering that in this case it is known that the hole concentration p is proportional to $P_{Cd}^{-1/2}$.

Calculated formation energies of particular neutral native point defects in CdTe are listed in Tab. 1.1 [29]. There are two interstitial sites in zinc blende structure. The first site is surrounded by anions (a) and the second one is surrounded by cations (c). For neutral Cd_I the lowest possible formation energy is $\Delta H(Cd_i^0) = 2.04eV$. Cadmium antisite defects Cd_{Te} were not observed by any experiment and are only predicted by numerical calculations [29].

defect	*Formation energy ΔH in CdTe (eV)*	*defect*	*Formation energy ΔH in CdTe (eV)*
V_{Cd}	1.88	V_{Te}	2.45
Te_i	2.62	Te_{Cd}	2.91
Cd_i^a	1.47	Cd_{Te}	3.13
Cd_i^c	1.25		

Tab. 1.1: Formation energies of native point defects in CdTe at neutral charged state [29].

The energy levels of the most frequent native point defects are depicted in Fig. 1.11. The values in Fig. 1.11 correspond to electrically active ionized native defects, which have been identified with different experimental methods [2]. Dominant donor-like native defects in Cd-rich crystals are singly ionized Cd_i^+, doubly ionized $Cd_i^{2+}$and doubly ionized Te_{Cd}^{2+}. The main acceptor-like native defects are monovalent and divalent V_{Cd}^-, and V_{Cd}^{2-}, respectively. The energy level of V_{Cd}^- is allocated relatively precisely, compared to V_{Cd}^{2-}, which can vary from 0.2 to 0.45 eV depending on the used measurement technique [2].

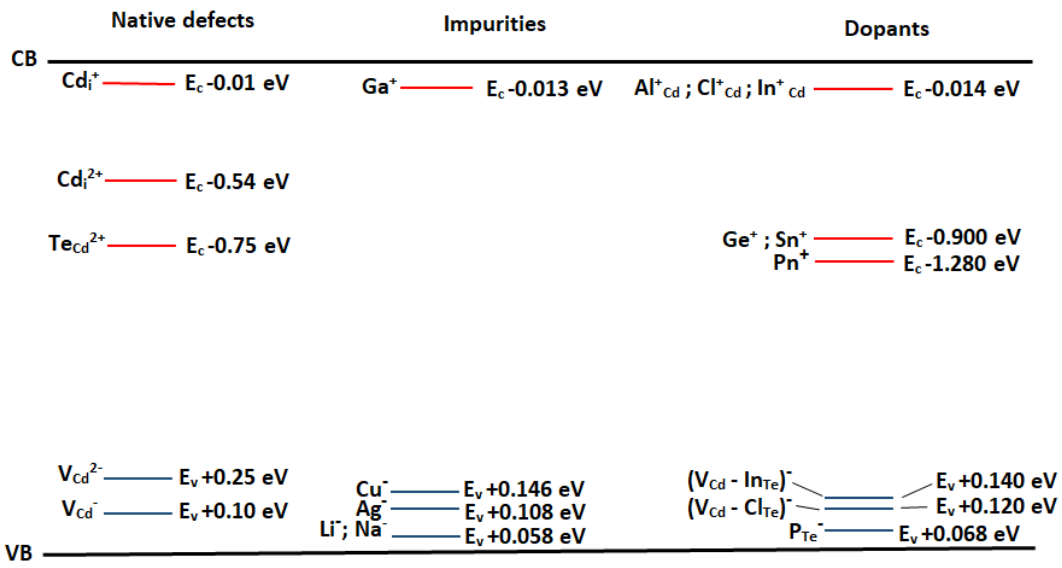

Fig. 1.11: The schematic view of energy levels of the most common defects (native, impurities and dopants) in CdTe. Red lines indicate donor levels, blue lines indicate acceptor levels.

1.5 Extrinsic point defects

Extrinsic defects can be divided into two groups. The first group comprises impurities uncontrollable present in the crystal and the second group comprises the intentionally introduced dopants specially to modify the physical and chemical properties of the material (see Fig. 1.11). The goal is to prepare materials with impurity concentration as low as possible, ideally with lower concentration than the concentration of the native point defects, which is about 10^{15}cm^{-3} at room temperature. This state can be successfully reached by the combination of purification methods such as repeated vacuum distillation and zone refining. With the mentioned methods the content of impurities can be achieved with concentrations about 10^{15}-10^{16}cm^{-3}. The most frequent impurities are Cu, Li, Na, Ag, K and O. The formation energies of the neutral and ionized impurity related point defects are listed in [30] and their energy levels are plotted in Fig. 1.11. The most important dopants for CdTe are indium and chlorine. Both dopant behave as donors and together with a cadmium vacancy create also an acceptor-like complex defect called *A-center*.

Indium atoms are embedded in the cadmium sublattice an form a shallow donor with E_i^{In} = 14.15meV. Interaction of a divalent cadmium vacancy V_{Cd}^{2-} with In_{Cd}^{+} on the closest available site form an additional monovalent acceptor-like A-center $(V_{Cd} - In_{Cd})^{-}$. The binding energy of the indium A-center is 140meV. The chlorine doping atoms are incorporated in the tellurium sublattice and form a donor-like defects with ionization energy E_i^{Cl} = 14.48meV. The chlorine A-center consisting of V_{Cd}^{2-} with Cl_{Te}^{+} exhibits the binding energy of about 120meV (see Fig. 1.11).

1.6 Diffusion processes

The diffusion process is present during the crystal growth and also during post-growth annealing. In CdTe the point defects and the impurities are also driven by this process and influence the final detector qualities of the crystal. In this chapter we will focus on the diffusion process in general and with some exact solutions with defined initial and boundary conditions based on Philibert [31].

If we restrict ourselves to a one-dimensional system where there is a concentration gradient $\frac{\partial c}{\partial x}$ of atoms, ions, point defects etc. a flux of particles is established in a *down* direction of the concentration gradient, we can express the flux proportional to the concentration gradient as Fick's equation

$$J = -D\frac{\partial c}{\partial x} \tag{1.31}$$

where D is the diffusion coefficient. The flow of particles in a given direction can be due to two causes: one is the concentration gradient and the second one is some external force. Under this force the particles move with some average velocity $\langle v \rangle c$

$$J = -D\frac{\partial c}{\partial x} + \langle v \rangle c. \tag{1.32}$$

In this case the first term on the right side is called the *Fickian or diffusional flux* and the second term is the *drift.*

In a case where the concentration is time dependent, one must combine Fick's equation with an equation of material balance. For species which obey the conservation law, this is the *equation of continuity*

$$\frac{\partial J}{\partial x} = -\frac{\partial c}{\partial t} \,. \tag{1.33}$$

The previous equation can be derived by considering a cylindrical parallel to the diffusion direction, of unit cross sectional area, with a section bounded by the planes *P* and *P'*, having coordinates *x, x + dx,* respectively. This configuration is also depicted in Fig. 1.12 below.

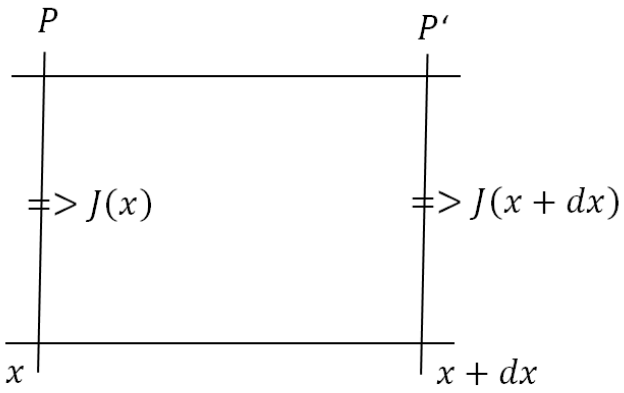

Fig. 1.12: One dimensional time dependent diffusion.

The quantity of material which is in the cylinder between P and P' must be equal to the change of the number of particles in a unit of volume as

$$\frac{dc}{dt} = -\frac{J(x + \Delta x, t) - J(x, t)}{\Delta x} \tag{1.34}$$

and in limit of an infinitesimally small stretch Δx

$$\frac{\partial c}{\partial t} = -\frac{\partial J}{\partial x} . \tag{1.35}$$

By combining equations (1.32) and (1.35) we can arrive on the general diffusion equation

$$\frac{\partial c}{\partial t} = \frac{\partial}{\partial x}\left(D\frac{\partial}{\partial x}\right) - \frac{\partial}{\partial x}(\langle v\rangle c) \tag{1.36}$$

which is a second-order partial differential equation. It cannot be solved analytically if D and $\langle v\rangle$ depend on concentration, thus on x and t. The diffusion equation becomes simpler if D and $\langle v\rangle$ are independent of concentration, which is applied for the case where the systems remain chemically homogeneous (e.g. self-diffusion). Then the equation (1.32) can be rewritten

$$\frac{\partial c}{\partial t} = D\frac{\partial^2 c}{\partial x^2} - \langle v\rangle\frac{\partial}{\partial x}. \tag{1.37}$$

In the case where the drift term is not present, equation (1.37) reduces to

$$\frac{\partial c}{\partial t} = D\frac{\partial^2 c}{\partial x^2}, \tag{1.38}$$

which is often inappropriately called Fick's second law. There are different analytical solutions for (1.37) and (1.38) corresponding to different initial and boundary conditions.

1.7 Solutions for the diffusion equation

In this section we will describe some simple cases in order to show the kinetics of diffusion by solving equation (1.38) with different analytical solutions.

1.7.1 Thin layer or instantaneous source

In this case the diffusing species is deposited as a "thin" layer on the surface of the sample or a sandwich like structure is considered, where the thin layer is between two identical samples. The initial condition is

$$t = 0, c(x, 0) = Q\delta(x) \tag{1.39}$$

Where δ indicates the Dirac delta function, defined as $\delta(x) = 0, x \neq 0$ and

$$\forall\, t, \int_0^\infty c\, dx = Q \qquad \text{or} \qquad \int_{-\infty}^\infty c\, dx = Q \tag{1.40}$$

where Q is the quantity of the deposited atoms per unit area and the integrals refer to a semi-infinite and infinite (sandwich-like) configuration, see also Fig. 1.13. The analytical solution for the sandwich geometry is

$$c(x, t) = \frac{Q}{2\sqrt{\pi D t}} exp\left(-\frac{x^2}{4Dt}\right). \tag{1.41}$$

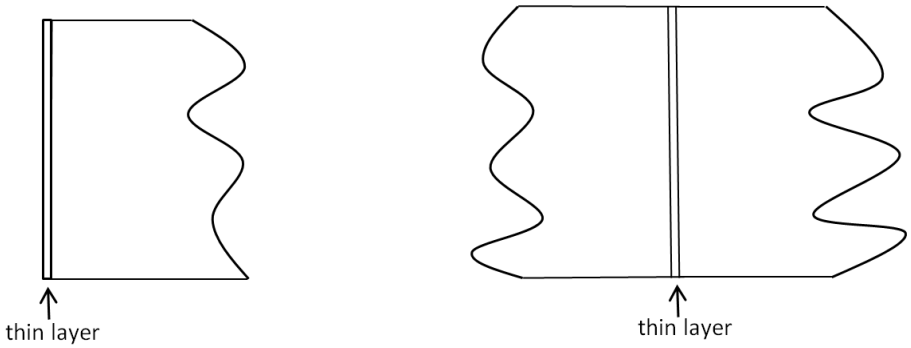

Fig. 1.13: A schematic view of the semi-infinite and infinite configuration.

For the surface deposition (semi-infinitive configuration), the factor *1/2* is removed from the pre-exponential. That is an equation of a Gaussian, which decays as the

square root of time and broadens as a function of $x/2\sqrt{Dt}$. The Gaussian can be also written as $exp(-\frac{x^2}{2w^2})$, where w is a width defined as $w = \sqrt{2Dt}$. The quantity $\sqrt{2Dt}$ is a measure of the penetration depth, see also Fig. 1.14.

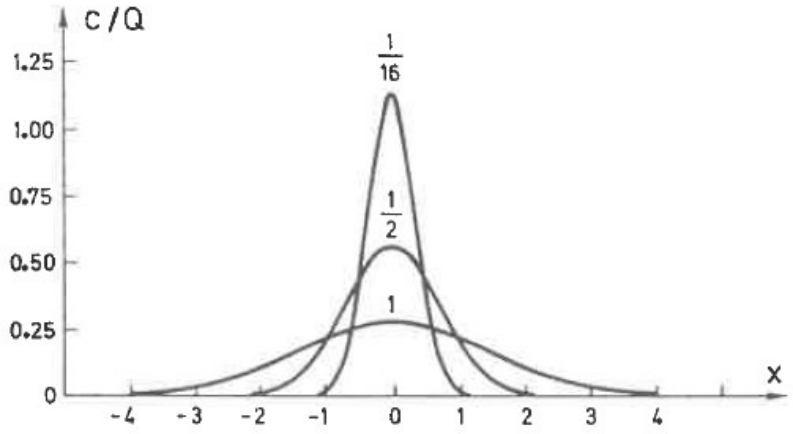

Fig. 1.14: Time dependence of concentration profiles for thin layer diffusion. The numbers on the curves relate to the values of *Dt* **[31]**.

For real measurements, the logarithm of the concentration against x^2 is plotted and D is calculated from the slope of the straight line. The validity of the experiment is indicated by the correlation of the measured points with the analytical solution. The fact that diffusion leads to a Gaussian distribution of the diffusing atoms means that the atoms move randomly under an effect of moving force.

1.7.2 Constant surface concentration

Initial conditions: t $= 0, x > 0, c(x, 0) = c_0$. Boundary conditions: all $t > 0, x = 0,$ $c(0, t) = c_s$. The solution is

$$\frac{c - c_s}{c_0 - c_s} = erf\left(\frac{x}{2\sqrt{Dt}}\right) \tag{1.42}$$

where *erf* means the error function on error integral of Gauss

$$erf\, z = \frac{2}{\sqrt{\pi}} \int_0^z e^{-u^2} du \ . \tag{1.43}$$

Two cases of equation (1.42) are particularly interesting:

1) $c_s = 0$

$$\frac{c}{c_0} = er\, f\left(\frac{x}{2\sqrt{Dt}}\right); \tag{1.44}$$

From the above equation, the outward flux at the surface is $Dc_0/\sqrt{\pi Dt}$ and the total quantity of substance that escapes by diffusion across a unit area of surface in time *t* is:

$$M(t) = \int_0^t \frac{Dc_0}{\sqrt{\pi Dt}} dt = 2c_0 \sqrt{\frac{Dt}{\pi}}. \tag{1.45}$$

As an example of this case we can choose the decarburization of steel in an oxidizing atmosphere or the dezincification of brass under vacuum (Fig. 1.15a).

2) $c_0 = 0$

$$\frac{c}{c_s} = erf\, c\left(\frac{x}{2\sqrt{Dt}}\right); \tag{1.46}$$

Where "*erfc*" is the complementary error function defined as $1 - erf$. Example for this kind of diffusion is a diffusion from an atmosphere, that in equilibrium, keeps the surface concentration constant (Fig. 1.15b). The quantity of material which diffuses into the solid per unit area is:

$$M(t) = 2c_s \sqrt{\frac{Dt}{\pi}}. \tag{1.47}$$

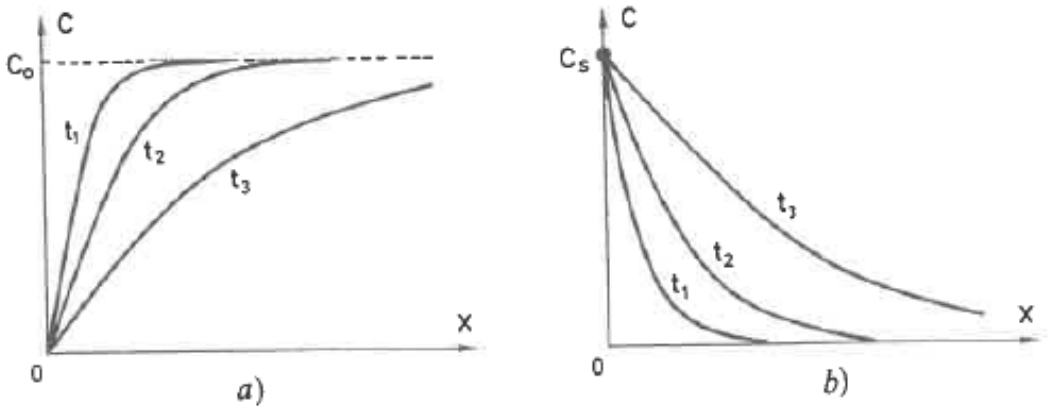

Fig. 1.15: Evolution of the concentration profiles with the time of diffusion: a) out-diffusion; b) in-diffusion; $t_1 < t_2 < t_3$ **[31]**.

In real life measurements one plots $erf^{-1}(c/c_0)$ or $erfc^{-1}(c/c_s)$ *vs*. *x* or *vs*. $x/\sqrt{t}$. After it, one must hope that the data plotted will form a straight line, in which case *D* can be calculated from the slope of the line. The practical difficulty appears in determining c_s, which is not always known with the necessary precision and one most vary both *D* and c_s. Besides, the condition $c_s = constant$ cannot always be proven, since the introduction of the diffusing species may take place by means of chemical reactions or the process of absorption. These processes may be rate determining, in which case the flux into solid is given by:

$$J(0,t) = K[c_s^0 - c_s(t)] \tag{1.48}$$

where *K* is the reaction rate constant (the reaction is assumed to first order), and $c_s(t)$ and c_s^0 are the real equilibrium surface concentrations. The solution of Fick's equation then becomes

$$\frac{c - c_0}{c_s^0 - c_0} = erfc\left(\frac{x}{2\sqrt{Dt}}\right) - \exp(hx + h^2Dt)\, erfc\left(\frac{x + 2hDt}{2\sqrt{Dt}}\right) \tag{1.49}$$

wherein *h=K/D*. It can be verified for the limiting case $h \to 0$, equation (1.49) predicts no diffusion ($c - c_0 = 0$), whereas for $h \to \infty$, the erfc solution is obtained, as the second term of (1.49) goes to zero.

Nonetheless, in the solution for constant surface concentration, the *x* coordinate of a plane parallel to the surface and at which the concentration remains constant with time is given by $x/2\sqrt{Dt} = constant$, which means that this plane moves as the square root of time. This result is typical for the diffusion: the penetration depth varies with the square root of the time. The same is true for the amount of diffusant introduced or lost (equations 1.44 and 1.46).

1.7.3 Infinite initial distribution

In this case the initial condition is a step function at *x = 0*

$$t = 0 \begin{cases} x < 0 & c = c_2 \\ x > 0 & c = c_1 \end{cases}$$

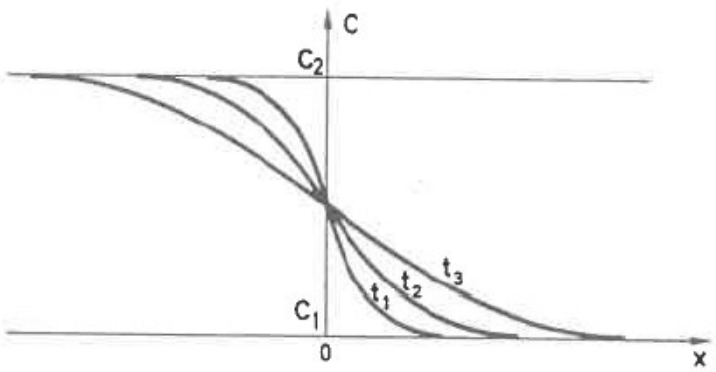

Fig. 1.16: Interdiffusion: evolution of the concentration profile with time. $\boldsymbol{t_1 < t_2 < t_3}$ **[31]**.

For symmetry reasons, the concentration at the initial interface (*x=0*) remains constant at the value of $\frac{1}{2}(c_1 + c_2)$. By substituting this value for c_s and $c_1$for $c_0$in equation (1.42) we arrive on

$$\frac{c-c_1}{c_2-c_1}=\frac{1}{2}erfc\left[\frac{x}{2\sqrt{Dt}}\right]. \tag{1.50}$$

The two branches of the solution are symmetrical with respect to the initial interface at *x=0* (Fig. 1.16).

1.7.4 The Boltzmann transformation

Since many of the previous solutions contain the combination $x/2\sqrt{Dt}$, we can try to define a useful variable to us as $\lambda = x/\sqrt{t}$. This substitution is known as the Boltzmann transformation and can be applied in cases where the initial and boundary conditions are themselves function of only the variable λ. Thus,

$$\frac{d}{dx}=\frac{d}{d\lambda}\frac{d\lambda}{dx}=\frac{1}{\sqrt{t}}\frac{d}{d\lambda}$$

and

$$\frac{\partial}{\partial t}=\frac{d}{d\lambda}\frac{\partial\lambda}{\partial t}=-\frac{\lambda}{2t}\frac{d}{d\lambda}$$

the Boltzmann transformation converts the partial differential diffusion equation

$$\frac{\partial c}{\partial t}=\frac{\partial c}{\partial x}\left(D\frac{\partial c}{\partial x}\right) \tag{1.51}$$

into a second order ordinary differential equation:

$$-\frac{\lambda}{2}\frac{dc}{d\lambda}=\frac{d}{d\lambda}\left(D\frac{dc}{d\lambda}\right) \tag{1.52}$$

the solution of which is concentration dependent on lambda $c(\lambda)$. When D is constant, that is independent of λ, the above equation simplifies to

$$\lambda \frac{dc}{d\lambda} = -2D \frac{d^2c}{d\lambda^2}, \tag{1.53}$$

Which can be with ease integrate

$$c(\lambda) = A + B\ erf(\lambda/2\sqrt{D})$$

or (1.54)

$$c(x,t) = A + B\ erf(\lambda/2\sqrt{Dt})$$

where A and B are constants to be determined from the boundary and initial conditions. The above solution applies to the case of constant surface concentration (chap. 1.7.2) and the infinite distribution (chap. 1.7.3) but not the instantaneous source (chap. 1.7.1), since there the initial conditions are given in terms of *x,* instead of λ.

1.7.5 The relation of drift and diffusion - The Nernst-Einstein equation

The combined effect of diffusion and driving force can lead to a steady state in a case where both effects are equal and in opposite sign.

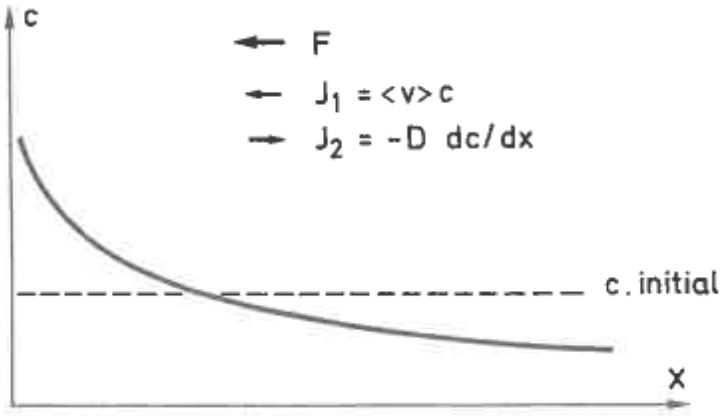

Fig. 1.17: Concentration profile under a driving force compensated by diffusion **[31]**.

$$J = 0 \rightarrow D\frac{\partial c}{\partial x} = \langle v \rangle\, c \tag{1.55}$$

We will assume that the applied force is a derivative of a potential $F = -d\Phi/dx$. In a thermodynamic equilibrium the distribution of the species under our consideration should follow the Boltzmann distribution:

$$c(x) = const.\, exp[\phi(x)/kT]. \tag{1.56}$$

The above expression should be the solution of the (1.55) equation at steady state. Differentiating with respect to *x* results in

$$\frac{dc}{dx} = -\frac{c}{kT}\frac{d\phi}{dx} = \frac{cF}{kT}\ , \tag{1.57}$$

and substituting it into (1.55) we can obtain

$$\frac{\langle v \rangle}{D} = \frac{F}{kT}\ . \tag{1.58}$$

This is the Nernst-Einstein equation. If the driving force is due to an electric field, then for the particles with charge q; $F = qE$. After introducing the mobility of electrons as $\langle v \rangle = \mu E$, the Nernst-Einstein equation becomes

$$\frac{\mu}{D} = \frac{q}{kT} \ . \tag{1.59}$$

Fick's equation can be also rewritten as

$$J = -D\frac{\partial c}{\partial x} + \frac{D}{kT}Fc \ . \tag{1.60}$$

If an electric field is present, the charged particles q migrate with velocity $\langle v \rangle$, from which the drift flux is:

$$J = \langle v \rangle c = \frac{FDc}{kT} = \frac{qcD}{kT}E \ ,$$

and the current density

$$i = qJ = \frac{cq^2D}{kT}E \ ,$$

which can be seen as Ohm's law, where the electrical conductivity is given by

$$\sigma = \frac{cq^2D}{kT} \ . \tag{1.61}$$

1.7.6 Solution of the Diffusion equation in three dimensions

If the diffusion is isotropic in a medium, the flux is

$$J = -D\,\nabla c \tag{1.62}$$

and the diffusion equation is given by

$$\frac{\partial c}{\partial t} = D\,\nabla^2 c\ . \tag{1.63}$$

The equation in Cartesian coordinates is as follows

$$\frac{\partial c}{\partial t} = D\left[\frac{\partial^2 c}{\partial x^2} + \frac{\partial^2 c}{\partial y^2} + \frac{\partial^2 c}{\partial z^2}\right], \tag{1.64}$$

in cylindrical coordinates

$$\frac{\partial c}{\partial t} = \frac{D}{r}\frac{\partial}{\partial \mathrm{r}}\left(r\frac{\partial \mathrm{c}}{\partial \mathrm{r}}\right), \tag{1.65}$$

in spherical coordinates

$$\frac{\partial c}{\partial t} = \frac{D}{r^2}\frac{\partial}{\partial \mathrm{r}}\left(r^2\frac{\partial \mathrm{c}}{\partial \mathrm{r}}\right). \tag{1.66}$$

1) Cylindrical coordinates

By separation of variables we can arrive on terms of type $J_0(\alpha_n r)\exp(-\alpha_n^2 Dt)$, where J_0 is the Bessel function of zeroth order. For steady state, equation (1.65) becomes

$$\frac{d}{dr}\left(r\frac{dc}{dr}\right) = 0\ , \tag{1.67}$$

and the general solution can be written as

$$c = A + B\ log\ r \tag{1.68}$$

with constants A and B determined by the boundary conditions.

2) Spherical coordinates

Let $u = rc$, equation (1.66) can be rewritten as follows

$$\frac{\partial u}{\partial t} = D\frac{\partial^2 u}{\partial r^2} \ . \tag{1.69}$$

The above equation is easily solved by separation of variables if u goes to zero as r becomes very large. For steady state

$$\frac{d}{dr}\left(r^2\frac{dc}{dr}\right) = 0 \ , \tag{1.70}$$

the general solution can be written as

$$c = (A/r) + B \ , \tag{1.71}$$

where the constants A and B are again determined by the boundary conditions.

1.8 Transport properties

In thermodynamic equilibrium the distribution function for the electrons can be described by the Fermi-Dirac function

$$f_0(E) = \frac{1}{1 + e^{(E-E_F)/kT}} \ , \tag{1.72}$$

where E_F is called the Fermi energy and $f_0(E)$ is the probability of a state at energy E occupied by an electron. In a non-equilibrium state a system of electrons can be described by the following general function

$$f\left(v_x, v_y, v_z, x, y, z, t\right)dv_x dv_y dv_z dx dy dz = f(v, r, t)d^3v d^3r \ . \tag{1.73}$$

We can study the changes of this function for a time frame in the dimensions of *r* and *v*, and we can arrive on the following terms

$$\frac{\partial f}{\partial t} = -v\nabla_r f - \frac{1}{m}F(\nabla_v f)\,. \tag{1.74}$$

Wherein the first term on the right side corresponds for the location and the second term corresponds to the velocity. We arrived on those terms by time derivation of function *f*:

$$\frac{\partial f}{\partial t} = \frac{\partial f}{\partial t} + \frac{\partial f}{\partial r}\frac{\partial r}{\partial t} + \frac{\partial f}{\partial v}\frac{\partial v}{\partial t}\,. \tag{1.75}$$

Both terms are multiplied by the time derivation of *r* and *v*. *F* stands for the force applied on the electron ($\dot{v} = F/m$). The number of electrons also changes by mutual collisions or by the collisions on the boundaries of the system, which will lead us to introduce a field term. Besides, we also introduce a function $W(v, v')d^3v'dt$ which will be the probability of changing the velocity of an electron from *v* to *v'* in the *dt* time frame:

$$-\int f(v, r, t)W(v, v')d^3v d^3r d^3v'\, dt. \tag{1.76}$$

This analogy can be applied also for electrons with velocity of *v'* which will regain velocity *v* after a collision

$$\int f(v', r, t)W(v, v')d^3v d^3r d^3v'\, dt\,. \tag{1.77}$$

Thus, the final number of electrons in a non-equilibrium state will be stated by the following equation

$$\frac{\partial f}{\partial t} = -v\nabla_r f - \frac{1}{m}F(\nabla_v f) + \int f(v', r, t)W(v, v') - f(v, r, t)W(v, v')d^3v' \tag{1.78}$$

known as Boltzmann's kinetic equation.

If we take a closer look for solving the above Boltzmann's kinetic equation, based on [32], for a sample which is homogeneous and macroscopic, with a weak conduction layer at the surface and without mesoscopic effects, we can arrive on the following. Firstly, we will assume that the bands are spherical, the heavy-hole (hh) band is parabolic and electron (e) and light-hole (lh) bands as well as wave functions are described in the *kp* approximation by the Kane formulae. A general form of the electric Boltzmann transport equation for the steady state system for transport in an external electric *E* and magnetic *B* fields and temperature gradient is

$$\left(\frac{\partial f}{\partial t}\right) = v \cdot \nabla_r f - \frac{e_\lambda}{\hbar}(E + v \times B) \cdot \nabla_k f, \tag{1.79}$$

where e_λ is the charge of respective free carriers (λ = *e, hh, lh*) and the velocity is given by the energy gradient $v = \nabla_k \varepsilon_{\lambda k}/\hbar$. The distribution function f in each band is looked for in a form

$$f(k) = f_0(\varepsilon) + f_1(k) \tag{1.80}$$

f_0 is the Fermi–Dirac function. In the linear response

$$\nabla_r f \approx \nabla_r f_0 = \frac{\partial f_0}{\partial \varepsilon} T \nabla_r \left(\frac{\varepsilon - E_F}{T}\right) \tag{1.81}$$

E_F is the Fermi energy. If we assume the following orientations *E = (E, 0, 0), B = (0, 0,B)* and $\nabla_r T = (T', 0, 0)$. Function f_1 can be written as a combination of two functions c_1 and c_2 :

$$f_1(k) = [k_1 c_1(\varepsilon) + k_2 c_2(\varepsilon)]\left(-\frac{\partial f_0}{\partial \varepsilon}\right), \tag{1.82}$$

k_1 and k_2 are the wave vector components. Equation (1.79) can be split into a set of two equations, which relate to the transport in the E parallel and perpendicular directions, respectively:

$$v_1\left(-\frac{\partial f_0}{\partial \varepsilon}\right)\left(\frac{\varepsilon - E_F}{T}T' + \nabla_r E_F - e_\lambda E - \frac{e_\lambda}{\hbar}Bc_2\right) = L(k_1c_1), \tag{1.83}$$

$$v_2\left(-\frac{\partial f_0}{\partial \varepsilon}\right)\frac{e_\lambda}{\hbar}Bc_1 = L(k_2c_2), \tag{1.84}$$

$L(k_ic_i), i = 1{,}2$ is the scattering operator given in the form:

$$L(k_ic_i) = -\frac{1}{k_BT}v\sum_{k'}W(k,k')f_0(\varepsilon_k)[1 - f_0(\varepsilon_{k'})] \times [k_ic_i(\varepsilon_k) - k_i'c_i(\varepsilon_{k'})]. \tag{1.85}$$

W(k,k') is the *k*⟶*k'* scattering probability. If interband scattering is involved, the distribution function for each band is defined. Then the sum in (1.85) also contains band summations where *k'* specifies the respective bands.

The relevant dc transport coefficients are obtained in the following form. The electrical conductivity tensor $\sigma_{ij} = \sum_{\lambda=e,hh,lh}\sigma_{ij}^{\lambda}$ where the particular terms represent the *e, hh* and *lh* conductivities:

$$\begin{Bmatrix}\sigma_{11}^{\lambda} = \sigma_{22}^{\lambda}\\ \sigma_{21}^{\lambda} = -\sigma_{12}^{\lambda}\end{Bmatrix} = \frac{e_\lambda}{3\pi^2\hbar}\int_0^\infty k_\lambda^3(\varepsilon)\begin{Bmatrix}c_1^{\lambda}(\varepsilon)\\ c_2^{\lambda}(\varepsilon)\end{Bmatrix}\left(\frac{\partial f_{0\lambda}}{\partial \varepsilon}\right)d\varepsilon, \left[E - \frac{\nabla E_F}{e_\lambda} = 1,\ T' = 0\right]. \tag{1.86}$$

Hall coefficient:

$$R_H = \frac{1}{B}\frac{\sigma_{12}}{\sigma_{11}^2 + \sigma_{12}^2} \tag{1.87}$$

2. Experimental setups

2.1 Crystal growth

For our galvanometric measurements we used CdTe crystals, grown in the Institute of Physics of the Charles University by Vertical-gradient freezing (VGF) method. The growth of VGF crystal was performed in two-steps. In the first step, 6N starting materials Cd and Te were synthesized in the synthetization furnace. The materials were put in a quartz ampoule with inner walls covered by graphite. The ampoule was evacuated up to 5×10^{-6} mbar, sealed and put into a one-zone synthetization furnace, which was heated up to 450°C, where the materials started to melt. Due to the strong endothermic reaction during the synthesis, the temperature of the ampoule was slowly heated up to 1100°C. The molten material was held on this temperature for 10 hours for homogenization and cooled down to room temperature with a cooling rate of 3°C/min. The obtained solid material was used as a starting material for the second growth step, single crystal growth using VGF technique.

Single-crystalline samples were cut from the CdTe ingot with a diameter of about 40 mm. Samples were high-quality intentionally undoped p-type single crystals with hole mobility close to published data [13]. Bar-like samples with the resistivity in the range from 200 to 400 Ωcm and typical dimensions of 3x2x12 mm^3 were used in our investigation.

2.2 Sample preparation

The CdTe ingot was sliced perpendicularly on the growth direction in order to cut wafers of 2-3 mm thickness. This cut was made by a diamond wire saw Well Diamond Wire Saws Inc. (model 6234) with wire diameter 0.3mm (cooled by water). The wafers were polished by boron carbide abrasive SiC F600 to reveal the structure of grains of the wafer. Consequently, bar-shaped (or squared) monocrystalline samples were cut from wafers by a wire saw South Bay Technology Inc. (model 850) using stainless steel wire with diameter of 0.1mm (with abrasive boron carbide-glycerine solution). After cutting, the samples were polished using finer SiC abrasive

F1000 followed by a chemo-mechanical polishing in 3% bromine-ethylene glycol solution on the silk cloth. Process was performed for 30 seconds each side. Finally, samples were etched in 3% bromine-methanol solution for 30 seconds to obtain shiny surfaces. After the etching process, each crystal was washed in ethanol and acetone. Finally, the samples were dried in clean air flow to remove any residual products from and etching process.

2.3 Contact preparation

After the etching process, the samples were covered by a photoresist in order to form six chemically-deposited golden contacts. The photoresist material was then hardened at 60°C for a period of 20 min. The masked sample was immersed into $AuCl_3$ solution to create chemically-deposited Au contacts on the uncovered portions of the sample. After the chemical deposition, the photoresist mask was removed by a lift-off technique in acetone. The samples were then glued on a sapphire pad (Fig. 2.1) with golden conductive channels by thermally conductive silicon paste. Gold channels on the holder were connected with the golden contacts on the sample by silver wires with a diameter 50μm. Besides wire soldering, dipping by graphite paste was also used to fix the wires to the crystal. This type of contact was used for temperatures above 140°C. Both types of contacts possessed good ohmic properties and were stable. The sapphire pad was attached to a holder and put into a cryostat, wherein the temperature dependence of the galvanomagnetic properties were measured. For higher temperature dependence measurements, the STVP-300 continuous flow cryostat from Janis Research was used. Here, the wires from the sample were connected by tin to the pins of the sample holder. In the cryostat, the sample chamber was filled with inert gas during the measurements.

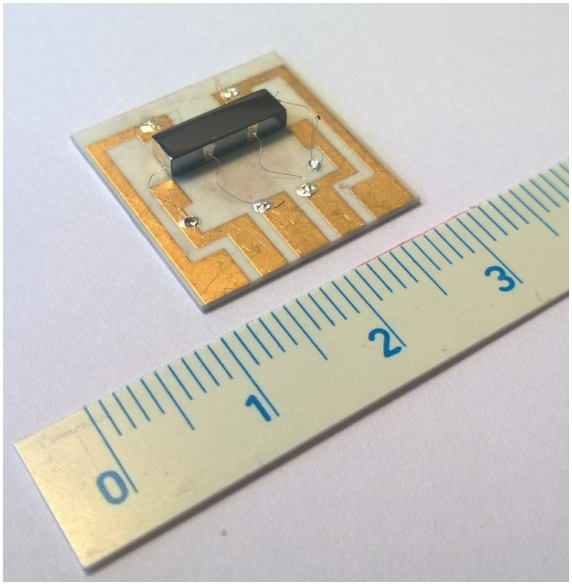

Fig. 2.1: Bar-like sample of CdTe crystal with six chemically-deposited golden contacts soldered by indium.

2.4 Transport measurements

The measurement of the carrier concentration, electron/hole mobility, and conductivity was carried out by Hall-effect measurements with the classical method setup. For this method, four voltage probes are considered, which are divided in pairs on the two lateral sides of the sample. Further, two current contacts are located on the front and back side of the sample, more particular from Fig. 2.2.

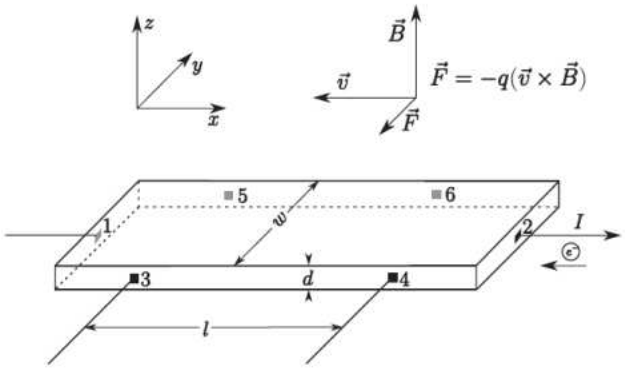

Fig. 2.2: Classical arrangement for the Hall-effect measurements **[33]**.

For the above configuration, while the current flows from contact 1 to contact 2 and the magnetic field B is non-zero, the potential change E_Y along axis y can be described as follows:

$$E_Y = R_H B_z J_x \,. \tag{2.1}$$

The Hall coefficient R_H is defined as [34] :

$$R_H = r_H \frac{p\mu_p^2 - n\mu_n^2}{e\left(n\mu_n + p\mu_p\right)^2} \,. \tag{2.2}$$

Wherein, n and p are the electron and hole concentrations; μ_n and μ_p are the electron and hole mobilities; e is the elementary charge of the electron and r_H is the Hall factor, which is approximately 1 for our measurements. For the cases where we can neglect one type of the carriers we get a simpler equation, in case of holes the following:

$$R_H = r_H \frac{1}{ep} . \tag{2.3}$$

That is, the Hall coefficient is inversely proportional with the concentration of the charge carriers (i.e. holes in our case). For measuring the conductivity, we use the following equations:

$$\sigma = \frac{1}{\rho} = \frac{l}{dw}\frac{I_{1,2}}{U_{3,4}}, \tag{2.4}$$

$$\sigma = \frac{1}{\rho} = \frac{l}{dw}\frac{I_{1,2}}{U_{5,6}}. \tag{2.4'}$$

That is, we replace in the above equations l, d and w with the actual distance between contacts, width, and thickness of the sample, respectively. The current measured between contacts 1 and 2 and potential change measured between contacts 3 and 4

(or 5 and 6) with the aforementioned dimensions will enable us to get the conductivity of the sample.

For measuring the carrier concentration, or rather the Hall coefficient, we use the following equations:

$$R_H = r_H \frac{d}{2B} \frac{U_{5,3}^{B+} - U_{5,3}^{B-}}{I_{1,2}}, \tag{2.5}$$

$$R_H = r_H \frac{d}{2B} \frac{U_{6,4}^{B+} - U_{6,4}^{B-}}{I_{1,2}}. \tag{2.5'}$$

Thus, we measure the potential change between the two facing voltage contacts 5 and 3 (or 6 and 4) while turning the magnetic field on and changing the polarity of the magnetic field. Deviations of σ and R_H evaluated by the relations (2.4), (2.5) and (2.4‘), (2.5‘), respectively, allowed us to eliminate an experimental error.

For the measurements we can consider a relative error of 10% in the length between the contacts and 2.5% in the thickness and width of the sample. The value of R_H is measured for 5s and its value is averaged. Thus, the error of R_H is dependent on the noise of the measured voltage signal from the sample. The error of the voltmeter and ampere meter is less than 1%. For keeping the magnetic field constant a continuous cooling is applied. Despite of it, variance in the magnetic field can also be present, which can be estimated as 5%. The sum of the errors for the conductivity is 15% and for R_H is 7.5%. However, during the stepwise and continuous temperature changes all the dimensions of the sample remain the same and the apparatus also. Thus, for our measurements the characters of the temperature dependencies are not influenced by the before mentioned errors.

2.5 SIMS and XPS measurements

For the X-ray photoelectron spectroscopy (XPS) measurements the samples were investigated in an ultrahigh vacuum chamber (UHV) equipped with a VSW HMA-100 hemispherical analyzer with multichannel detection provided by PSP Vacuum

Technology. The data were taken using an Al Kα excitation (1486.6 eV) at normal emission angle with respect to the sample surface. The Secondary Ion Mass Spectroscopy (SIMS) experiments were performed in an UHV chamber equipped with Perkin-Elmer PHI 600 mass spectrometer. SIMS was operated at "dynamic" conditions of Cs primary ion gun with the energy of 5 keV and current 100 nA, approximately, giving the sputtering rate of 50 nm / min, approximately. The Cs ion beam was scanned over the crater raster area of 800 x 500 μm^2. In order to obtain well resolved depth profiles and to minimize crater effects, the gating technique of secondary ion detection was used. For both, XPS and SIMS analysis, the base pressure was below 10^{-7} Pa and the samples were kept at room temperature during measurements.

2.6 Ellipsometry

Ellipsometry is a non-destructive optical technique, which proved itself as an effective tool to acquire optical properties of matter with high surface sensitivity [35]. It measures changes in light polarization upon reflection from the sample. These changes are represented by ellipsometric angles Ψ and Δ, which are related to Fresnel reflection coefficients for s- and p-polarized light by:

$$\rho = \frac{r_p}{r_s} = \tan(\Psi)\, e^{i\Delta}\,. \tag{2.6}$$

Therefore, with proper choice of a theoretical model structure one can fit the experimental data and deduce spectrally dependent optical properties of investigated material as well as the thickness of the surface layer. In our case, the model structure for the distilled water consisted of a semi-infinite bulk CdTe material with the surface oxide layer of certain thickness and roughness. An assumption of semi-infinite CdTe is justifiable with respect to its high absorption coefficient in the investigated spectral region and a large thickness of the sample. A commercial Mueller matrix ellipsometer RC2 (J.A. Woollam Co., USA) was used to obtain the experimental data in the spectral range from 200 to 1700 nm. To ensure a sufficiently large ensemble of experimental data necessary for high accuracy fitting, the

ellipsometry was measured in reflection for five different incident angles 55°, 60°, 65°, 70° and 75° with an acquisition time 60 s. The results were fitted using aforementioned model structure and the mean squared error (MSE) was used to evaluate the reliability of the fit. The error of Ψ and Δ are 0.02 and 0.05 degrees, respectively. The incident light spot diameter was 4 mm and therefore the acquired information was averaged over the whole surface.

2.7 Photoluminescence

Photoluminescence is a non-destructive optical method for studying material defects. Therefore, it is widely used for characterizing the structure of the material. Its main limitation is the fact, that this method can only reveal defects which have optical transitions. The samples are usually cold down to eliminate the thermal noise. The sample is irradiated with a laser and electron-hole pairs are generated, which are trapped on the defects in the material and after they recombine they might emit light. The energy of the emitted light corresponds to the energy level of the defect in the bandgap. By detecting all the emitted photons, we can obtain a photoluminescence spectrum. The schematic setup of our photoluminescence measurement is depicted on the below Fig. 2.3.

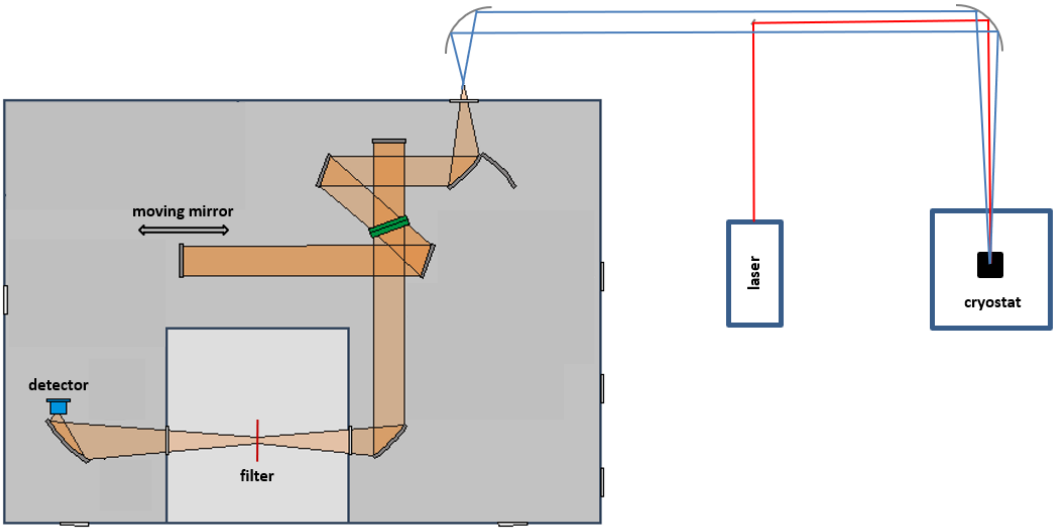

Fig. 2.3: The schematic setup of the photoluminescence measurement.

We used a Bruker Vertex 80v spectrometer with a Si detector for detecting the photoluminescence spectra. The sample was placed into a cryostat cooled down to a temperature lower than 10K and irradiated by a semiconductor laser with a wavelength of 635nm. The signal from the sample was filtered with the same wavelength to eliminate it from the spectrogram

3. Results

3.1 Thermal stability of p-CdTe

There are only a few literature data related to electrical measurements on bulk CdTe at temperatures of 300-700 K. Hall effect and electrical conductivity in the range of 310-420 K were studied in semi-insulating p-type CdTe:Cl crystals, where an anomalous increase of resistivity was observed [36]. Other measurements of electric properties in the range from 295 to 430 K were carried out for semi-insulating p-CdTe:Cl crystals wherein anomalous changes of electrical properties in the range 340-380 K were seen [37]. This anomaly was interpreted as the relocation of Cu atoms in the lattice of CdTe. The activation energy of 0.87 eV of this process was determined from the temperature dependence of relaxation time.

The reason for the low interest of researchers in measuring electric properties of CdTe in the temperature interval of a few hundred Kelvin above room temperature arises from the complexity of adjustment of the experiment and the interpretation of obtained results. At room or lower temperatures, the defect structure may be considered as stable, and transient phenomena are induced only by the charge dynamics and local defect rearrangement. The evaluation of high temperature measurements above 700 K may be based on defect structure ruled by native defects and their associates with extrinsic defects. The sufficiently fast chemical diffusion at such temperatures allows the researchers to reach defect equilibrium under defined thermodynamic conditions [38] within hours [39]. On the other hand, the experiments in the intermediate temperature interval of ~300-700 K cannot rely on these premises. Moderate heating of the sample induces point defect rearrangement involving diffusion and defect reactions. Simultaneously, the diffusion processes are too slow to establish the equilibrium unless the time of experiment is extremely extended. Consequently, the theoretical model describing envisaged effects must consider the dynamics of defect structure during the whole experiment.

Special attention must be devoted to fast diffusing impurities, typically group I elements Li, Na, Cu or Ag [40,41,42], which contaminate the material at the density 10^{14}-10^{15} cm^3 comparable to the hole concentration in p-CdTe. The presence of these impurities is often a problem in the fabrication of electronic devices and their elimination is a permanent goal in this field [43]. Complex features of diffusion of

Ag and Cu including anomalous diffusion of Ag atoms against their concentration gradient were extensively studied by radiotracer experiments [44,45]. In this work we report on the measurement of galvanomagnetic properties of p-type CdTe samples subjected to two distinct thermal treatments. In the first process, the relaxation of the hole density is measured after stepwise change of temperature. The activation energy of the relaxation process is determined thereon. In the second case the samples are heated and cooled continuously at a constant heating/cooling rate. Transients are simulated with a theoretical model assuming diffusion of a fast diffusing element from/into Te inclusions.

3.1.1 Stepwise temperature changes

As apparent in Figs. 3.1, 3.2 for Sample I and in Figs. 3.3, 3.4 for Sample II, which depict typical parts of the measuring cycle, the measurements consisted in the monitoring of the transport properties of the samples at the temperature steps.

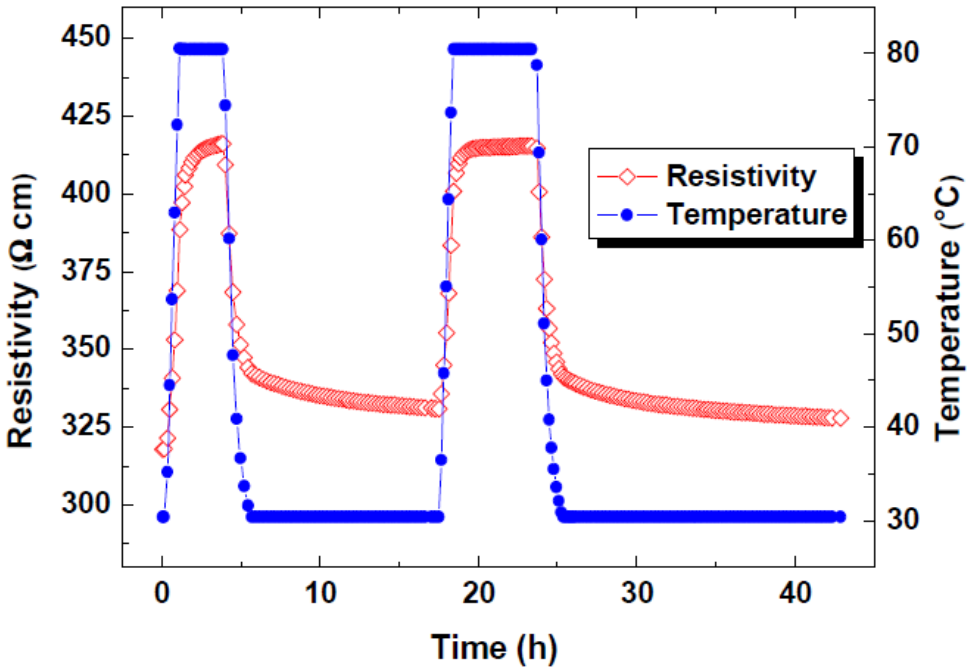

Fig. 3.1: Example of the resistivity evolution of Sample I at the temperature profile 30 -80-30-80-30°C.

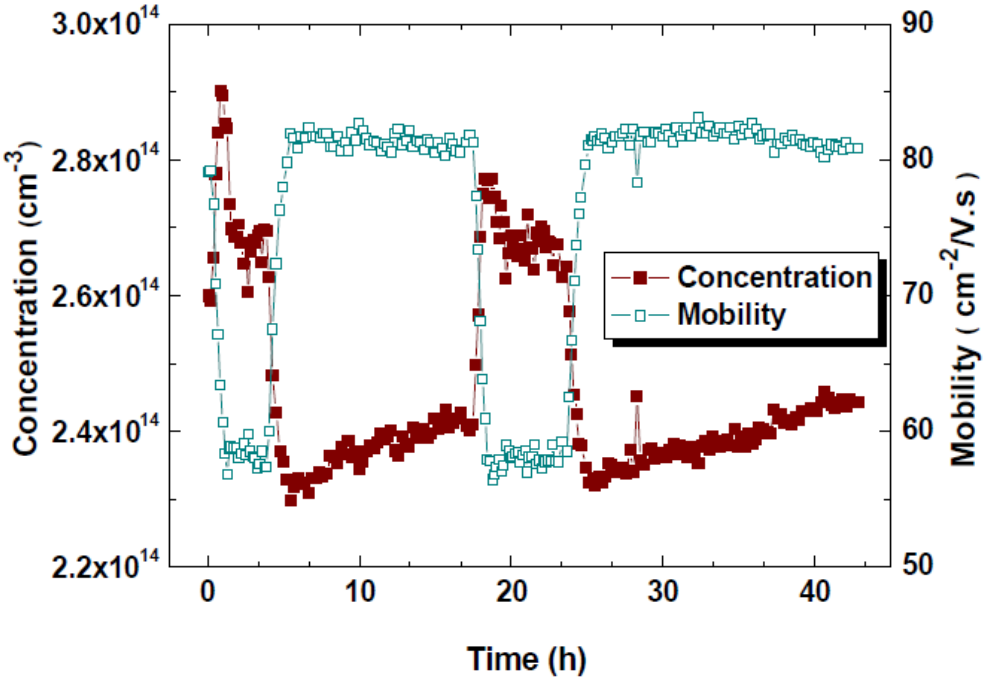

Fig. 3.2: Example of hole concentration and mobility evolution of Sample I at the temperature profile 30-80-30-80-30°C.

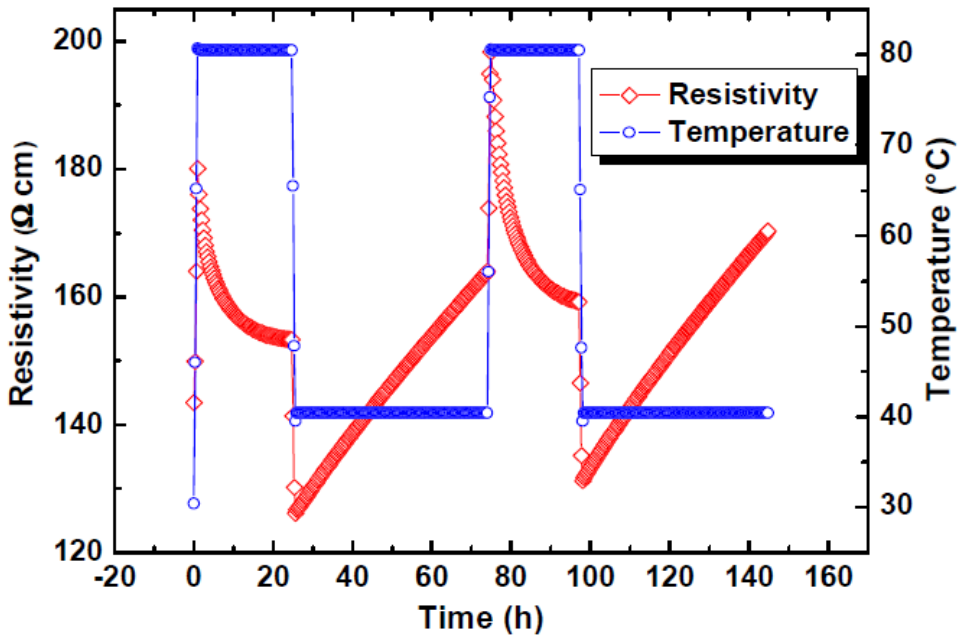

Fig. 3.3: Example of the resistivity evolution of Sample II at the temperature profile 30-80-40-80-40°C.

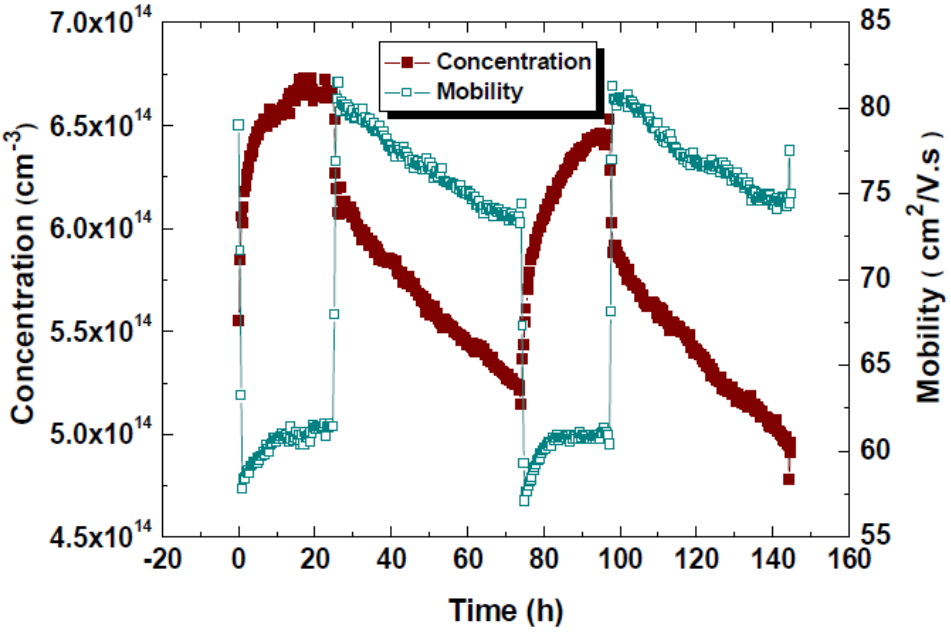

Fig. 3.4: Example of the hole concentration and mobility evolution of Sample II at the temperature profile 30-80-40-80-40°C.

In all figures, we may identify two characteristic features of the transport coefficient evolution. During the temperature changes - increase/decrease - we observe the parallel evolution of the resistivity. The increase of resistivity with raising temperature is unusual in semiconductors and it is explained by the damping of carrier mobility together with minor increase of free carrier density. This effect is often observed in low resistivity CdTe. After the temperature stabilization, few days evolution of transport characteristics is observed in both samples. While in Sample I we clearly see that the resistivity increases/decreases after the temperature step up/down, just an opposite behavior is identified in Sample II, where the temperature step up/down entails the resistivity decrease/increase. Thus, for the same type of p-type CdTe samples we observed different behavior of the resistivity relaxation. As seen in Fig. 3.2, the hole mobility was constant during the relaxation, and the hole concentration was increasing in the lower temperature and decreasing in the higher temperature in Sample I. In Sample II the mobility was slightly saturating in the higher temperature interval and, as seen in Fig. 3.4, slightly decreasing in the lower temperature interval. The hole concentration had similar characteristics as the mobility temperature dependence, except that in the lower temperature interval the

decrease was more rapid. The characteristic time of the relaxation varies from few hours at maximum temperature, as we can see in Fig. 3.1 and Fig. 3.2, up to weeks at minimum temperature, apparent in Fig. 3.3 and Fig. 3.4. For both samples we carried out the relaxation procedures with different lower temperatures. Since the relaxation of Sample I was relatively fast, we have succeeded to grasp principal part of the relaxation curve, which enabled us to find out an activation energy of the relaxation process and to estimate the diffusion coefficients of the relaxations assuming a diffusion between the sample bulk and surface responsible for the relaxation [46]. Evaluation of the diffusion coefficient D of the sample I is depicted in Fig. 3.5 – 3.7.

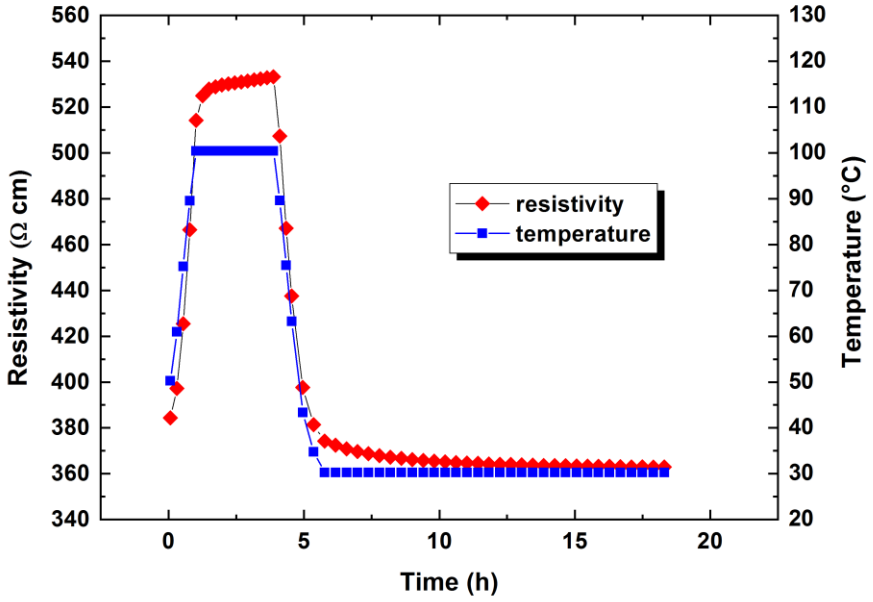

Fig. 3.5: The resistivity evolution of Sample I at the temperature region 100-30°C.

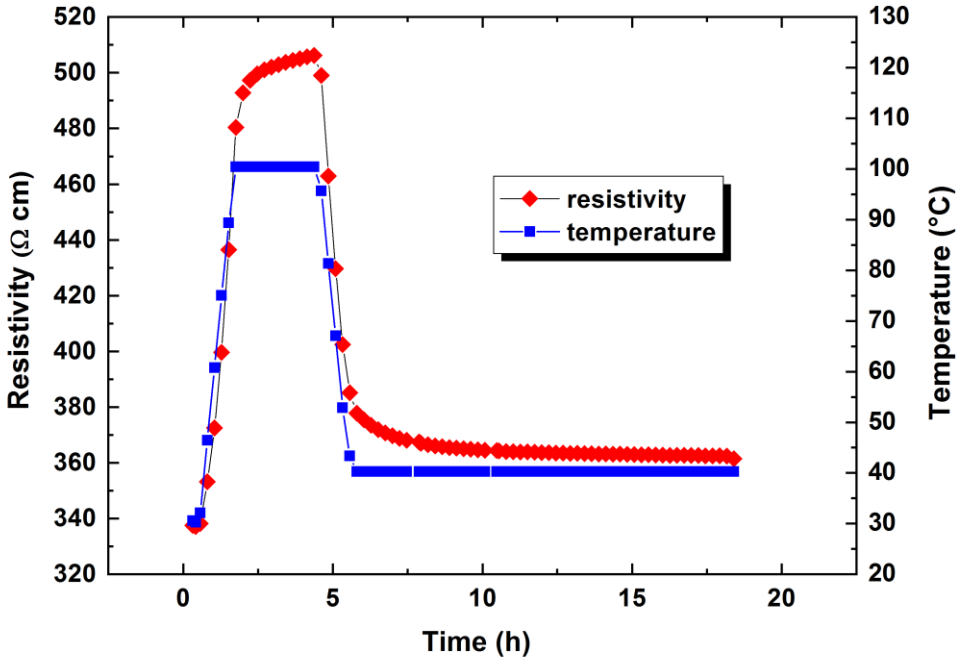

Fig. 3.6: The resistivity evolution of Sample I at the temperature region 100-40°C.

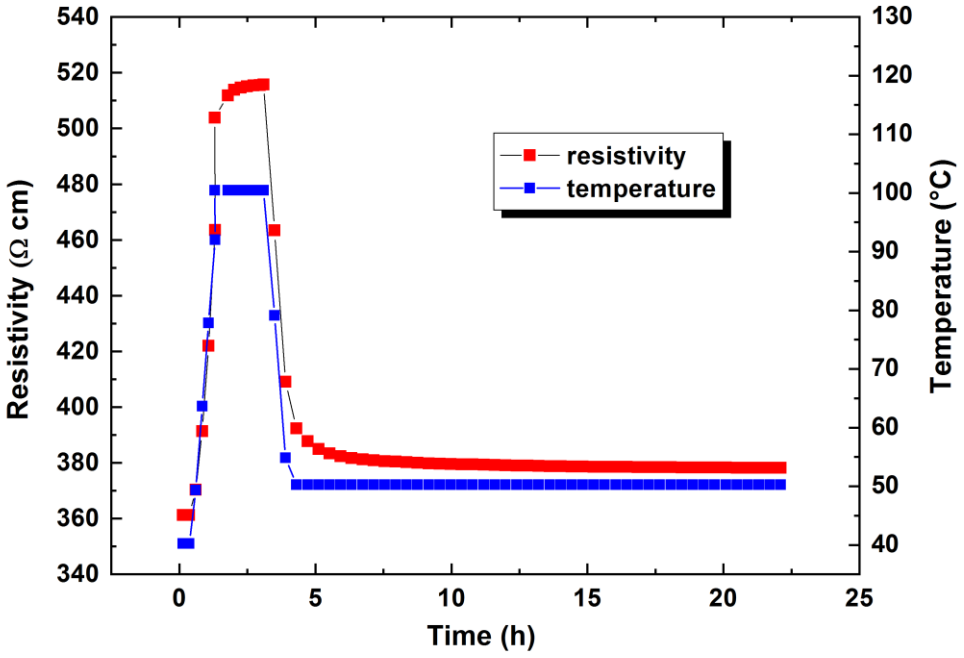

Fig. 3.7: The resistivity evolution of Sample I at the temperature region 100-50°C.

The above graphs 3.5 – 3.7 show a typical behavior of Sample I and its resistivity relaxation. As already said the fast relaxation of Sample I allowed us to determine the diffusion coefficient and the activation energy of the process. The diffusion coefficient D is determined by the fit of conductivity via the form [46]:

$$|\sigma(t) - \sigma_\infty| \sim exp\left(-\frac{Dt\pi^2(w^2+d^2)}{w^2d^2}\right). \qquad (3.1)$$

The conductivity fit of the relaxation is illustrated on the following Fig. 3.8. The solid line in the graph represents the fit of the left side of equation (3.1). In the equation (3.1) *w* and *d* refer to the cross-sectional dimensions of the sample (width and height) and *t* represents the time.

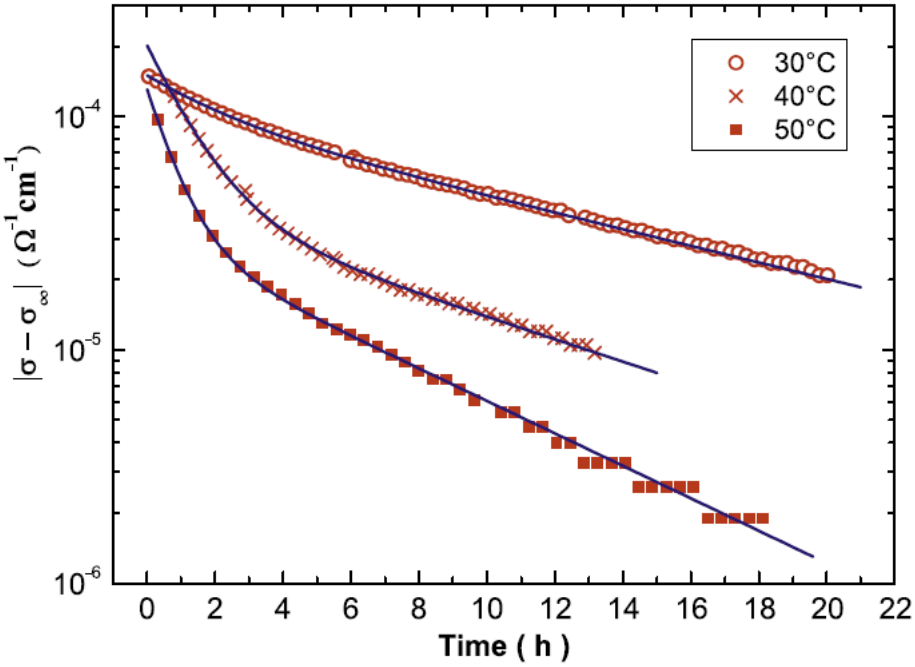

Fig. 3.8: Double-exponential fit of the conductivity after stepwise change of temperature of Sample I.

Analogous evaluations were carried out in order to obtain the activation energy for temperatures 30 and 40°C. As it is apparent in Fig. 3.9, the corresponding diffusion coefficients were well aligned, thus we were able to determine the activation energy of the relaxation for Sample I to about 0.3 eV.

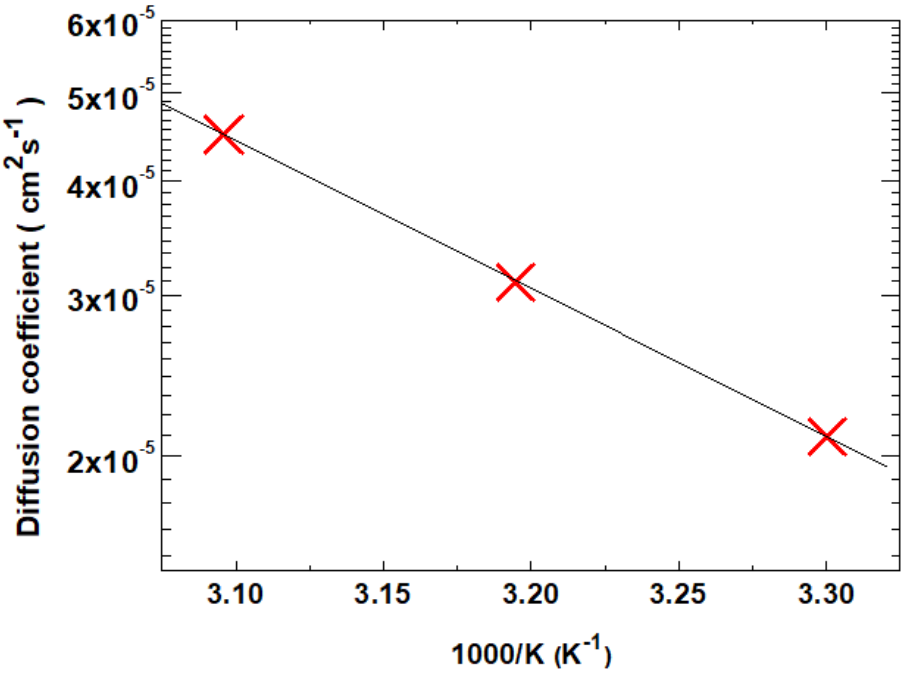

Fig. 3.9: Temperature dependence of diffusion coefficients for Sample I.

The diffusion coefficient of the type I relaxation results as:

$$D = D_0 e^{-E/k_b T} = 2.4e^{-0.3eV/k_b T}\ (cm^2 s^{-1}). \qquad (3.2)$$

We also compared our measured diffusion coefficients, which were in the range of 3.5×10^{-6} – 7.5×10^{-6} cm^2s^{-1}, with the already published results of Lyubomirsky [47], Jones [48] and Belas [43], showing a good correlation with the latter one, where D~3×10^{-6} - 4×10^{-6} cm^2s^{-1} at 100°C was reported. The electro-diffusion measurements [43] of CdTe showed that the fast diffusing impurities/defects in p-type CdTe samples are donors, thus we assume analogous character of defects in our case. The nature of contaminating donors is unknown yet. Group I elements Li, Na, Cu, Ag, are mostly presumed [43]. Impurities may originate from the source 6N elements, quartz ampoule in which the crystal is grown and from ambient conditions together with the outside effects during the sample preparation and contacting procedure.

From the measurement of the hole relaxation, we could estimate the density of the donors, which is connected to the change of the hole concentration during the relaxation procedure. The estimated donor concentration for Sample I is ~ $10^{13}cm^{-3}$

while the mobility had constant character during the relaxation, which reflects good crystal quality. For Sample II the estimated donor concentration is ~ $10^{14}cm^{-3}$ while the mobility was slightly decreasing which can be connected to the non-homogeneity of the sample. The aforementioned concentration values are at the resolution limits of the glow discharged mass spectroscopy (GDMS). For the identification of elements possibly responsible for reported phenomena the secondary ion mass spectroscopy (SIMS) measurements are required.

3.1.2 Summary of the stepwise temperature changes

The thermal stability of two p-type CdTe single crystals cut from different parts of as grown ingot was studied by conductivity and Hall-effect measurements. Step-like change of temperature in the interval 30-100°C was followed by a dwell, in which the relaxation of resistivity and Hall coefficient was stored. While Sample I exhibited increasing/decreasing resistivity after increasing/decreasing temperature step, an opposite behavior was identified at Sample II. Faster relaxation of Sample I allowed us to establish the activation energy of the process 0.3 eV. The relaxation effects were attributed to fast diffusing group I donors penetrating the material at the densities ~ $10^{13}cm^{-3}$ in Sample I and ~ 10^{14} cm^{-3} in Sample II.

3.2 Continuous temperature change

The sample temperature was controlled by a temperature controller, which enabled us to set a ramp rate of 1 K/min during the experiment. The accuracy of the temperature control was 0.1 K. An influence of different ambient atmosphere and the rate of thermal change on the results were studied as well. Both argon and vacuum gave the same relaxation characteristics (see Fig. 3.10). Likewise, diverse heating/cooling rates were also tested in order to find the best heating/cooling regime for the reproducibility of the measurements (see Fig. 3.11 and Fig. 3.12). The red lines in the figures indicate the heating of the sample in the beginning and the blue lines indicate the subsequent cooling.

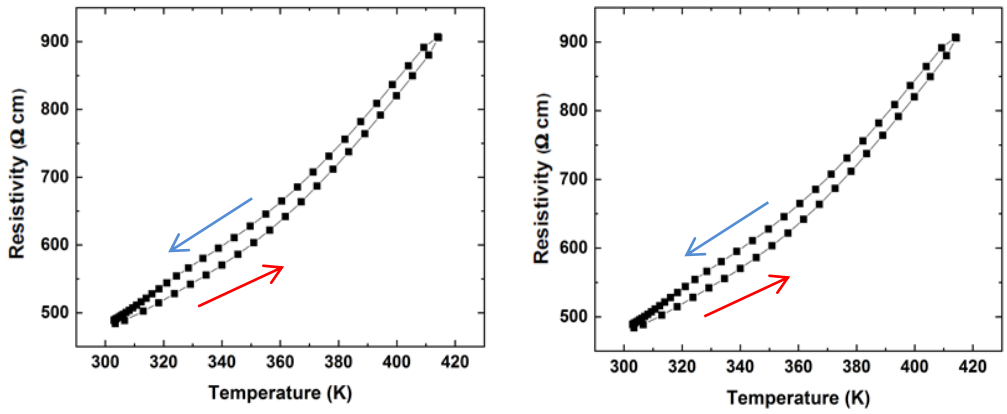

Fig. 3.10: The resistivity evolution 30-140-30°C with continuously changed temperature in vacuum (left) and argon (right).

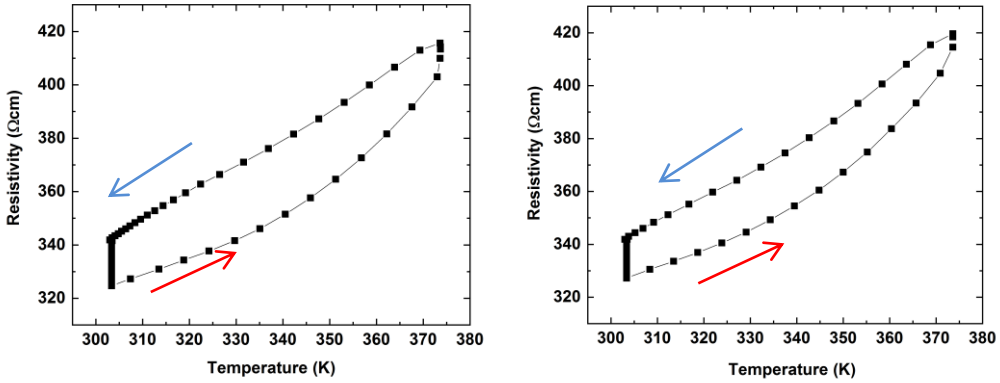

Fig. 3.11: The resistivity evolution 30-100-30°C with continuously changed temperature with a temperature rate of 1K/min (left) and 0.5K/min (right).

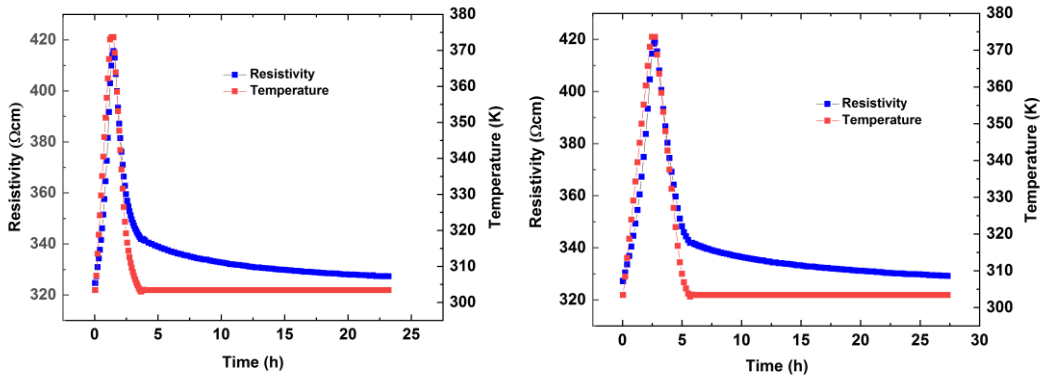

Fig. 3.12: The resistivity evolution 30-100-30°C with continuously changed temperature with a temperature rate of 1 K/min (left) and 0.5 K/min (right).

Moreover, the heating cycles were also repeated to test the effects of a heating cycle on the subsequent heating cycle (see Fig. 3.13).

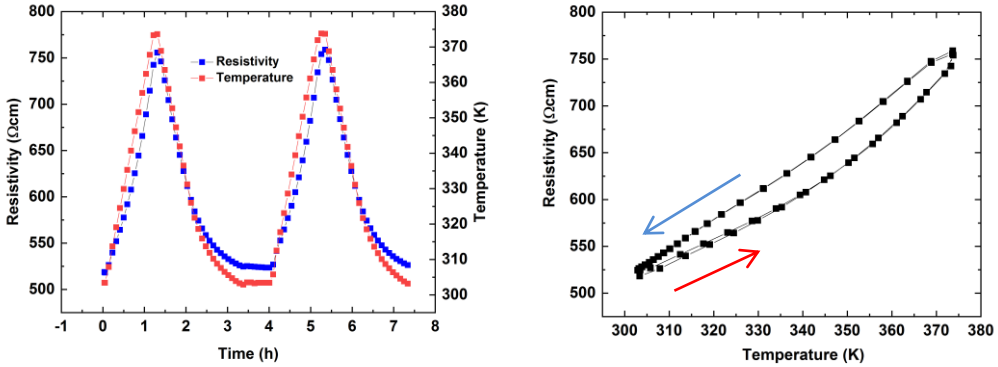

Fig. 3.13: The resistivity evolution 30-100-30-100-30°C with continuously changed temperature.

As it is visible from graphs 3.10 – 3.13, the ambient atmosphere and the temperature rate, 0.5 K/min vs. 1K/min, played no role in the measurements. The repetition of the measurements also gave the same results. The measurement of a single value of the Hall coefficient R_H in our setup took about 3 min, which is necessary for the magnetic field and electric current stabilization in all combinations in the classical Hall-bar method. The hole density p and Hall mobility μ_h evaluated in the dynamic regime then suffer from enlarged noise. To suppress the noise in the data employed

for ensuing theoretical analysis, and in view of the fact that measured μ_h follows well the theoretical formula [49]:

$$\mu_h^{PO} = 57\left(e^{252/T(K)} - 1\right)(cm^2V^{-1}s^{-1}), \tag{3.3}$$

the hole density p was elicited from the resistivity ρ via the obvious formula

$$p = \frac{1}{e\mu_h\rho}. \tag{3.4}$$

The Hall data were used for the verification of sample stability and the course of μ_h in the dynamic regime.

The chemical analysis of samples surface was performed by SIMS. The mass spectra were recorded using 5 keV Cs^+ primary ion beam.

Second-phase particles (SPPs) were watched by infrared microscopy. Tellurium inclusions were observed in usual densities and dimensions typical for CdTe grown from Te-rich melt [50]. The photo characterizing the distribution and magnitude of SPPs in measured sample is shown in Fig. 3.14.

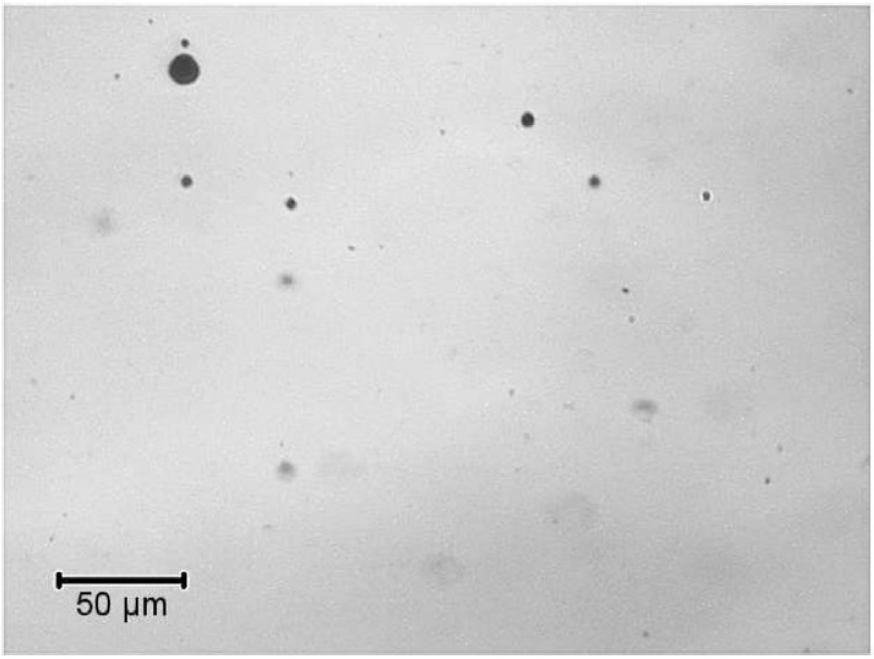

Fig. 3.14: IR image of measured CdTe sample with Te inclusions of variable magnitude.

The density of small SPPs with the radius $\delta < 1$ μm was estimated at 2×10^6 cm^3 and of those with the radius $\delta > 1$ μm at 5×10^4 cm^{-3}.

The experiments were performed in the dynamic regime with samples heated and cooled continuously at a constant heating/cooling rate of 1 K/min and a short delay of about 15 min at the maximum temperature. The reason for such unusual course was an effort to explore the behavior of p-CdTe in a wide temperature interval involving the regions where the irreversible process takes place. Characteristic profiles of temperature, ρ, p, and μ_h are plotted in Fig. 3.15. The slowing down of the cooling rate in the final part of cooling was due to the delay of the heat transfer given by the ambient room temperature.

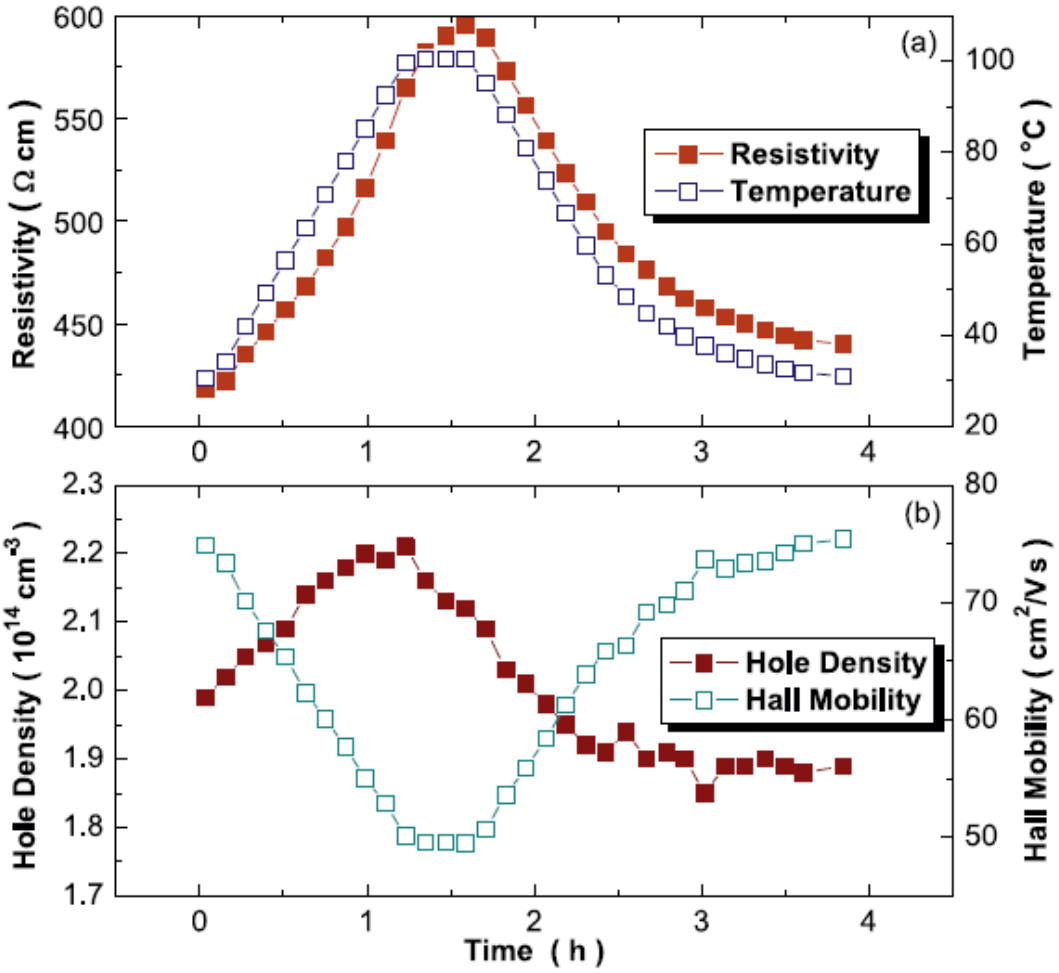

Fig. 3.15: Example of temporal evolution of electric properties induced by gradual change of temperature 30-100-30°C. Panel (a) shows the temperature and resistivity. Panel (b) shows the hole density and mobility.

In the following pages, in Fig. 3.16 - Fig. 3.20, the detailed measurement data of the continuous temperature changes are depicted for 100°C, 120°C, 140°C, 160°C and 180°C.

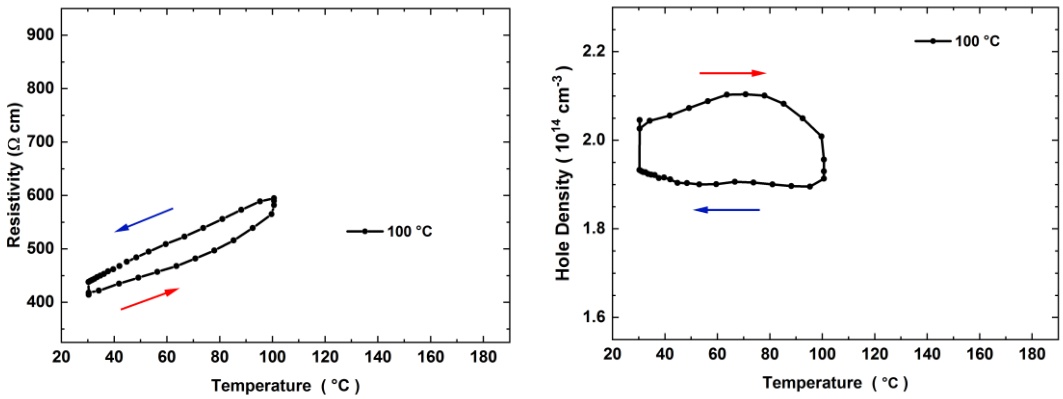

Fig. 3.16: The resistivity and hole density evolution for 30-100-30°C with continuously changed temperature.

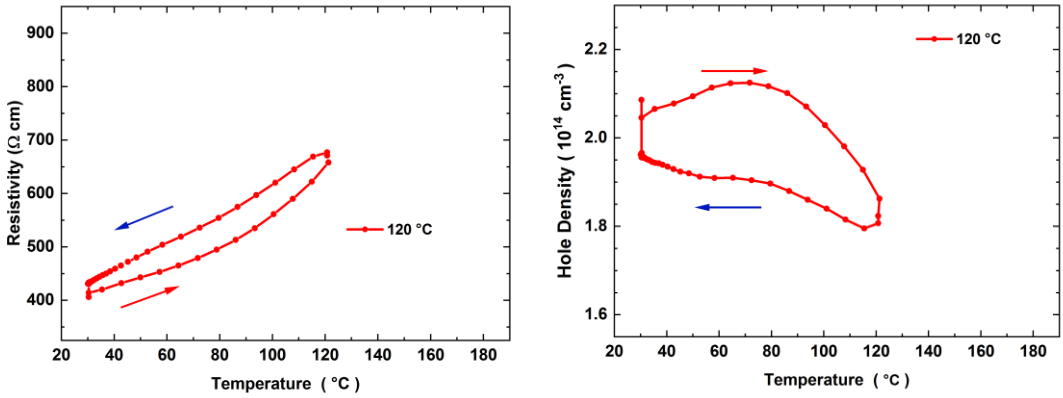

Fig. 3.17: The resistivity and hole density evolution for 30-120-30°C with continuously changed temperature.

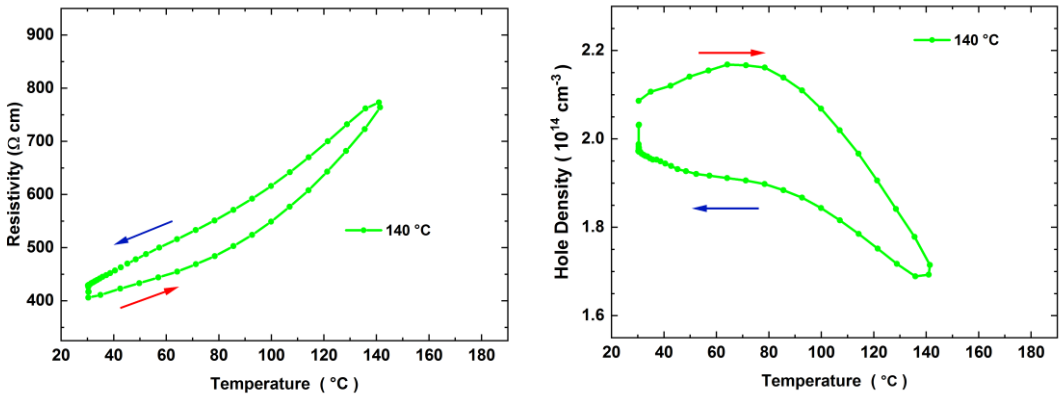

Fig. 3.18: The resistivity and hole density evolution for 30-140-30°C with continuously changed temperature.

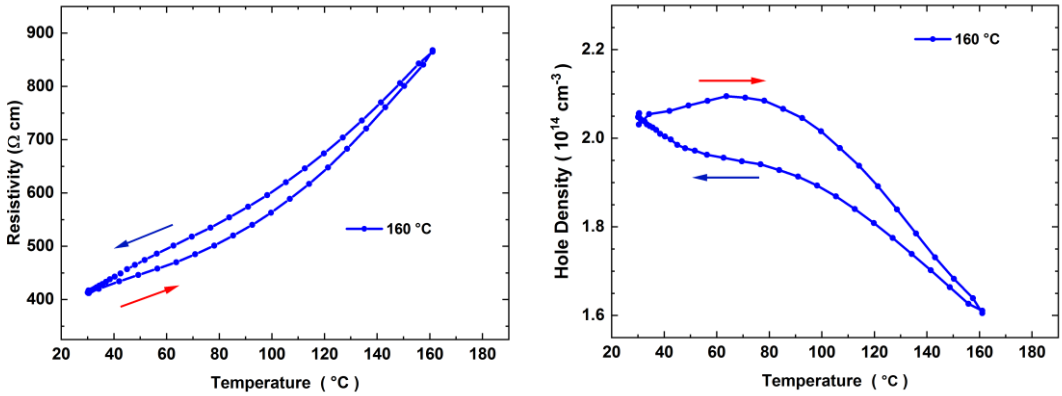

Fig. 3.19: The resistivity and hole density evolution for 30-160-30°C with continuously changed temperature.

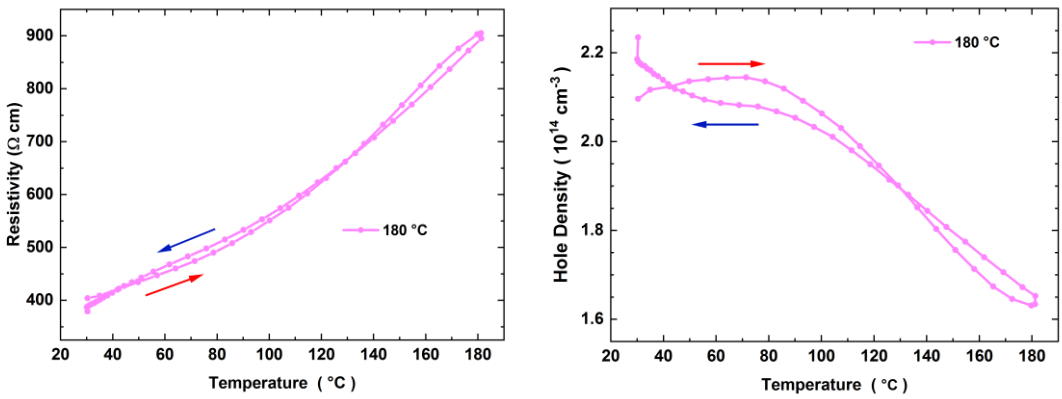

Fig. 3.20: The resistivity and hole density evolution for 30-180-30°C with continuously changed temperature.

The comprehensive overview of the measurement in the dynamic regime is plotted in Fig. 3.21. Here we may clearly see the most interesting discovery of the research. In contrast to the basic theory of semiconductors, which firmly predicts increasing/decreasing carrier density along with heating/cooling of the material, we observe an opposite behavior above ~100°C.

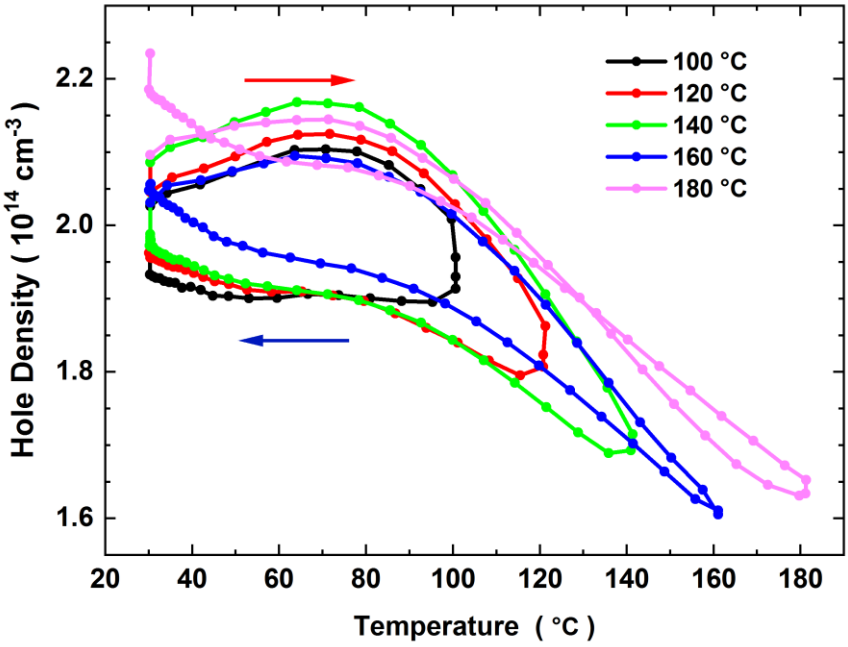

Fig. 3.21: Hole density vs temperature for the gradual increase and decrease of temperature. Five cycles were measured with the maximum temperature depicted in the legend.

3.2.1 Theory of the hole density evolution in the continuous heating cycles

The explanation of this effect is the main topic of the next section. The changes of electrical properties after heating up to 140°C could recover by a 1-day storage at 30°C. The heating above 140°C induced the appearance of another effect manifesting in the irreversible increase of p. The essential features of the experimental results could be reproduced on different samples.

The SIMS was measured on samples before and after the thermal treatment with the aim to identify diffusing atoms responsible for observed effects. All samples showed considerable enhancement of Na and K on the surface after the treatment. Normalizing to the signal of Te ions, the signal of Na and K has increased 3-10 times and 3-5 times after the treatment, respectively. In view of the fact that Na and K are known as fast diffusing group I elements in semiconductors, we propose these elements for the most probable species responsible for observed effects. Unfortunately, the extreme differences in sensitivity of the SIMS method for CdTe matrix material and Na and K impurities did not allow us to perform a sufficiently precise quantitative analysis and evaluation of the element density in the surface layer. The premise thus could not be supported by quantitative data. Other analytical techniques accessible in the laboratory are not sensitive enough to detect changes of element densities in the estimated range $<10^{15}$ cm^{-3}.

The reversible relaxation of ρ and p at steady temperature without distinct variations of μ_h points to the diffusion character of the discovered process. We have followed such a scheme and assumed that the thermal activation of the relaxation process is dominantly mediated by the diffusion coefficient attaining the form of the Arrhenius equation:

$$D = D_0 e^{-\frac{E_D}{k_b T}}, \tag{3.5}$$

with the pre-exponential factor D_0 and activation energy E_D. The time dependence of the conductivity $\sigma(t)$ than scales with D along with $\sigma(t) \equiv \tilde{\sigma}(Dt)$. The measurement of relaxation at different temperatures allowed us a direct determination of E_D by fitting experimental data using the trial double-exponential formula

$$\sigma(t) = \sigma_\infty + \sigma_1 e^{-\alpha_1 D(T) t} + \sigma_2 e^{-\alpha_2 D(T) t} \tag{3.6}$$

with the conductivity $\sigma = 1/\rho$ and parameters of the fit σ_1, α_1, σ_2, and α_2. This is analogous to our measurements depicted in Fig. 3.8. The evaluated slopes (relaxation rates $\alpha_{1,2}D(T)$) of $\sigma(t)$ at temperatures 30, 40, 50, and 80°C are in Fig. 3.22.

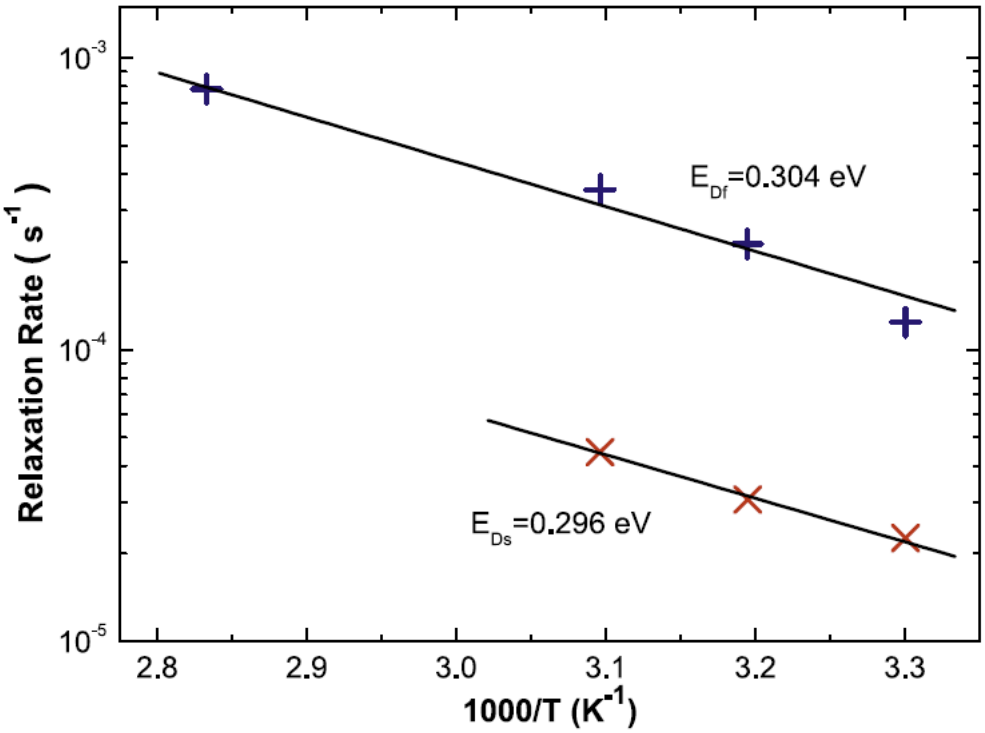

Fig. 3.22: Temperature dependence of the conductivity relaxation rates with the Arrhenius plot. E_{Ds} and E_{Df} depict the activation energy of the slow and fast relaxation, respectively.

The relaxation at 80°C was determined from the measurements shown in Fig. 3.1 for the second heating, and allowed us to establish only the faster component. The pre-exponential factor D_0 could not be determined in this experiment due to an unknown characteristic range of the diffusion process represented by parameters $\alpha_{1,2}$. The relatively narrow temperature interval of 30-80°C used to determine E_D was limited by an upper T, where the irreversible changes appear. Though a strong irreversible process was observed above 140°C, it was detected after long-term heating at T>80°C as well and such T could not be used for a reliable determination of the relaxation rate. Both relaxation components show a very similar slope of the Arrhenius plot providing the activation energy of the slow and fast processes E_{Ds} = 0.296 eV and E_{Df} = 0.304 eV, respectively. The mean energy E_D = 0.30 eV was estimated as the most characteristic value used hereafter in all simulations in the thesis.

In contrast to our previous analysis of relaxation effects in p-CdTe, we relinquish the concept of the diffusion of defects from/to the sample surface and assume that the diffusion occurs mostly inside the sample. The reason of this change is the complicated character of observed effects revealing a reversible character after moderate heating and cooling to room temperature and the fact that Na and K appeared in remarkable density on the sample surface after the thermal treatment. Consequently, we deduce that the surface is an important location for segregation of impurities, which may be hardly driven back to the crystal as must be anticipated in reversible processes. We thus conclude that the surface impurity segregation represents mostly a unidirectional process and does not describe principal reversible effects.

It is known that Te inclusions existing in Te-rich CdTe getter impurities in the large scale [51,52]. The cooling of as-grown crystal results in their enhanced concentration in inclusions and, conversely, the impurities spread in the crystal at the heating. Because the fast diffusing impurities migrate mostly interstitially [53,54], donor-type character may be supposed [29]. Migrating donors partly compensate dominant acceptors and subsequently reduce p in p-CdTe. Based on these premises we have developed the consecutive model explaining the effects plotted in Fig. 3.21.

Let us assume that the CdTe bulk contains SPPs with characteristic radius δ and density N_p randomly distributed in the crystal. The mean volume of the bulk belonging to single SPP extends in a sphere with radius R(>> δ) around SPP

$$R = \sqrt[3]{\frac{3}{4\pi N_p}}. \tag{3.7}$$

Both SPPs and bulk contain fast diffusing species (DS), which are neutral, if positioned in SPPs, and positively charged in the bulk. Shallow donors formed by extrinsic atoms located in interstitial positions are characteristic representatives. Homogeneous initial distribution of DS in the bulk with the density c_0 is assumed. The equilibrium density of DS in SPPs c_p is enhanced by the binding energy E_b

$$c_p = c_0 e^{\frac{E_b}{k_b T}} \tag{3.8}$$

where k_b is the Boltzmann constant. Equal density of interstitial sites in CdTe and in SPPs is assumed for simplicity. Homogeneous distribution of DS in the bulk c_0 and c_p defined by eq. (3.8) warrants the system in thermodynamic equilibrium at the start.

Heating of the system results in the release of DS from SPPs and their dispersion in the ambient spherically-shaped bulk. The process may be described as diffusion from spherical source by the equation

$$\frac{\partial c}{\partial t} = \frac{D}{r^2}\frac{\partial}{\partial \mathrm{r}}\left(r^2 \frac{\partial \mathrm{c}}{\partial \mathrm{r}}\right) \tag{3.9}$$

solved in the interval $\delta < r < R$. The boundary condition at the SPP-bulk interface is derived by differentiating of generalized eq. (3.8)

$$c_p(t) = c(\delta, t) e^{\frac{E_b}{k_b T(t)}} \tag{3.10}$$

with respect to time, considering the particle conservation and assuming homogeneous distribution of DS within SPP and local thermal equilibrium as

$$\left.\frac{\partial c}{\partial t}\right|_{r=\delta} = c(\delta)\frac{E_B}{k_b T^2}\frac{\partial T}{\partial t} + \frac{3D}{\delta e^{\frac{E_b}{k_b T}}}\frac{\partial c}{\partial r}. \tag{3.11}$$

The boundary condition at the outer diameter R is calculated as

$$\left.\frac{\partial c}{\partial t}\right|_{r=R} = D\left.\frac{\partial^2 c}{\partial r^2}\right|_{r=R} \tag{3.12}$$

considering particle conservation within the spherical region $dc/dr = 0$ at $r = R$.

The diffusion equation (3.9) with defined boundary conditions (3.11), (3.12) is time-integrated numerically with Adaptive Step-size Control of the fourth-order Runge-Kutta method [55]. Integrating $c(r,t)$ may be applied for the calculation of total amount of charged DS in the bulk. The calculation may be also done more effectively, when the conservation of DS and the local equilibrium between SPP and adjacent bulk are considered. The mean DS density in the bulk may than be calculated as

$$\bar{c} = c_0 + \frac{\delta^3}{R^3}\left(c_0 e^{\frac{E_b}{k_b T_0}} - c(\delta, t) e^{\frac{E_b}{k_b T}}\right) \tag{3.13}$$

where T_0 is the initial temperature.

The outlined model was successfully applied in the fit of $p(t)$ in the sample subjected to the thermal changes shown in Fig. 3.21 by the formula

$$p = N_{a1} + \frac{N_{a2}}{1 + 4e^{\frac{E_{a2} - E_F}{k_b T_0}}} - \bar{c}\,. \tag{3.14}$$

In addition to the DS treated as shallow donors, two acceptor levels were included into the defect model to assure the p-type character of the material. The first level with the density N_{a1} is a shallow level totally ionized in the range of temperatures used. The second level is characterized by the density N_{a2} and ionization energy E_{a2}. It assures the slight increase of p in the initial heating up to ~ 80°C. The Fermi energy E_F could be deduced from the experimental p in the temperature interval 303 K - 453 K and a linear form

$$E_F(meV) = -64 + 1.2T\ . \tag{3.15}$$

appeared quite satisfactory to describe its course. Fermi energy is defined relatively to the valence band maximum here.

The simulation of p is shown by dashed lines in Fig. 3.23. The model parameters are: N_p = 4.5 ×10^5 cm^3, δ = 2 μm, E_b= 0.37 eV, c_0 = 3.6 × 10^{12} cm^3, D_0 = 4 × 10^{-3} cm^2 s^{-1}, E_D = 0.3 eV, N_{a1} = 1.9 × 10^{14} cm^{-3}, N_{a2} = 3.2 × 10^{13} cm^{-3} and E_{a2} = 0.25 eV. None of the parameters falls out of the range of values routinely observed or presumed in p-CdTe with Te inclusions. We give also other relevant quantities characterizing the model: the sphere radius R = 81 μm, diffusion length at 140°C and characteristic time 1 min L = 72μm, equilibrium density of DS at 140°C c_0(140°C) = 5.8 × 10^{13} cm^{-3}, and the total density of DS in the bulk and in SPPs c_{tot} = 8.9 × 10^{13} cm^{-3}.

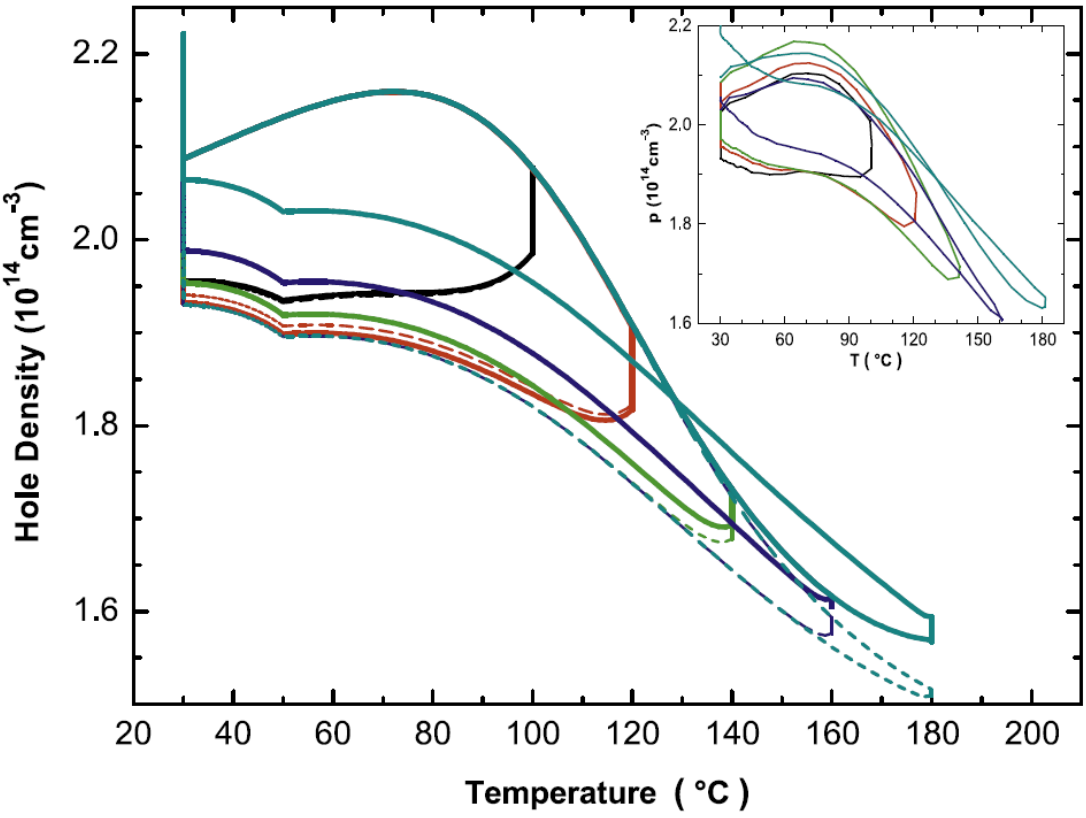

Fig. 3.23: Fit of the hole density vs temperature plotted in Fig. 3.21. Full lines show the complete fit including the irreversible source of acceptors. Dashed lines show the results without the irreversible processes. The inset displays the fitted experiment.

The appearance of an irreversible mechanism leading to the increase of p at the heating above 140°C and manifested by the loop at the measurement to 180°C was not involved in the model. We assume that this effect is caused by an activation of a source of acceptors at increased temperature in the sample. We thus attached an appropriate thermally activated process into the model via the form

$$\frac{\partial \tilde{p}}{\partial t} = \alpha e^{-\frac{E_a}{k_b T}} \tag{3.16}$$

where $\alpha = 6 \times 10^{16}$ cm^{-3} s^{-1} and $E_a = 0.65$ eV. The initial condition $\tilde{\boldsymbol{p}} = 0$ was used. On integrating eq. (3.16) numerically along the $T(t)$, calculated $\tilde{\boldsymbol{p}}$ was added to previously obtained p. Final curves are shown as full lines in Fig. 3.23. Due to the

irreversible character of the process, its detailed exploration was not possible in this experimental scheme.

For the sake of lucidity, the simulation of each loop starts from the same initial conditions so that the heating period follows always the same curve. In case of real experiment, the measurement of the loop above 140°C induced the irreversible change of the sample and subsequent loops followed unlike paths. The curve depicting cooling phase of the loop up to 100°C passes at slightly higher p compared to the experiment. This deviation is caused by a longer delay (25 min) at the maximum temperature than it was in other loops (~15 min), and leads to correspondingly enhanced appearance of DS.

It should be pointed out that a fit of similar quality could be obtained with a different choice of parameters so that given parameters do not represent a unique possibility to fit the experimental data properly. The aim of the above simulations was the qualitative demonstration of the validity of the model depicting the observed effects. The qualitative description of the data would require a more detailed determination of the properties of SPPs involving the generalization of the model to randomly distributed SPPs with variable magnitude.

In contrast to the double-exponential relaxation of $\sigma(t)$ measured at constant temperature as shown in Fig. 3.8, analogous simulations using the presented model followed steadily the single-exponential rule. One should thus cogitate on the reason of the discrepancy. The similarity of $E_{Ds} \approx E_{Df}$ indicates that the slow and fast relaxations are mediated by the same DS. We thus deduce that the different rates are induced by variable density and radii of SPPs as seen in Fig. 3.14 and consecutively by different characteristic relaxation rates within the crystal. The double-exponential relaxation points to two distinguished regions in the bulk with specific SPP properties.

3.2.2 Summary of continuous temperature changes

In this section we described the conductivity and Hall-effect measurements in p-type CdTe subjected to thermal changes in the range of 30-180°C.We have shown that thermal changes often lead to anomalous behavior of the hole density characterized

by reversible decrease/increase at the heating/cooling regime. The anomaly was explained by the transfer of fast diffusing donors between Te inclusions and ambient bulk. Sodium and potassium were proposed as the most probable diffusing species by the SIMS. Theoretical model based on this premise was built up and successfully applied to experimental data.

3.3 Oxidation and erosion of CdTe surface in distilled water and NaCl solution

3.3.1 Oxidation and erosion of CdTe surface in distilled water

In the field of room-temperature X-ray and gamma-ray detectors, CdTe and CdZnTe, are long-term considered as promising semiconductor materials. The performance of these detectors is principally influenced by the quality of surface treatment, particularly by mechanical polishing and subsequent chemical etching in a bromine-methanol solution [56]. Besides, in the case of chemical Au contact preparation commonly used for this semiconductor [57] the detector material is immersed into distilled water solution of $AuCl_3$. Upon contact preparation, the surface of the detector is commonly exposed to distilled water, which can lead also to oxidization of the detector surface [58]. Studies have shown that the oxidization contributes to the leakage current by changing the conducting properties of the detector [59]. The leakage current consequently affects many aspects of the device operation and performance. Several ellipsometric studies have been carried out [60,61,62,63] to evaluate the surface layer thickness with respect to the surface preparation techniques and history. The oxygen bound merely to Te was determined by XPS measurements after long-term storage of the sample in air [61].

The oxidation of semiconductor's surface exposed to air or immersed in a liquid constitutes an important process significantly influencing the surface properties of specimens as well as the quality of electronic devices. Models describing oxidation of silicon mostly rely on the Deal-Grove theory [64,65,66] defining the velocity of oxidation by the diffusion of oxygen through the oxide layer. Wet oxidation of AlGaAs at elevated temperature showed constant oxidation rate in the range of oxide

later thickness 10-250 nm [67]. Concurrently with the corrosion of metals, which represents basically analogous phenomenon, the oxidation of solids was extensively investigated for decades [68,69]. To the best of our knowledge, the study of a surface oxide layer formation and its thickness evolution with respect to the time of its immersion in distilled water has not been reported in CdTe and CdZnTe yet. The knowledge of these dynamics may help to better understand the process of surface oxide formation and surface degradation, which plays a key role in the production of high quality and stable detectors.

The unintentional contamination of semiconductors constantly bothers researchers at any treatment with the high purity material. Fast diffusing species mainly issuing from group one elements in the periodic table are the most critical pollutants since they could contaminate not only the thin surface layer but they may penetrate deep in the bulk of the material and depreciate this way its demanded properties. In our opinion, sodium represents one of the most dangerous elements in this group due to its abundance in the ambient. The diffusion of sodium was suggested as the most probable mechanism responsible for fast changes of electrical properties of p-CdTe subject to moderate thermal changes [70]. Despite the practical importance, the penetration of Na into CdTe remained unattached by researchers so far. High temperature diffusion of Na was studied in [71].

In this chapter we investigated the effect of the immersion of CdTe in distilled water and in NaCl solution on the degradation of its surface. The purpose of the research was the completion of data measured on samples stored on air by analogous research using treatment in liquids. The samples were stored at fixed temperature 50^0C for 1-400 h either in distilled water or in NaCl solution. Grown surface oxides and surface degradation were studied by ellipsometry and by SIMS. It was proved that the oxidization proceeds much faster in water than in the air reaching 10 nm of surface oxide after 400h immersion. The investigation of Na diffusion revealed, up to 500nm thick affected layer found by SIMS in the sample long-term stored in NaCl solution.

CdTe crystals were grown just as for the previous experiments, by the Vertical-gradient freezing method. Single-crystalline samples, cut from the CdTe ingot, were high-quality intentionally undoped p-type crystals with the hole mobility close to 75 $cm^2V^{-1}s^{-1}$ at 300 K. The samples in our investigation were square shaped with the resistivity in the range of 200 to 400 Ωcm and typical dimensions of 5x5x2 mm^3.

The samples were polished and etched to remove a damaged layer from the surface induced by cutting. Prior to each set of experiments the top surface was chemo-mechanically polished for 30 s on a silk pad using a 3% Br-ethylene glycol solution. Afterwards, the sample was immersed into 3% Br_2-methanol solution for the same time keeping the top surface oriented upwards. To observe and describe the evolution of the surface oxide layer the sample was immersed into a reservoir with distilled water heated at 50°C for 1h-400h time extent. A combination of spectroscopic ellipsometry, XPS and SIMS were employed to systematically study the evolution of surface oxide and CdTe near surface.

Although spectrally dependent optical properties of bulk CdTe can be found elsewhere [62,72,73], they might slightly differ with respect to the growth method and stoichiometry of the sample. Therefore, the spectral dependence of optical properties of studied CdTe samples was deduced prior to the distilled water immersions. Since the measurements have been done right after the surface preparation (within 2 minutes) we did not consider the surface oxide layer in the model structure. A set of Tauc-Lorentz oscillators was used to parametrize the spectral dependence of CdTe optical properties. Resulting spectra of the optical parameters of the etched CdTe are plotted in Fig. 3.24 and they follow the dependencies already published in the literature [61].

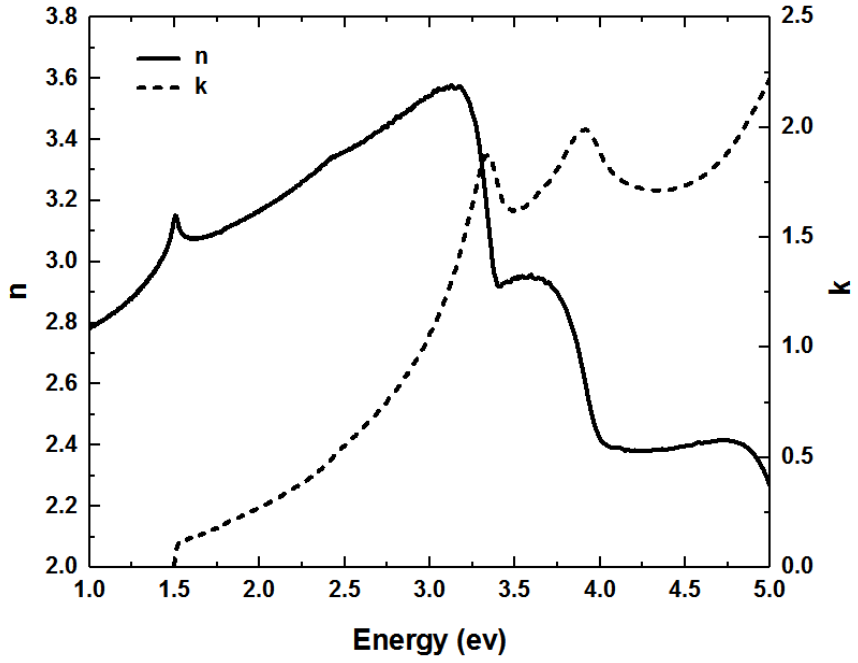

Fig. 3.24: Optical parameters of bulk CdTe determined from ellipsometry.

Knowing the optical parameters of bulk CdTe, the sample was immersed into distilled water for certain period. Afterwards, the sample was taken out, dried by pressurized air and immediately measured by ellipsometry. Experimental spectra of ellipsometric parameters Psi and Delta for an etched and 48h immersed sample are shown in Fig. 3.25.

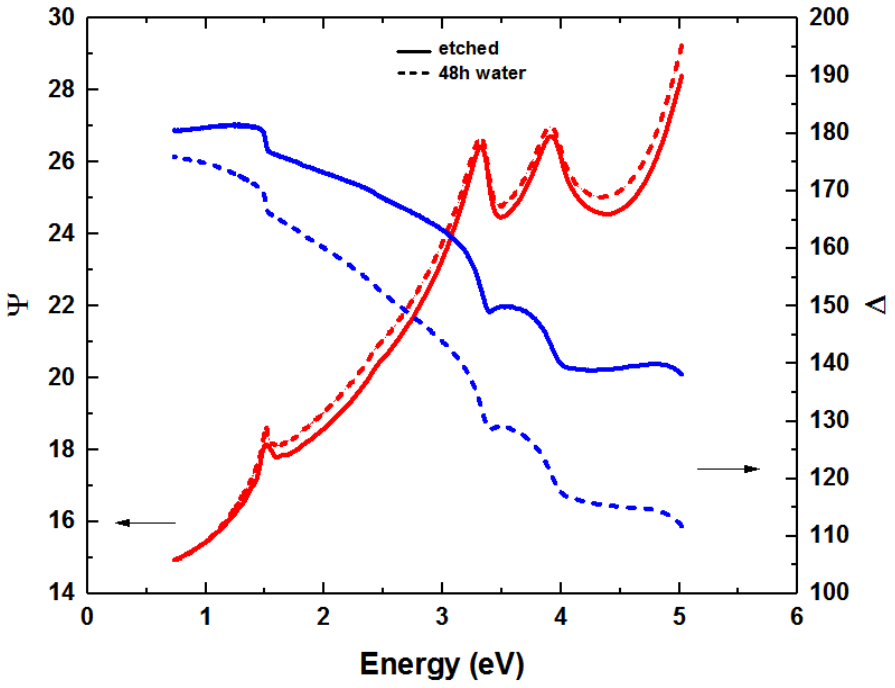

Fig. 3.25: Experimental spectra of ellipsometric parameters Psi and Delta for etched and 48h treated sample in distilled water.

From this figure one can see that the immersion resulted in different optical response of the sample. A set of experimental data for immersion times varying from 45 min to 96 h was obtained and fitted at once using the model structure of a single surface oxide layer with roughness on bulk CdTe. Optical parameters of CdTe were taken from the measurements on bare CdTe right after the surface preparation and the parameters of the surface oxide were taken from the literature [61] (parametrized by Cauchy relation). Only the surface roughness and surface oxide thickness were the parameters allowed to fit, since we considered that the optical properties of CdTe and surface oxide do not change during the oxidation. An example of the fit of experimental data for the immersion time of 48 hours is shown in Fig. 3.26.

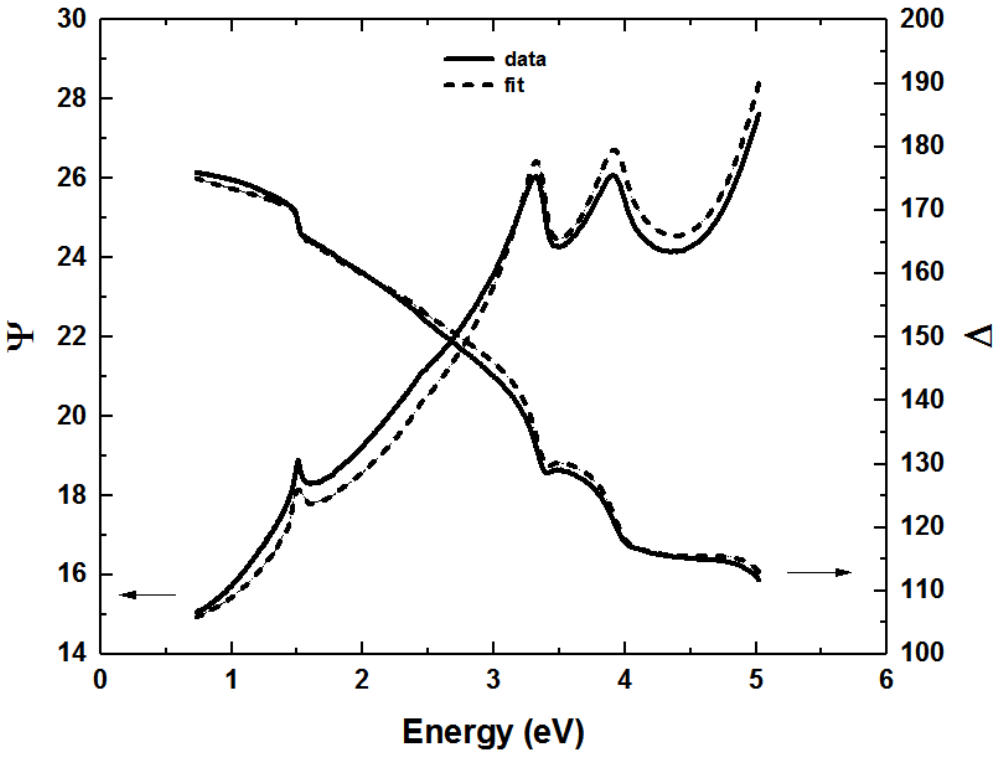

Fig. 3.26: Theoretical fit for 48h surface treated sample in distilled water.

The fit is in a reasonable agreement with experimental data and the deviations may have origin in slightly different optical properties of Te oxide on the surface. Another explanation of deviations can be the loss of ideal planar surface due to lengthy water exposure, since the oxide formation is a complex process.

As it is apparent in Fig. 3.25, the 48-hour treatment shifted both ellipsometric angles Ψ and Δ (red and blue lines respectively). The changes are more pronounced in Δ spectrum, which is related to the change of the phase of light upon the reflection, and suggest certain changes at the surface. With the aforementioned model structure, the spectrum could be fitted, as it is shown in Fig. 3.26. It should be mentioned that the distinct water treatment periods were chosen in a random time interval series to avoid the pertinent effect of systematic degradation of the sample surface. The sequence of periods was alternated between short and long-time intervals.

The thickness and roughness of the oxide layer evaluated by the above defined procedures are shown in Fig. 3.27.

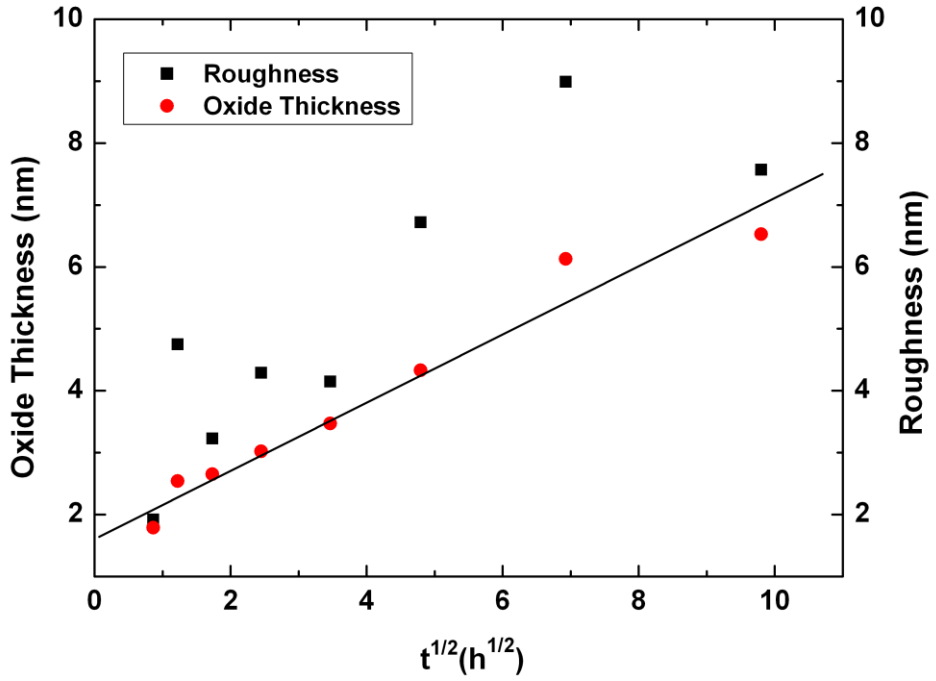

Fig. 3.27: Evaluated thickness and roughness for different time intervals for the distilled water treated sample.

Despite of slightly scattered data it is clearly seen that the growth of the oxide layer may be conveniently expressed by a linear function of the square root of time. The fit of the oxide thickness yields

$$l(mm) = 1.7 + 0.54\sqrt{t(h)}. \qquad (3.17)$$

A qualitative model describing the oxide layer formation is presented also in the next section.

The chemical composition of the surface layer was evaluated from XPS measurements. The XPS spectra were first measured on the as-received etched surface and then after 96 hours distilled-water surface treatment. Fig. 3.28 shows examples of Te3d XPS spectra.

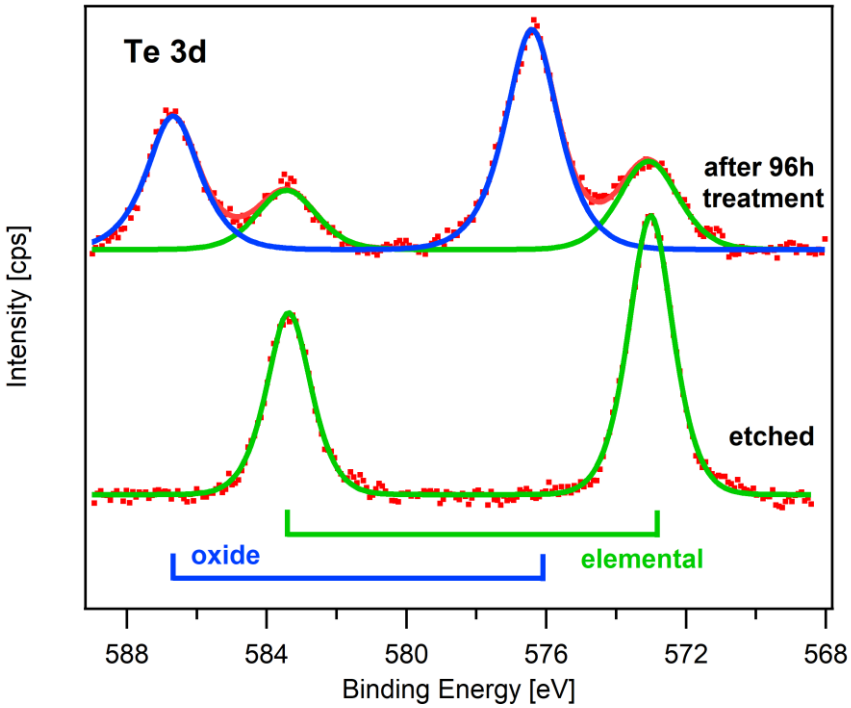

Fig. 3.28: Example of Te3d (a) and Cd3d (b) photoelectron spectra taken on etched surface and after 96 hours distilled-water surface treatment of CdTe sample.

Te3d spectrum is composed of oxide (doublet at binding energy (BE) of 576.1 eV and spin-orbital splitting Δ=10.4 eV) and elemental (doublet at BE 572.5 eV and Δ=10.4 eV) components, as indicated in the figure 3.21. It was found that both of these surfaces are enriched with Te. While the value of the Te/Cd atomic ratio on the etched surface was below 1.3, the value of this atomic ratio on the treated surface was substantially higher (1.85). After the etching of the surface, the XPS spectrum lacked the doublet for an oxide bound to tellurium and contained only the peaks for elemental tellurium. The absence of the surface oxide layer after the etching corresponds with our expectation and with other measurements [61]. After the surface treatment of the sample in distilled water, the oxide doublet was clearly visible. The value of the Te oxide/Te elemental atomic ratio on treated surface was 2.3. According to Bahl et al. [74], the position of the XPS peaks confirms the formation of a TeO_2 layer.

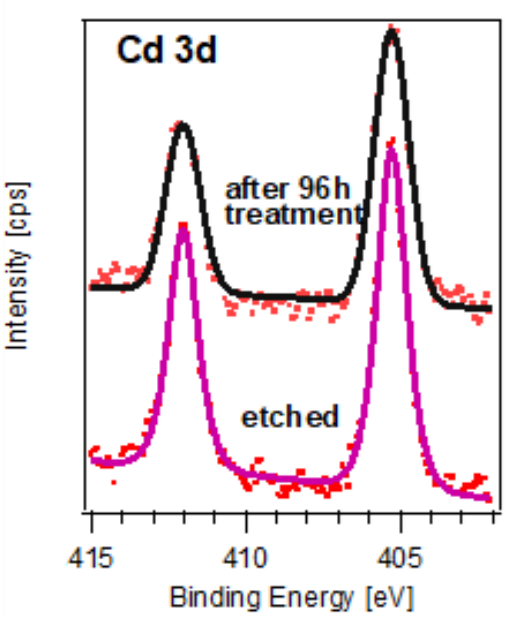

Fig. 3.29: Example of Cd3d photoelectron spectra taken on etched surface and after 96 hours distilled-water surface treatment of CdTe sample.

Passivation and oxide formation were discussed in the literature [75], where it was found that the surface composition depends strongly on the treatment procedure. Cd 3d photoelectron spectrum in the Fig. 3.29 composed of a doublet located at BE 405.3 eV and having spin-orbital splitting Δ=6.8 eV. We attributed this doublet to CdTe base material. The published BE values of Cd $3d_{5/2}$ emission line are 404.9 eV for thermal oxide and those in CdO, CdTe and $CdTeO_3$ are 403.0, 405.1 and 405.7 eV, respectively. Thus, the presence of phase should be indicated by a new or shoulder of the main CdTe peaks in the spectrum. In our case we did not observed any traces of additional component. Detail analysis of XP spectra showed only very slight broadening of the photoemission peak profile after treatment in distilled water. It can be attributed to the CdTe-oxide interface. It is also consistent with our previously published results in [61], [76] and [77].

In this section we propose a qualitative model conveniently explaining all experimental findings. Consistent theory of the oxidation of CdTe and CdZnTe should satisfactorily comprise the following demands:

1. As discovered by ellipsometry, the thickness of the oxide layer should be defined by the square root of time according to equation (3.17).
2. At the start of oxidation a layer with thickness about 1.7 nm is created very fast.

3. The oxide layer is dominantly formed by oxides of tellurium revealed by XPS.
4. The Te/Cd atomic ratio increases during the treatment. Consequently, cadmium should disappear from the surface layer in the process.

Two mechanisms are defining the oxidation of material surface widely studied in the literature being distinguished by a driving force forwarding the process. A diffusion model assuming the diffusion of oxygen through oxide layer was proposed at the explanation of silicon [64] and copper oxidation [69]. In metals, the theory mostly stems from diffusion and drift of ions from the metal through the oxide to the oxide-gas interface where they react to the oxide [66], [68]. We shall combine both mechanisms here. The principle of the model is schematically outlined in Fig. 3.30.

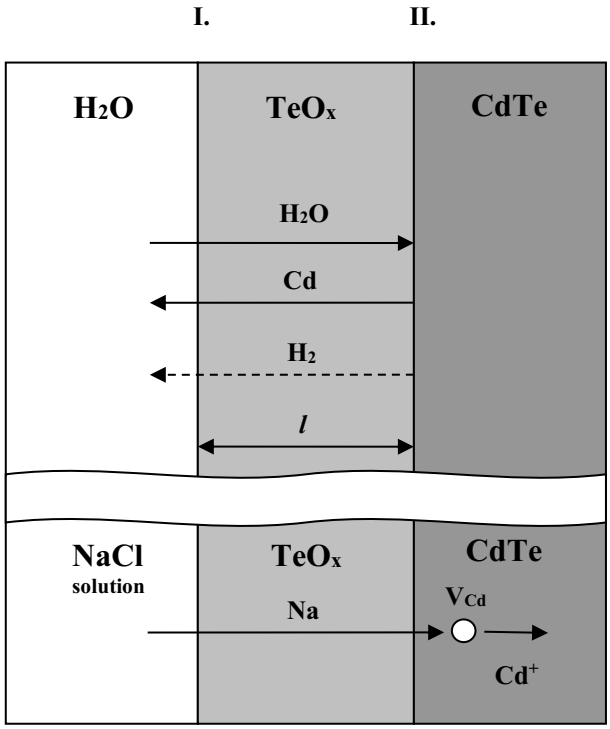

Fig. 3.30: A schematic layer configuration and processes on the surface of CdTe treated in water and in saturated NaCl solution. On the surface of CdTe a TeO_x oxide layer is disposed, denoted by interface II. The interface between the water or NaCl solution and TeO_x is denoted by I. Water molecules diffuse through the oxide with thickness *l* to CdTe and Cd cations drift from CdTe to water. Excess H_2 diffuses to water as well. In case of CdTe immersed in NaCl solution Na diffuses through the TeO_x to CdTe where it drifts interstitially as Na^+ ion and it is trapped in Cd sublattice liberating Cd cations.

The oxidation is driven by the reaction of water oxygen via chemical reaction

$$CdTe + xH_2O -> TeO_x + xH_2 + Cd\ . \tag{3.18}$$

Alternatively, the OH^- ions could enter into the reaction as well and single atomic hydrogen H^+ could appear instead of H_2. Water molecules diffuse through the oxide layer and degrade CdTe liberating Cd^+ ions. Cd^+ ions drift to the liquid forwarded by electric field oriented outward from CdTe to the water. The potential difference between water and CdTe is induced by excess of Cd^+ at the oxide-CdTe interface and also by contact potential difference. As it was observed in multiple metals [68], the initial stage of oxidation may occur much faster than the rest of the process. This phenomenon is probably caused by softer oxide structure localized few atomic layers adjacent to the liquid. The velocity of the oxidation is limited by the transport of species across the oxide layer. Oxygen is transported from water to CdTe and Cd moves in the opposite direction. Hereafter we shall assume that Cd^+ ions are less mobile than water molecules and the supply of H_2O to the oxide-CdTe interface is fast. Consequently, the rate of the drift of Cd^+ is the most critical kinetic quantity limiting the process.

The flux of Cd^+ across the oxide layer J is given by

$$J = E\mu[Cd^+] \tag{3.19}$$

where μ is the Cd ions mobility and E is the electric field distributed in the oxide defined by the electric potential difference on the oxide interfaces $E=-\delta\varphi/l$. $[Cd^+]$ denotes the Cd^+ density. Let us note that E and J are negative according the scheme in Fig. 3.30.

The soft oxide formed at the start of process allows much faster drift of Cd^+ than it occurs in thicker oxide when the oxide structure becomes stiff. With aim to fit eq. (3.17) we express the dependence of μ on oxide thickness l by a trial function

$$\mu(l) = \frac{\mu_0 l}{l - l_0} \tag{3.20}$$

which expresses the stabilization of μ in thick oxide layer in a final mobility μ_0 in thick oxide and l_0 characterizes the thickness of the soft oxide. For $l<l_0$ the mobility $\mu(l)$ is very large and it is approximated by infinity in this model. The rate of the growth of oxide layer is described by the equation

$$\frac{dl}{dt} = -\frac{J}{n_0} \tag{3.21}$$

where n_0 is the density of Te atoms in the oxide. Putting equations (3.19-3.21) together, we may compose the differential equation

$$\frac{dl}{dt} = \frac{\partial\varphi\mu_0[Cd^+]}{n_0(l-l_0)} \tag{3.22}$$

which may be easily integrated, giving the solution

$$l = l_0 + \sqrt{\frac{2\partial\varphi\mu_0}{n_0}[Cd^+]t}\,. \tag{3.23}$$

Final form (3.23) is equal to the fit of the experiment (3.17). Comparing eqs. (3.17) and (3.23), we may deduce for model parameters

$$\frac{2\partial\varphi\mu_0}{n_0}[Cd^+] = (0.54\times10^{-7})^2/3600 = 8.1\times10^{-19}(cm^2s^{-1}). \tag{3.24}$$

Taking characteristic n_0 for the tetragonal TeO_2 $n_0 = 2.3\times10^{22}$ cm^{-3}, we obtain $\delta\varphi\ \mu_0$ [Cd$^+$] = 9.3×10^3 cm^{-1}s^{-1}. Since we do not possess a technique for determination of $\delta\varphi$, μ_0 or [Cd$^+$] the model remains on a qualitative level in this respect.

Let us note that suggested model accords with the Cabrera-Mott limit of the high-field approximation [68] stating that the minimum oxide thickness, which could effectively screen the contact potential, should exceed 10 nm. In our case the oxide thickness does not reach such a value and the drift model is supported by this way.

Nevertheless, another model based on Cd$^+$ drift weakly different from the premises above could be created as well. This alternative model might start from an

assumption that negative charge inducing the electric field in the oxide is not localized on the water-oxide interface but it penetrates the soft oxide and localizes at the depth l_0 below the oxide surface. Such premise allows us to derive eq. (3.17) without the assumption of l-dependent μ. While the former model foresees the variable $\mu(l)$ depending on l but independent of the position, the latter model steadily splits the oxide layer in the soft layer with the thickness l_0 and stiff layer in the rest thickness l-l_0. Existing data do not allow us to give preference to one of the models.

3.3.2 Atomic force microscopy of the treated samples

In order to compare and characterize the treated samples in distilled water and in saturated NaCl solution the surface of the samples were scanned by a Bruker EDGE Atomic Force Microscope (AFM) with a closed-loop scanner. The silicon probe NCHV-A (see below on Fig. 3.31) was operated in tapping mode with a resonant frequency of 300 kHz.

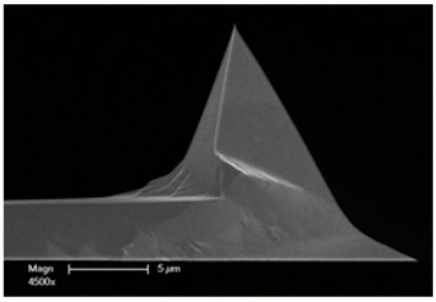

Tip Schematic

Geometry:	Standard (Steep)
Tip Height (h):	10 - 15µm
Front Angle (FA):	25 ± 2.5°
Back Angle (BA):	15 ± 2.5 °
Side Angle (SA):	22.5 ± 2.5 °
Tip Radius (Nom):	8 nm
Tip Radius (Max):	10 nm
Tip SetBack (TSB)(Nom):	12.5 µm
Tip Set Back (TSB)(RNG):	9 - 16 µm

Fig. 3.31: NCHV-A tip specification for the AFM microscope.

On the below Fig. 3.32 the surfaces of the etched sample and the water treated sample for 45 min are shown. For the proper orientation the surface was marked with a V sign which is visible in the lower part of the images.

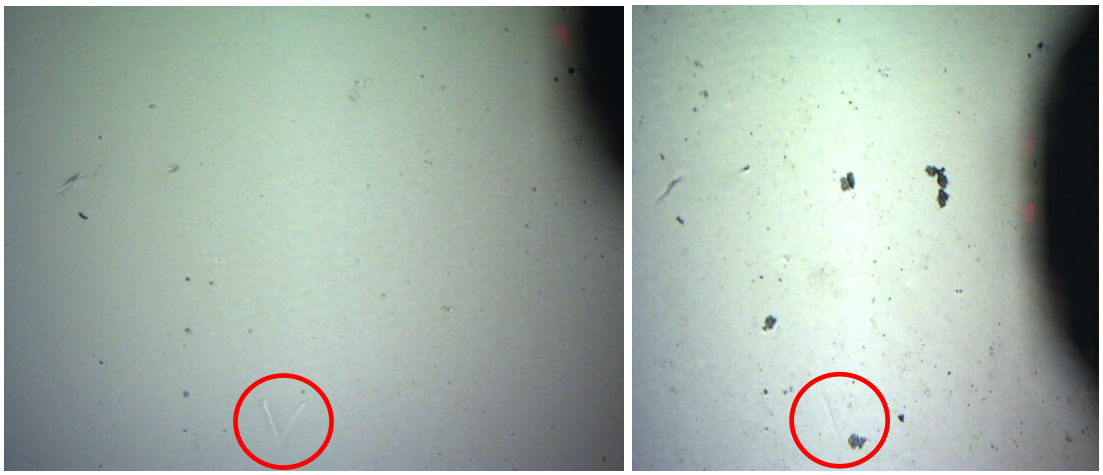

Fig. 3.32: Optical image of the etched surface and the water treated surface (45 min) of the sample.

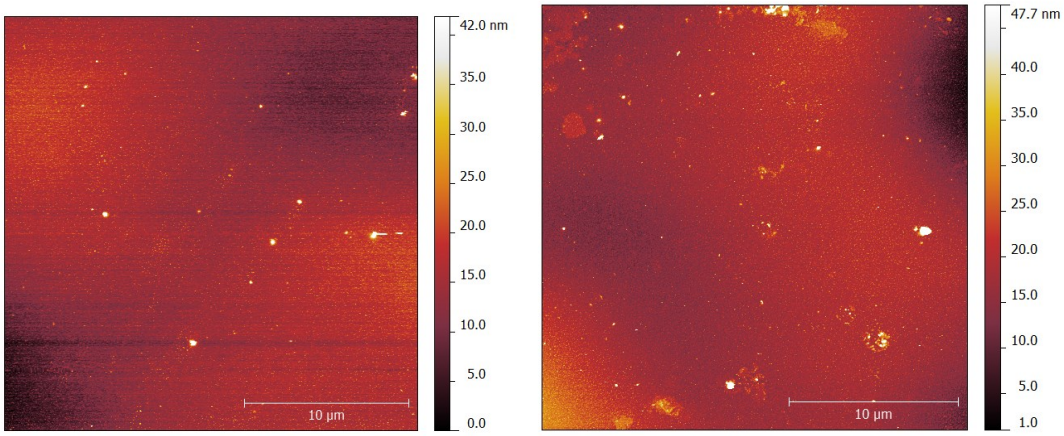

Fig. 3.33: Scan of the etched surface (left) and the water treated surface (45 min) with AFM (right).

On the above Fig. 3.33 two AFM scans are depicted for the etched surface and for the water treated surface (45 min) As it is visible from the above scans, the water treated sample has higher roughness compared to the etched surface and there are also small stains with a diameter of 2-5 μm. Thus, the water treated sample was contaminated and also had relatively big impurities on the surface which made it difficult to scan with AFM.

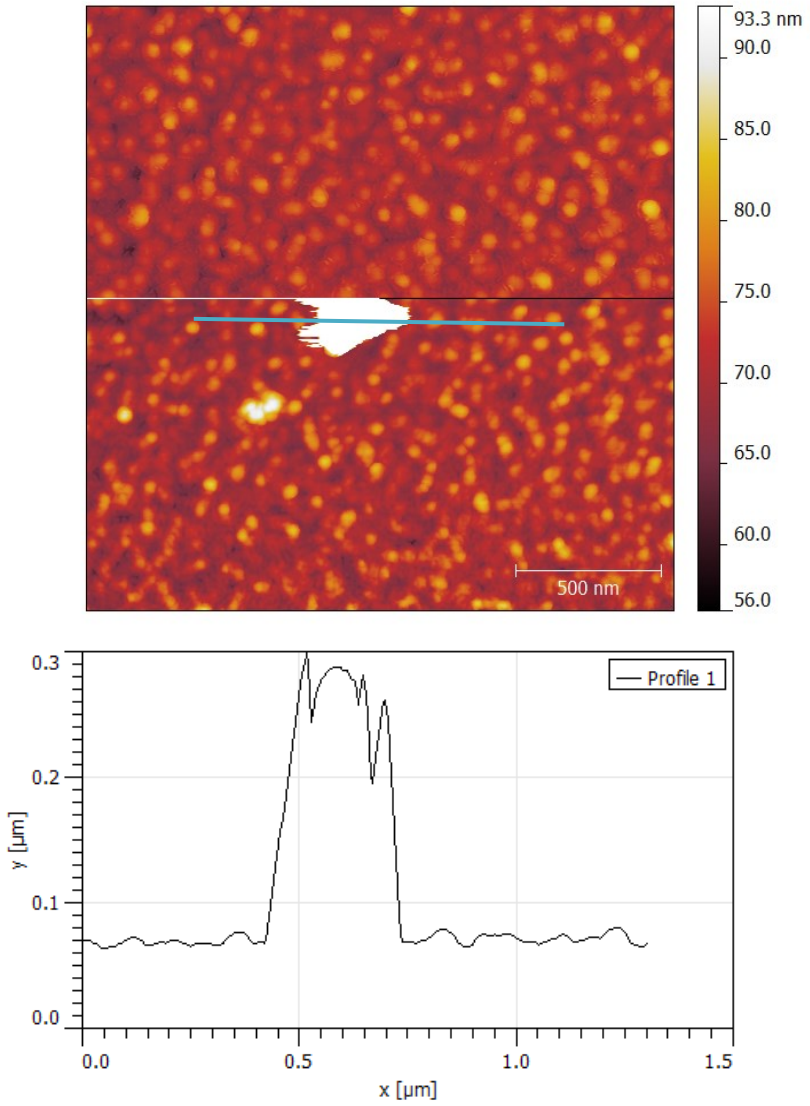

Fig. 3.34: Scan of the water treated surface (45 min) and a profile height measurement corresponding to the blue horizontal line on the upper image.

The scanning of the water treated surface, as shown on Fig. 3.34, was uneasy due to the relatively high impurities on the surface of the sample. The impurities also contaminated the silicon probe, which resulted in less accurate scans. The images at higher resolution scans were systematically defected. With longer treatment times the oxide layer and the concentration of the impurities on the surface increased and AFM measurements would be even more problematic. Therefore, it was decided to not continue with this type of measurements and focus more on the ellipsometric measurements, described in section 2.6.

3.3.3 Oxidation and erosion of CdTe surface in NaCl solution

To better understand the effect of polluted ambient on the CdTe surface vitiation the saturated NaCl water solution was chosen. Na element is in suspect to diffuse fast in the CdTe lattice that could affect electrical properties of devices. It also strongly reacts with the acceptor-type defects. It is assumed that Na as the group I element diffuses fast interstitially similarly as Li [53], so it can also fast penetrate the material and bind to native defects undetected by chemical profile analyses. The structure of the surface and Na distribution can be sufficiently examined by the SIMS method, which is well sensitive to Na.

No exact diffusion data on Na for temperature less than 500K are found in the literature. The diffusion coefficient of Na D_{Na} was measured at T=500-700K [71] on semi-insulating p-CdTe:Cl

$$D_{Na} = 1.18 \times 10^{-6} e^{\frac{-0.25eV}{k_B T}} (cm^2 s^{-1}). \quad (3.25)$$

Similar activation energy, 0.3 eV, of resistivity relaxation in p-CdTe subjected to cyclic thermal changes were reported in [70].

Extrapolating eq. (10) to 50°C confirms our assumption of pretty fast Na diffusion with D_{Na}(50°C) = 1.5×10^{-10} cm^2s^{-1}. We show in Fig. 3.35 the SIMS measurement of normalized profiles of [Na] near the surface after the treatment of the samples in salt water. It can be seen that the damping of [Na] with the depth is much steeper than it would correspond to the D_{Na} above. The thickness of the affected layer defined by the drop of normalized density to 0.1 vs time is shown in Fig. 3.36.

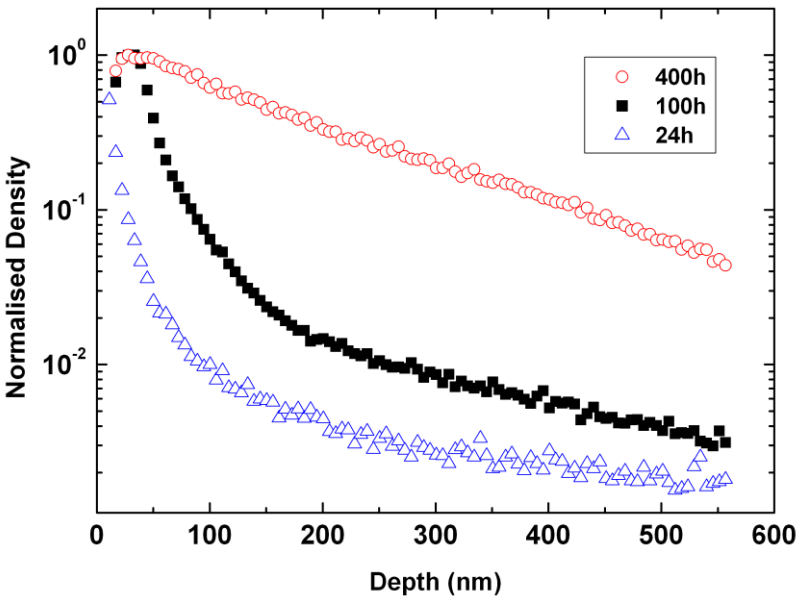

Fig. 3.35: Normalized density of Na distributed in the CdTe sample after 24h, 100h, and 400h treatment times.

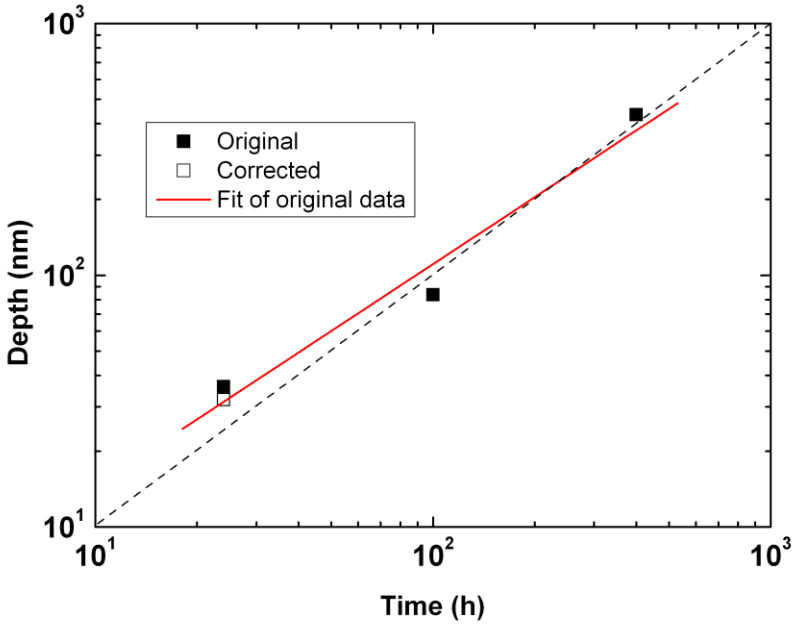

Fig. 3.36: Temporal dependence of penetration depth of Na into CdTe. Full squares were deduced directly from the data, open square was obtained by an extrapolation of the Na profile near the surface. Full (red) line is the fit. Dash line shows the slope 1 guide.

We may see that the slope of the Na penetration is close to 1. Such finding excludes the diffusion model of Na penetration that would have to be characterized by a ½ slope. We thus have to search for another model describing Na propagation. We deduce that determined profiles are connected with the trapping of Na on point defects created in the material. We assume the Na^+ drifts interstitially in the electric field induced by charge redistribution near the CdTe surface. It is significantly trapped in the lattice substituting Cd by the reaction

$$CdTe + Na_I \rightarrow Na_{Cd}Te + Cd_I\,. \tag{3.26}$$

Sodium may spend significant time as the Cd-substituting species before its repeated liberation. Since the re-liberation energy of Na_{Cd} could be pretty large, the migration of Na at room temperature may be much slower than one could estimate from the extrapolation of D_{Na} in eq. (10) to the low temperature. We may thus conclude that the long-term treatment of CdTe in the salt water may affect the bulk to the depth of hundreds nm. Unfortunately, SIMS does not allow us exact determination of the defect density.

If we estimate the band bending characterizing the electric potential near the surface by ~ 0.1 eV and the width of depletion layer deduced from the sample bulk resistivity 300 Ωcm to W=1μm, we may calculate the effective Na mobility in p-CdTe at 50°C as μ_{Na}~10^{-14}cm^{2}V^{-1}s^{-1}. The respective diffusion coefficient deduced via Einstein relation results D_{Na}~10^{-15}cm^{2}s^{-1}.

For Fig. 3.35 we need to note that for the 24h treatment the Na distribution near to the surface could not be measured with the same precision as for the longer times. This is due to the fact, that the oxide thickness for 24h is around 6 nm (see Fig. 3.27), which is comparable to the Na penetration depth. Simultaneously, the detected Na profile is influenced by the matrix effect caused by the oxidized surface layer. In order to estimate the maximum Na concentration, for the 24h measurement for the normalized distribution, we extrapolated the first three measured data, obtained at depth 12-22 nm, linearly to gain a theoretical maximum at the surface. From this theoretical maximum and the first value in the graph (representing the measured concentration maximum) we calculated a geometrical average, which was used to normalize the measured data with the aim to receive an analogical curve as we

gained for the longer treatment times. For the longer treatment times, the concentration was normalized without any correction.

3.3.4 Summary of oxidation and erosion of CdTe surface

The evolution of the surface structure of low resistivity p-type CdTe single crystals long-term treated in distilled water and NaCl solution at 50°C was investigated by ellipsometry, XPS and SIMS. It was revealed that the oxidation of CdTe surface proceeds significantly faster than it was observed in air and reached 7 nm after 100 h treatment. As the mechanism limiting the oxidation process, the drift of Cd ions through the oxide layer was suggested and theoretical models were elaborated. The treatment in NaCl solution showed significantly slower Na diffusion than it could be deduced from diffusion at higher temperatures. This effect was explained by trapping of Na in Cd sublattice.

3.4 Photoluminescence measurement of as-grown sample

For obtaining additional information about the defect structure of the p-CdTe samples we performed a supplementary low-temperature photoluminescence (PL) measurement. An as-grown sample was chosen from the same crystal area as the samples investigated in chapters 3.1, 3.2 and 3.3.

During the PL measurements at low temperature less than 10 K we observed several spectral lines in the vicinity of the bandgap (see Fig. 3.37**Fig. 3.37:** The photoluminescence spectra of an as-grown sample.) related to the recombinations of free exciton (FX and its phonon replicas FX-LO and FX-2LO) and excitons bound to the shallow levels. We identified recombination of exciton (D^0-X) bound to the shallow neutral donor localized 3 meV below the bandgap. Two types of shallow neutral acceptors at 6 meV (A_1^0-X) and 7 meV (A_2^0-X) above the valence band were also observed from which the more significant (A_2^0-X) is accompanied by three phonon replicas. Another PL line was observed 1.539 eV. According to Molva et. al. [78] its probable origin is the so called „two-hole-transition" (THT) related to the

recombination of the exciton bound to the shallow neutral acceptor (A_2^0-X) accompanied by the excitation of the hole at the acceptor to the state $3S_{3/2}$. Based on [78] and this coincidence we can clearly conclude that (A_2^0-X) is related to the presence of sodium atoms embedded in Cd sublattice forming substitution defect Na_{Cd}.

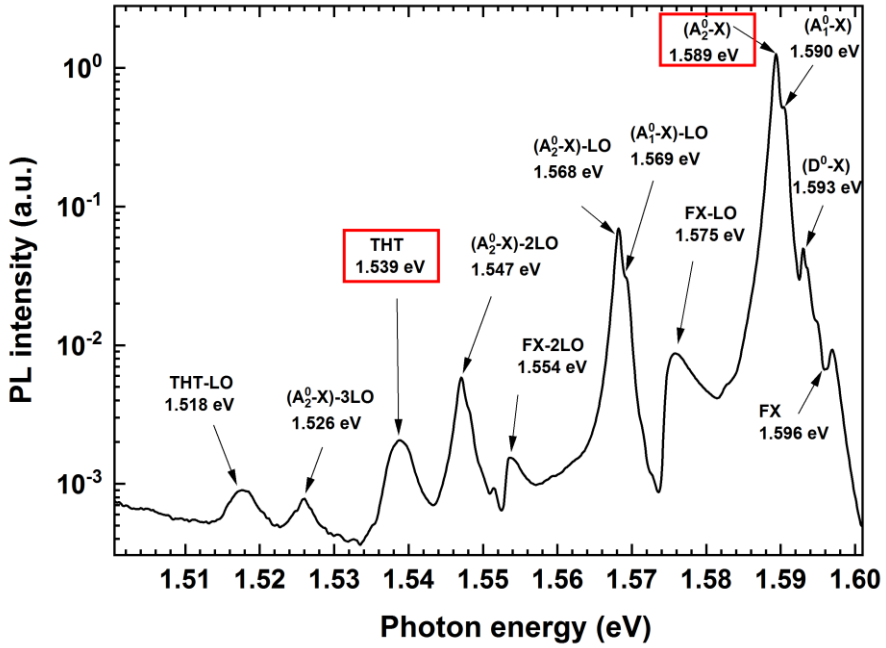

Fig. 3.37: The photoluminescence spectra of an as-grown sample.

The observation of Na in the PL spectrum of the as-grown sample is in good agreement with our conclusions in chapters 3.1.2 and 3.2.2. Sodium is a volatile element in the crystal lattice either substituting Cd in the Cd sublattice (Na_{Cd}) forming shallow acceptor or liberated in the interstitial site (Na_I) being a fast diffusing shallow donor.

4. Conclusion

In this thesis the thermal stability of p-type CdTe single crystals from as grown ingot was studied. In order to describe the observed characteristics of the crystal, conductivity, Hall-effect measurements XPS and SIMS measurements were combined. First, step-like temperature changes in the interval 30-100°C followed by a dwell were applied, in which the relaxation of resistivity and Hall coefficient were monitored. While Sample I exhibited increasing/decreasing resistivity after increasing/decreasing temperature step, an opposite behavior was identified at Sample II. Faster relaxation of Sample I allowed us to establish the activation energy of the process 0.3 eV. The relaxation effects were attributed to fast diffusing group I donors penetrating the material at densities ~ 10^{13}cm^{-3} in Sample I and ~ 10^{14} cm^{-3} in Sample II.

In the following part of the thesis conductivity and Hall-effect measurements in p-type CdTe single crystals were performed by continuous thermal changes in the range of 30-180°C. It was shown that thermal changes often lead to anomalous behavior of the hole density characterized by reversible decrease/increase at the heating/cooling regime. The anomaly was explained by the transfer of fast diffusing donors between Te inclusions and ambient bulk. Sodium and potassium were proposed as the most probable diffusing species by the SIMS. Theoretical model based on this premise was built up and successfully applied to experimental data.

Besides, the evolution of the surface structure of low resistivity p-type CdTe single crystals was studied. The crystals were long-term treated in distilled water and NaCl solution at 50°C and investigated by ellipsometry, XPS and SIMS. It was revealed that the oxidation of CdTe surface proceeds significantly faster than it was observed in air and reached 7 nm after 100 h treatment. As the mechanism limiting the oxidation process, the drift of Cd ions through the oxide layer was suggested and theoretical models were elaborated. The treatment in NaCl solution showed significantly slower Na diffusion than it could be deduced from diffusion at higher temperatures. This effect was explained by trapping of Na in Cd sublattice. The presence of Na was also affirmed by the analysis of the low temperature PL spectrum.

5. Bibliography

[1] M. Fabre , *Ann. Chim. Phys*, vol. 14, p. 110, 1888.

[2] R.Triboulet, P.Siffert, *CdTe and related compounds: physics, defects, hetero- and nano- structures, crystal growth, surfaces and applications – Part I.: physics, CdTe-based nanostructures, semimagnetic semiconductors, defects*.: Elsevier, 2010.

[3] M. L. Cohen, J.R. Chelikowsky, *Electronic Structure and Optical Properties of Semiconductors*. Berlin: Springer-Verlag, 1988.

[4] N. B. Vasyl'ovych, *The study of chemical diffusion and properties of electric contacts on CdTe for gamma ray detector applications*. Prague, 2010.

[5] S. Del Sordo, L. Abbene, E. Caroli, A.M. Mancini, A. Zapettini, P. Ubertini, "Progress in the development of CdTe and CdZnTe semiconductor radiation detectors for astrophysical and medical applications," *Sensors*, vol. 9, pp. 3491-3526, 2009.

[6] J. Sites, A Munshi, J. Kephart, D. E. Swanson, "Progress and challenges with CdTe cell efficiency," pp. 3622-3635, 2016.

[7] R. A. Chipman, S. Lu D. B. Chenault, "Electro-optic coefficient spectrum of cadmium telluride," *Appl. Opt.*, vol. 33, pp. 7382-7389, 1994.

[8] E. O. Kane , "Band structure of indium antimonide," *J. Phys. Chem. Solids*, vol. 1, no. 4, pp. 249-261, 1957.

[9] K. L. Shaklee, F. H. Pollak M. Cardona, "Electroreflectance at a Semiconductor-Electrolyte Interface," *Phys. Rev.*, vol. 154, no. 3, p. 696, 1967.

[10] D.J. Chadi, J.P. Walter, M. L. Cohen, Y.Petroff, M. Balkanski, "Reflectivities and Electronic Band Structures of CdTe and HgTe," *Physical Review B*, no. 5, pp. 3058-3064, 1972.

[11] A.L.Mears, R.A.Stradling, "Cyclotron resonance and cross-modulation with n-type CdTe at 1 mm and 2 mm wavelength," *Solid State Communications*, vol. 7, no. 17, pp. 1267-1269, 1969.

[12] D. Kranzer, "Hall and drift mobility of polar p-type semiconductors," *Journal of Physics C: Solid State Physics*, vol. 6, no. 20, pp. 2977-2987, 1973.

[13] S. Yamada, "On the Electrical and Optical Properties of p-type Cadmium Telluride Crystals," *Journal of the Physical Society of Japan*, vol. 15, pp. 1940-1944, 1960.

[14] R. Triboulet, Y. Marfaing, "Growth of High Purity CdTe Single Crystals by Vertical Zone Melting," *J. Electrochem. Soc.*, vol. 120, no. 3, pp. 1260-1265, 1973.

[15] D.A.Porter, K.E.Easterling, *Phase Transformations in Metals and Alloys*.: CRC Press, 1992.

[16] P.Kratochvil, P.Lukac, B.Sprusil, *Introduction to physics of metals I*.: SNTL - Alfa, 1984.

[17] P. W. Bridgman, "Crystals and their manufacture," patent US1793672A, Feb. 16, 1926.

[18] Cs. Szeles, S. E. Cameron, J. O. Ndap, W. C. Chalmers, "Advances in the crystal growth of semiinsulating CdZnTe for radiation detector applications," in *Nuclear Science Symposium Conference Record*, 2001, pp. 2535-2540.

[19] Y.Feutelais, B.Legendre A.Haloui, "Experimental study of the ternary system Cd Te Zn," *J. Alloys Compounds*, vol. 260, pp. 179-192, 1997.

[20] R. Grill, A. Zapettini, "Point defects and diffusion in cadmium telluride," *Prog. Cryst. Growth Charact. Mater.* , pp. 209-244, 2004.

[21] R. Grill, J. Franc, P. Hoschl, I. Turkevych, E. Belas, P. Moravec, M. Fiderle, K-W. Benz, "High-Temperature Defect Structure of Cd- and Te-Rich CdTe," *IEEE Transactions*, vol. 49, pp. 1270 - 1274, 2002.

[22] R.Fang, R.F.Brebrick, "CdTe I: Solidus curve and composition-temperature-tellurium partial pressure data for Te-rich CdTe(s) from optical density measurements," *J. Phys. Chem. Solids*, vol. 57, no. 4, pp. 443-450, 1996.

[23] V. N. Guskov, V. B. Lazarev, O. V. Shebershneva J. H. Greenberg, "Vapor-pressure scanning of nonstoichiometry in cadmium telluride," *Mater. Res. Bull.* , vol. 27, pp. 847–854, 1992.

[24] R.F. Brebrick, "Equilibrium constants for quasi-chemical defect reactions," *J.Electron. Mater.* , vol. 33, no. 11, pp. L24–L26, 2004.

[25] M. Bugár, *Dynamics of structural defects in CdTe-based semiconductors*. Prague, 2011.

[26] M. van Schilfgaarde, A. Sher M.A. Berding, "First-principles calculation of native defect densities in HgCdTe," *Phys. Rev. B*, vol. 50, p. 1519, 1993.

[27] D. Nobel, "Phase equilibria and semiconducting properties of cadmium telluride," *Philips Res. Rep.*, vol. 14, pp. 361-399, 1959.

[28] S.S. Chern, H.R. Vydyanath, F.A. Kröger, "The defect structure of CdTe: Hall Data," *J. Solid State Chem.* , vol. 14, pp. 33-43, 1975.

[29] S.-H. Wei, S.B. Zhang, "Chemical trends of defect formation and doping limit in II-VI semiconductors: The case of CdTe," *Phys. Rev. B*, vol. 66, no. 15, p. 155211, 2002.

[30] S.H.Wei, S.B.Zhang, "First-principles study of doping limits of CdTe," *Phys. Stat. Sol. (b)*, vol. 229, pp. 305-310, 2002.

[31] J. Philibert, *Atom movements diffusion and mass transport in solids*.: EDP Sciences, 1991.

[32] P. Moravec, R. Grill, J. Franc, R. Varghová, P. Höschl, E. Belas, "Galvanomagnetic and thermoelectric properties of p-Hg1-xCdxTe (x approx. 0.22) ," *Semicond. Sci. Technol.*, vol. 16, pp. 7-13, 2001.

[33] G. Korcsmáros, P. Moravec, R. Grill, "Stability of galvanomagnetic properties of CdTe in the range 30 – 100 °C," *Electroscope*, vol. 5, 2013.

[34] B. M. Askerov, *Electron transport phenomena in semiconductors*. Singapore: World Scientific Publisher Company, 1994.

[35] H. Fujiwara, *Spectroscopic ellipsometry: principles and applications*. Chichester: John Wiley & Sons, 2007.

[36] V.D. Popovych, F.F. Sizov, O.A. Parfenjuk, Z.F.T. Ivasiv, "The effect of inhomogeneous dopant distribution on the electrical transport properties and thermal stability of CdTe:Cl single crystals," *Semicond. Sci. Technol*, vol. 25, no. 3, 2010.

[37] A.V. Savitsky, O.A. Parfenyuk, M.I. Ilashchuk, P.M. Fochouk, N.D. Korbutyak, "Relaxation processes in CdTe Cl crystals," *Semicond. Sci. Technol.*, vol. 15, no. 263, 2000.

[38] R. Grill, J. Franc, P. Hoschl, I. Turkevych, E. Belas, P. Moravec, "Semi-insulating Te-saturated CdTe," *IEEE Trans. Nucl. Sci.*, vol. 52, no. 5, pp. 1925 - 1931, 2005.

[39] R. Grill, L. Turjanska, J. Franc, E. Belas, I. Turkevych, P. Hoschl , "Chemical Self-Diffusion in CdTe," *Phys. Stat. sol. B*, vol. 229, pp. 161-164, 2002.

[40] E.D. Jones, J.C. Clark, , EMIS Datareviews Series No. 10 P. Capper (Ed.), Ed.: INSPEC, IEE, London, 1994, p. 472.

[41] O. Kopach, P. Fochuk, A.E. Bolotnikov, R.B. James L. Shcherbak, "Empirical Correlations Between the Arrhenius' Parameters of Impurities' Diffusion Coefficients in CdTe Crystals," *J. Phase Equilib. Diff.*, vol. 36, no. 2, pp. 99-109, 2015.

[42] J.P. Chamonal, E. Molva, J.L. Pautrat, L. Revoil, "Complex behaviour of Ag in CdTe," *J. Cryst. Growth*, vol. 59, pp. 297-300, 1982.

[43] E. Belas, R. Grill, M. Bugar, J. Prochazka, P. Hlídek, P. Praus, J. Franc, P. Hoschl, "Electromigration of Mobile Defects in CdTe," *IEEE Trans. Nucl. Sci.*, vol. 56, pp. 1752-1757, 2009.

[44] H. Wolf, J. Kronenberg, F. Wagner, M. Deicher, T. Wichert, "Shift of Ag diffusion profiles in CdTe by metal/semiconductor interfaces," *Appl. Phys. Lett.* , vol. 100, no. 17, p. 171915, 2012.

[45] H. Wolf, F. Wagner, T. Wichert, "Anomalous Diffusion Profiles of Ag in CdTe due to Chemical Self-Diffusion," *Phys. Rev. Lett.* , vol. 94, p. 125901 , 2005.

[46] K. Zanio, "Chemical Diffusion in Cadmium," *J. Appl. Phys*, vol. 41, p. 1935, 1970.

[47] I. Lyubomirsky, M.K. Rabinal, D. Cahen, "Room-temperature detection of mobile impurities in compound semiconductors by transient ion drift," *J. Appl. Phys.*, vol. 81, p. 6684, 1997.

[48] E.D. Jones, J.C. Clark, "Diffusion of group I, II and III impurities in CdTe," *EMIS Datareviews Series No.10 (P. Capper Ed., INSPEC, IEE)*, p. 472, 1994.

[49] D. Kranzer, "Mobility of holes of zinc-blende III–V and II–VI compounds," *Phys. Stat. Sol. (a)*, vol. 26, no. 11, 1974.

[50] A. Zappettini, L. Marchini, M. Zha, G. Benassi, N. Zambelli, D. Calestani, L. Zanotti, E. Gombia, R. Mosca, M. Zanichelli, M. Pavesi, N. Auricchio, E. Caroli, "Growth and Characterization of CZT Crystals by the Vertical Bridgman Method for X-Ray Detector Applications," *IEEE Trans. Nucl. Sci.*, vol. 58, no. 5, 2011.

[51] G. Yang, A.E. Bolotnikov, Y. Cui, G.S. Camarda, A. Hossain, R. James, "Impurity gettering effect of Te inclusions in CdZnTe single crystals," *J. Cryst. Growth*, vol. 311, no. 1, pp. 99-102, 2008.

[52] P. Fochuk, I. Nakonechnyi, O. Panchuk, O. Kopach, Y. Nykonyuk, R. Grill, E. Belas, K.H. Kim, A.E. Bolotnikov, G. Yang, R.B. James, "Changes in the Electrical Parameters of CdTe-based Crystals During Isothermal Annealing," *IEEE Trans. Nucl. Sci.*, vol. 62, no. 3, pp. 1239 - 1243, 2015.

[53] L. Svob, C. Grattepain, "Low-temperature diffusion of lithium in CdTe," *J. Solid State Chem.*, vol. 20, no. 3, pp. 297-303, 1977.

[54] E. Belas, P. Moravec, R. Grill, J. Franc, A.L. Toth, H. Sitter, P. Hoschl, "Silver diffusion in p-type CdTe and (CdZn)Te near room temperature," *Phys. Stat. Sol. C.*, vol. 1, no. 4, pp. 929-932, 2004.

[55] W.H. Press, S.A. Teukolsky, W.T. Vetterling, B.P. Flannery, *Numerical Recipes in Fortran*, 2nd ed. New York: Cambridge University Press, 1992.

[56] A.J. Nelson, A.M. Conway, C.E. Reinhardt, J.L. Ferreira, R.J. Nikolic, S.A. Payne, "X-ray photoemission analysis of passivated Cd(1 − x)ZnxTe surfaces for improved radiation detectors," *Mater. Lett.*, vol. 63, pp. 180-181, 2009.

[57] S. Mergui, M. Hage-Ali, J. M. Koebel, P. Siffert, "Thermal annealing of gold deposited contacts on high resistivity p-type CdTe nuclear detectors," *Nucl. Instrum. Methods Phys. Res. A.*, vol. 322, pp. 375–380, 1992.

[58] K. Meinander, J. L. Carvalho, C. Miki, J. Rideout, S. M. Jovanovic, G. A. Devenyi, J. S. Preston, "Purified water etching of native oxides on heteroepitaxial CdTe thin films," *J. Phys. D: Appl. Phys.*, vol. 47, p. 495304, 2014.

[59] J. Crocco, H. Bensalah, Q. Zheng, F. Dierre, P. Hidalgo, J. Carrascal, O. Vela, J. Piqueras, E. Dieguez, "Study of the effects of edge morphology on detector performance by leakage current and cathodoluminescence," *IEEE Trans. Nucl. Sci.*, vol. 1935-1941, no. 4, 2011.

[60] H.W. Yao, J.C. Erickson, H.B. Barber, R.B. James, H. Hermon, "Optical properties of Cd0.9Zn0.1Te studied by variable angle spectroscopic ellipsometry between 0.75 and 6.24 eV," *J. Electron. Mater.* , vol. 28, pp. 760–765, 1999.

[61] J. Zázvorka, J. Franc, L. Beran, P. Moravec, J. Pekárek, M. Veis, "Dynamics of native oxide growth on CdTe and CdZnTe X-ray and gamma-ray detectors," *Sci. Technol. Adv. Mater.*, vol. 17, pp. 792-798, 2016.

[62] G. Badano, A. Million, B. Canava, P. Tran-Van, A. Etcheberry, "Fast detection of precipitates and oxides on CdZnTe surfaces by spectroscopic ellipsometry," *J. Electron. Mater.*, vol. 36, no. 8, pp. 1077-1084, 2007.

[63] M. E. Özsan, P. J. Sellin, P. Veeramani, S. J. Hinder, M. L. T. Monnier, G. Prekas, A. Lohstroh, M. A. Baker, "Chemical etching and surface oxidation studies of cadmium zinc telluride radiation detectors," *Surf. Interface Anal.*, vol. 42, pp. 795–798, 2010.

[64] A. S. Grove B. E. Deal, "General Relationship for the Thermal Oxidation of Silicon," *J. Appl. Phys.*, vol. 36, pp. 3770-3778, 1965.

[65] H. Li, J. Robertson, "Germanium oxidation occurs by diffusion of oxygen network interstitials," *Appl. Phys. Lett.*, vol. 110, no. 22, p. 222902, 2017.

[66] A. Atkinson, "Transport processes during the growth of oxide films at elevated temperature," *Rev. Mod. Phys.*, vol. 57, pp. 437-470, 1985.

[67] K.D. Choquette, K.M. Geib, C.I.H. Ashby, R.D. Twesten, O. Blum, H.Q. Hou, D.M. Follstaedt, B.E. Hammons, D. Mathes, R. Hull, "Advances in selective wet oxidation of AlGaAs alloys," *IEEE J. Sel. Top. Quantum Electron.*, vol. 3, pp. 916–926, 1997.

[68] N. Cabrera, N. F. Mott, "Theory of the oxidation of metals," *Rep. Prog. Phys.*, vol. 12, pp. 163-184, 1949.

[69] Ch. Gattinoni, A. Michaelides, "Atomistic details of oxide surfaces and surface oxidation: the example of copper and its oxides," *Surf. Sci. Rep.*, vol. 70, pp. 424-447, 2015.

[70] G.Korcsmaros, P. Moravec, R. Grill, A. Musiienko, K. Mašek, "Thermal stability of bulk p-CdTe," *J. Alloy. Compd.* , vol. 680, pp. 8-13, 2016.

[71] Y.M. Ivanov, G.S. Pavlova, E.L. Kanunova, "The Diffusion of Indium and Sodium in Chlorine-Doped CdTe," *Inorg. Mater.* , vol. 24, pp. 1681-1684, 1988.

[72] S. S. Choi, G. Lucovsky, "Native oxide formation on CdTe," *J. Vac. Sci. Technol. B.*, vol. 6, pp. 1198-1203, 1988.

[73] H. W. Yao, J. C. Erickson, H. B. Barber, R. B. James, H. Hermon, "Optical properties of Cd0.9Zn0.1 Te studied by variable angle spectroscopic ellipsometry between 0.75 and 6.24 eV," *J. Electron. Mater.*, vol. 28, pp. 760-765, 1999.

[74] M. K. Bahl, R. L. Watson, K. J. Irgolic, "X-ray photoemission studies of tellurium and some of its compounds," *J. Chem. Phys.*, vol. 66, pp. 5526-5535, 1977.

[75] T.L. Chu, Shirley S. Chu, S.T. Ang, "Surface passivation and oxidation of cadmium telluride and properties of metal-oxide-CdTe structures," *J. Appl. Phys.*, vol. 58, no. 8, p. 3206, 1985.

[76] P. Moravec, V.G. Ivanits'ka, J. Franc, Z.F. Tomashik, V. Tomashyk, K. Masek, P.I. Feychuk, L.P. Shcherbak, P. Hoschl, R. Grill, J. Walter, "Chemical Interaction of CdTe and CdZnTe with Aqueous Solutions of H2O2-HI-Tartaric Acid," *J. Electron. Mater.*, vol. 38, 1645-1651 2009.

[77] V.G. Ivanitska, P. Moravec, J. Franc, Z.F. Tomashik, P.I. Feychuk, V.M. Tomashik, L.P. Shcherbak, K. Masek, P. Hoschl, "Chemical etching of CdTe in aqueous solutions of H2O2-HI-citric acid," *J. Electron. Mater.*, vol. 36, no. 8, pp. 1021–1024, 2007.

[78] E. Molva, J. L. Pautrat, K. Saminadayar, G. Milchberg, N. Magnea, "Acceptor states in CdTe and comparsion with ZnTe. General trends," *Phys. Rev. B*, vol. 30, pp. 3344-3354, 1984.

[79] R. Fang and R. F. Brebrick, "CdTe I: Solidus curve and composition-temperature-tellurium partial pressure data for Te-rich CdTe(s) from optical density measurements," *J. Phys. Chem. Solids*, vol. 57, pp. 443–450, 1996.

List of tables

List of Abbreviations

A^0-*X*	recombination of exciton bound to the shallow neutral acceptor
AFM	atomic force microscope
BM	Bridgman method
CMP	congruent melting point
D^0-*X*	recombination of exciton bound to the shallow neutral donor
DS	diffusing species
erf	error function on error integral of Gauss
erfc	complementary error function defined as 1-erf
FX	free exciton
FX-LO	free exciton phonon replica
GDMS	glow discharged mass spectroscopy
hh	heavy-hole
lh	light-hole
MSE	mean squared error
PL	photoluminescence
SIMS	secondary ion mass spectroscopy
SPP	second-phase particles
THM	travelling heater method
THT	two hole transition
UHV	ultrahigh vacuum chamber
VGF	vertical-gradient freezing
XPS	x-ray photoelectron spectroscopy

List of Symbols

A_I	interstitial defect
B	magnetic field
c	concentration
c_s	surface concentration
D	diffusion coefficient
E_a , E_d	acceptor and donor one-electron ionization energies
E_b	binding energy
E_D	activation energy
E_F	Fermi energy
E_G	energy of the bandgap
E_{hh}	energy of the heavy holes
E_{lh}	energy of the light holes
E_{so}	energy of the spin-orbit
E_n	energy of the electrons
eV	electronvolt
F	Helmholtz free energy
G	Gibbs energy
$g_{X^{z-}}$	defect degeneracies, z refers to the ionization energy
H	Enthalpy
$\hbar$	Plank's constant
i	current density
J	flux
k	wave vector
k_b	Boltzmann constant
$K_{V_A^0}$	reaction rate constant
$L(k_i c_i)$	scattering operator
m_0	free electron rest mass
m_n	electron effective mass at bottom of conduction band
m_{lh}	light hole effective mass
m_{hh}	heavy hole effective mass
m_{so}	spin-orbit split off band effective mass

m_{Cd}	mass of the Cd atom
n	concentration of electrons
n_l *and* n_s	material amounts in the liquid and solid phase
Na_{Cd}	Na in the Cd sublattice
N_{a1}	density of states
p	concentration of holes
P_{Cd}	partial pressure of Cd
$\vec{p}$	momentum operator
Q	quantity of deposited atoms
r_H	Hall factor
R_H	Hall coefficient
S	entropy
Te_{Cd}	donor type Te antisite
U	internal energy
$\langle v \rangle$	average velocity
V_A	vacancy defect
$W(k,k')$	scattering probability
Z	atomic number
Γ	center of Brillouin zone
Δ_0	spin-orbit splitting energy
Φ	degrees of freedom
Ψ and Δ	ellipsometric angles
μ_{Cd}	chemical potential of Cd
μ_n	electron mobility
μ_p, μ_h	hole mobility
σ_{ij}	conductivity tensor
ρ	resistivity